WAPD-TM--1387

DE88 005498

WAPD-TM-1387
Distribution Category UC-78

LIGHT WATER BREEDER REACTOR FUEL ROD DESIGN AND PERFORMANCE CHARACTERISTICS

(LWBR Development Program)

W. R. Campbell
J. F. Giovengo

Contributors: J. C. Clayton
D. A. Gorscak

Contract No. DE-AC11-76PN00014

October 1987

Printed in the United States of America
Available from the
National Technical Information Service
U. S. Department of Commerce
5285 Port Royal Road
Springfield, Virginia 22161

NOTE

This document is an interim memorandum prepared primarily for internal reference and does not represent a final expression of the opinion of Westinghouse. When this memorandum is distributed externally, it is with the express understanding that Westinghouse makes no representation as to completeness, accuracy, or usability of information contained therein.

Bettis Atomic Power Laboratory West Mifflin, Pennsylvania 15122-0079
Operated for the U. S. Department of Energy by
WESTINGHOUSE ELECTRIC CORPORATION

FOREWORD

The Shippingport Atomic Power Station located in Shippingport, Pennsylvania was the first large-scale, central-station nuclear power plant in the United States and the first plant of such size in the world operated solely to produce electric power. This program was started in 1953 to confirm the practical application of nuclear power for large-scale electric power generation. It has provided much of the technology being used for design and operation of the commercial, central-station nuclear power plants now in use.

Subsequent to development and successful operation of the Pressurized Water Reactor in the Atomic Energy Commission (now Department of Energy, DOE) owned reactor plant at the Shippingport Atomic Power Station, the Atomic Energy Commission in 1965 undertook a research and development program to design and build a Light Water Breeder Reactor core for operation in the Shippingport Station.

The objective of the Light Water Breeder Reactor (LWBR) program has been to develop a technology that would significantly improve the utilization of the nation's nuclear fuel resources employing the well-established water reactor technology. To achieve this objective, work has been directed toward analysis, design, component tests, and fabrication of a water-cooled, thorium oxide-uranium oxide fuel cycle breeder reactor for installation and operation at the Shippingport Station. The LWBR core started operation in the Shippingport Station in the Fall of 1977 and finished routine power operation on October 1, 1982. After end-of-life core testing, the core was removed and the spent fuel shipped to the Naval Reactors Expended Core Facility for detailed examination to verify core performance including an evaluation of breeding characteristics.

In 1976, with fabrication of the Shippingport LWBR core nearing completion, the Energy Research and Development Administration, now DOE, established the Advanced Water Breeder Applications (AWBA) program to develop and disseminate technical information which would assist U.S. industry in evaluating the LWBR concept for commercial-scale applications. The AWBA program, which was concluded in September, 1982, explored some of the problems that would be faced by industry in adopting technology confirmed in the LWBR program. Information developed includes concepts for commercial-scale prebreeder cores which would produce uranium-233 for light water breeder cores while producing electric power, improvements for breeder cores based on the technology developed to fabricate and operate the Shippingport LWBR core, and other information and technology to aid in evaluating commercial-scale application of the LWBR concept.

All three development programs (Pressurized Water Reactor, Light Water Breeder Reactor, and Advanced Water Breeder Applications) have been conducted under the technical direction of the Office of the Deputy Assistant Secretary for Naval Reactors of DOE.

Technical information developed under the Shippingport, LWBR and AWBA programs has been and will continue to be published in technical memoranda, one of which is this present report.

TABLE OF CONTENTS

Section	Title	Page
List of Figures		viii
List of Tables		ix
List of Abbreviations and Acronymns		xi
1	INTRODUCTION AND BACKGROUND	1
1.1	LWBR Objectives	1
1.2	Unique Features of the LWBR Core	2
1.2.1	Physics	2
1.2.2	Thermal and Hydraulics	4
1.2.3	Core Mechanical Description	6
1.2.4	Fuel Element Design	9
2	OPERATIONAL REQUIREMENTS AND ENVIRONMENTAL CONDITIONS	11
2.1	Duty Requirements	11
2.2	Operational Requirements	11
2.3	Environmental Conditions	14
2.4	Transients and Accidents	15
3	MECHANICAL DESIGN OF THE FUEL RODS	19
3.1	General Description	19
4	UNIQUE FEATURES OF THE FUEL ROD DESIGN	27
4.1	Uranium-233 Fuel	27
4.2	Urania-Thoria Fuel System	28
4.3	Tight Lattice (High Metal-to-Water Ratio)	31
4.4	Low-Hafnium Zircaloy Tubing	33
4.5	Nonfreestanding Blanket Tubing	33
4.6	Recrystallization Annealed Seed Tubing	35
4.7	Tapered Fuel Pellets	36
4.8	Fuel Zoning for Control of Reactivity and Power Peaking	37

TABLE OF CONTENTS (Cont)

Section	Title	Page
4.9	Moving and Scramming Fuel	39
4.10	Bolted Top- and Bottom-Mounted Fuel Rods	40
4.11	Neolube in the System	42
5	SPECIFIC FUEL ELEMENT DESIGN CONSIDERATIONS	45
5.1	Fuel Pellet Temperature	45
5.2	Axial Gaps	47
5.2.1	Design Concern	47
5.2.2	Mechanism for Forming Axial Gap	47
5.2.3	Analytical Model	48
5.3	Rod Length Increase	48
5.3.1	Design Criteria	48
5.3.2	Analytical Model	49
5.3.3	Qualification of CYGRO Model	49
5.3.4	Design Calculations	50
5.4	Stress Corrosion Cracking	50
5.5	Overpower Transients	56
5.6	Cladding Corrosion and Hydriding	58
5.6.1	Design Concern	58
5.6.2	Analysis	58
5.6.3	Corrosion Model	59
5.6.4	The CHORT Program Calculations	59
5.6.5	Discussion of Results	61
5.7	Rod Bow	65
5.7.1	Design Concern	65
5.7.2	Analysis	65
5.8	Fission Gas Release and Loss-of-Coolant Accident Performance	68
5.8.1	Design Concern	68
5.8.2	Discussion	68
5.8.3	Impact of Fission Gas Internal Pressure on Loss-of-Coolant Accident	74

TABLE OF CONTENTS (Cont)

Section	Title	Page
5.9	Cladding Fatigue	76
5.10	Endclosure Welds	77
5.11	Defect Operation	81
5.11.1	Design Concern	81
5.11.2	Design Basis	81
5.11.3	Analysis	81
5.11.4	Corrosion Model for Defected Rods	82
5.11.5	The CHORT Program Calculations	82
5.11.6	Discussion of Results	83
5.11.7	Fuel Rod Failure	86
5.11.8	Summary	90
5.12	Cladding Wear	91
5.13	Pellet Integrity	98
5.14	Cladding Deformation	103
5.14.1	Design Concern	103
5.14.2	Analytical Models	104
5.14.2.1	Diametral Changes	104
5.14.2.2	Cladding Ovality (Cladding Collapse)	105
5.14.2.3	Grid-Induced Cladding Deformation (Dimpling)	112
5.14.2.4	Ridging	116
5.14.2.5	Grooving	118
5.15	Plenum Design	120
5.15.1	Plenum Volume	120
5.15.2	Support Sleeve	120
5.15.3	Plenum Spring	122
6	FABRICATION PROBLEMS AND LESSONS LEARNED	127
6.1	Fabrication Problems Affecting Fuel Rod Design	127
6.1.1	Pellet Chamfers	127
6.1.2	Pellet Lengths	127

TABLE OF CONTENTS (Cont)

Section	Title	Page
6.1.3	Plenum Support Sleeve Relief Holes	127
6.2	Fabrication Problems Affecting Technical Requirements	127
6.2.1	Tubing Internal Diameter Surface Borescope	128
6.2.2	Pellet Edge Cracks	129
6.2.3	Pellet Structure	129
6.2.4	In-Motion Radiography	130
6.2.5	Low-Density Reflector Fuel Pellets	131
6.2.6	Coring in Reflector Pellets	131
6.2.7	Fuel Rod Straightness	132
6.3	Lessons Learned	133
7	SUMMARY AND CONCLUSIONS	135
8	ACKNOWLEDGMENTS	137
9	REFERENCES	139
APPENDIX A1	DERIVATIONS OF EQUATIONS FOR CLADDING WEAR DEPTH	A1-1
A1.1	Vibrational Wear at a Stationary Wear Spot	A1-1
A1.2	Vibrational Wear at a Moving Wear Spot	A1-3
A1.3	Overlay Wear	A1-8
A1.4	Finite Dimple Width Effect	A1-16
APPENDIX A2	CLADDING STRAINS DUE TO RIDGING	A2-1

LIST OF FIGURES

Figure	Title	Page
1	Thorium-232 to Uranium Breeding Process	3
2	LWBR Core in Shippingport Reactor Vessel	5
3	Bypass Inlet Flow Balance System	7
4	Cross Section Module Identification	8
5	Power Duty Requirements	12
6	General Dimensions and Components of Seed Fuel Rods	22
7	General Dimensions and Components of Blanket Fuel Rods	23
8	General Dimensions and Components of Reflector Fuel Rods	24
9	Cross Sections of Typical LWBR Fuel Pellets	25
10	Lifetime Equivalency Parameter Versus Lifetime	55
11	Best Estimate Fission Gas Release	71
12	Design Fission Gas Release Over Lifetime	72
13	Tapered Insert and Friction Grip Endclosures	79
14	Hydride Failure Limit for Defected Zircaloy-Clad Fuel Rods	89
15	Standard Blanket Fuel Rod Plenum Ovalities	108
16	Seed Fuel Rod Plenum Ovalities	109
17	Standard Blanket Fuel Rod In-Stack Axial Gap Ovalities	110
18	Standard and Power Flattening Blanket Collapse Limits	112
19	Curves for Grid-Induced Cladding Dimpling Based on Irradiation Test Data	115

APPENDIX A1

A1-1	Development of Overlay Wear Due to Plant Shutdown and Power Reduction (LWBR Blanket Fuel Rods)	A1-11
A1-2	Overlay Wear at a Grid Spring	A1-12
A1-3	Overlay Wear at a Grid Dimple	A1-13
A1-4	Effect of Finite Dimple Width (Using LWBR Spring and Dimple Geometries)	A1-17

LIST OF TABLES

Table	Title	Page
1	Peak Local Linear Power Rating, Burnup, and Fluence for Each of the LWBR Fuel Regions	13
2	Operational Requirements of LWBR Fuel Elements	14
3	Environmental Conditions for Operations to 18,000 EFPH	15
4	Fuel Element Dimension Specifications	20
5	Materials of Construction	21
6	Unirradiated Fuels Best Estimate Melting Point	29
7	Unirradiated Fuels Best Estimate Thermal Conductivity	30
8	Unirradiated Fuels Best Estimate Thermal Expansion Coefficients	29
9	Typical Cladding Hoop Stress in Pressurized System	34
10	Peaking Factors - LWBR Versus Commercial	38
11	Scram and Contact Velocity	40
12	Maximum Fuel Temperatures and Design Limits	45
13	Calculated Elongations of LWBR Fuel Elements (at 18,000 EFPH)	50
14	CHORT Qualification Data Base	60
15	Input Data for CHORT Analysis of Nondefected LWBR Core Rods	62
16	CHORT-Calculated Corrosion Oxide Thickness for Nondefected LWBR Core Rods at Peak Power Position	63
17	CHORT-Calculated Hydrogen Pickup in Nondefected LWBR Core Rods at Peak Power Position	64
18	Initial Fuel Rod Bows	66
19	Initial Bow Due to Endconnector Tightening	67
20	Bow Components by Rod Type (18,000 EFPH)	69
21	Fuel Rod Spacing Limits	70
22	LWBR Fuel Rod Internal Gas Composition	73
23	Calculated Internal Fuel Rod Gas Pressure	74
24	Summary of Results of Assessment of Seismic and LOCA Events	75

LIST OF TABLES (Cont)

Table	Title	Page
25	Endclosure Weld Fatigue to 18,000 EFPH	80
26	CHORT Input Parameters for Defected LWBR Core Rod Calculations to 25,000 EFPH	83
27	CHORT-Calculated Internal Corrosion Oxide Thickness for Initially-Defected LWBR Core Rods at Peak Power Position	84
28	CHORT-Calculated Corrosion at 30,000 EFPH for Defected LWBR Core Rods at Peak Power Positions	85
29	Comparison of Core History and Failure Limit for Defected LWBR Seed Rods	88
30	LWBR Seed Fuel Rod Vibrational Wear Rates (for Operation at Full Coolant Flow Rate)	93
31	LWBR Blanket Fuel Rod Vibrational Wear Rates (for Operation at Full Coolant Flow Rate)	94
32	Summary of Cladding Wear Spot Depth Calculation	95
33	LWBR Blanket Rod Wear Depths (Predicted for 29,100 EFPH with Full Coolant Flow Rate)	99
34	LWBR Seed Rod Wear Depths (Predicted for 29,100 EFPH with Full Coolant Flow Rate)	99
35	Fuel Rod Diameter Shrinkage	105
36	Predicted Number of Fuel Rods with Collapsed Cladding	113
37	ACCEPT Predictions for Seed Grid-Induced Cladding Deformations at 30,000 EFPH	114
38	LWBR Fuel Rod Ridging	117
39	LWBR Blanket Fuel Rod Groove Depths	119
40	Plenum Void and Sleeve Dimensions (As-Installed at Room Temperature)	121
41	LWBR Fuel Rod Plenum Spring Specifications	123
42	Typical Characteristics of As-Built Springs	124
43	Calculated Lifetime Spring Load Ranges	126
44	Calculated Plenum Spring Conditions Over Lifetime	126

LIST OF ABBREVIATIONS AND ACRONYMNS

ACCEPT*	Analysis of Creep Collapse of Externally Pressurized Tubes
ATWS	Anticipated Transient without Scram
AWBA	Advanced Water Breeder Activity
BIF	Bypass Inlet Flow
BOL	Beginning of Life
CANDU	Canadian Deuterium-Uranium Fuel System
CHF	Critical Heat Flux
CHORT*	Corrosion and Hydriding of Reactor Tubing
CW	Cold Worked
CYGRO*	Cylindrical Growth, a fuel rod analysis program (CYGRO-4)
DECAG	Deformation of Cladding into Axial Gaps
DLEP	Delimiting Lifetime Equivalency Parameter
EFPD	Effective Full Power Days
EFPH	Effective Full Power Hours
EOL	End of Life
EPRI	Electric Power Research Institute
f/cc	Fissions per Cubic Centimeter, a measure of fuel depletion
FIGRO*	Fuel Internal Growth, a fuel rod temperature and dimension analysis program
FIR	Fissile Inventory Ratio, a measure of breeding
LEP	Lifetime Equivalency Parameter
LOCA	Loss-of-Coolant Accident
LWBR	Light Water Breeder Reactor
MELBA	Multipurpose Extended Life Blanket Assembly
METER*	Monte Carlo Employed to Evaluate Responses, a computer program simulating interactions between independent random variables
MFA	Movable Fuel Assembly
MWD/MTM	Megawatt Days per Metric Ton of Metal (U + T_h in LWBR fuel), a measure of fuel burnup
n/cm^2	Neutrons per Square Centimeter, a measure of fast neutron (>1 Mev) fluence
PCI	Pellet-Cladding Interaction
PCT	Peak Center Line Temperature
PWR	Pressurized Water Reactor
RIT	Reactivity Insertion Transient
ROBOT*	Computer Program for Calculating Rod Bow
RXA	Recrystallization Annealed
SCC	Stress Corrosion Cracking
SRA	Stress Relief Annealed

*Computer Program.

Light Water Breeder Reactor (LWBR) fuel rods were designed to provide a reliable fuel system utilizing thorium/uranium-233 mixed-oxide fuel while simultaneously minimizing structural material to enhance fuel breeding. The fuel system was designed to be capable of operating successfully under both load follow and base load conditions. The breeding objective required thin-walled, low hafnium content Zircaloy cladding, tightly spaced fuel rods with a minimum number of support grid levels, and movable fuel rod bundles to supplant control rods. Specific fuel rod design considerations and their effects on performance capability are described. Successful completion of power operations to over 160 percent of design lifetime including over 200 daily load follow cycles has proven the performance capability of the fuel system.

LIGHT WATER BREEDER REACTOR
FUEL ROD DESIGN AND PERFORMANCE CHARACTERISTICS

(LWBR Development Program)

SECTION 1 - INTRODUCTION AND BACKGROUND

This report describes the unique demands and features of the Shippingport light water breeder reactor (LWBR) as they affect the fuel system. Fuel rod design concerns are discussed, analysis methods used to predict fuel rod performance are presented, and fabrication problems and lessons learned are summarized.

1.1 - LWBR OBJECTIVES

The objective of the Light Water Breeder Reactor Program was the development of technology to significantly enhance the utilization of the nation's nuclear fuel resources in light water reactors. To achieve this objective, development work was directed toward analysis, design, component tests, and fabrication of a small, water-cooled thorium cycle breeder reactor.

The following were the specific objectives of LWBR:

1. Proof of breeding, which is the engineering demonstration that a light water reactor core can be designed and operated to generate more fissile fuel than was consumed during power operations.
2. Confirmation of the technology that would permit a vast additional energy resource (thorium) to be made available.
3. Confirmation of a basic technology that can be applied in large-scale commercial light water breeder reactors.
4. Confirmation of the more generally applicable theoretical and experimental work related to the utilization of ^{233}U and thorium in reactors.
5. Development of a light water reactor supplement to the uranium fuel cycle, with much more efficient use of fuel resources and with smaller overall adverse environmental impacts.

To accomplish these objectives, several unique features of the reactor were required as discussed below.

1.2 - UNIQUE FEATURES OF THE LWBR CORE

1.2.1 - Physics

Because of the primary objective of breeding, the nuclear requirements set the basic design of the light water breeder reactor. The mechanical, thermal and hydraulic, and fuel element designs were constrained by the nuclear requirements.

As discussed in Reference 1, the nuclear design of the LWBR core was directed toward the primary goal of breeding nuclear fuel by utilizing the thorium/uranium-233 fuel cycle in a pressurized light water environment. Figure 1 presents a schematic of the breeding process showing ^{232}Th conversion to uranium.

A neutron absorption in ^{232}Th produces ^{233}Th, which decays to ^{233}Pa. Protactinium-233 can β-decay with a 27-day half-life to produce ^{233}U or it can absorb a neutron to produce ^{234}U. In the latter case, additional neutron absorptions would produce ^{235}U and ^{236}U. Because of the relatively long

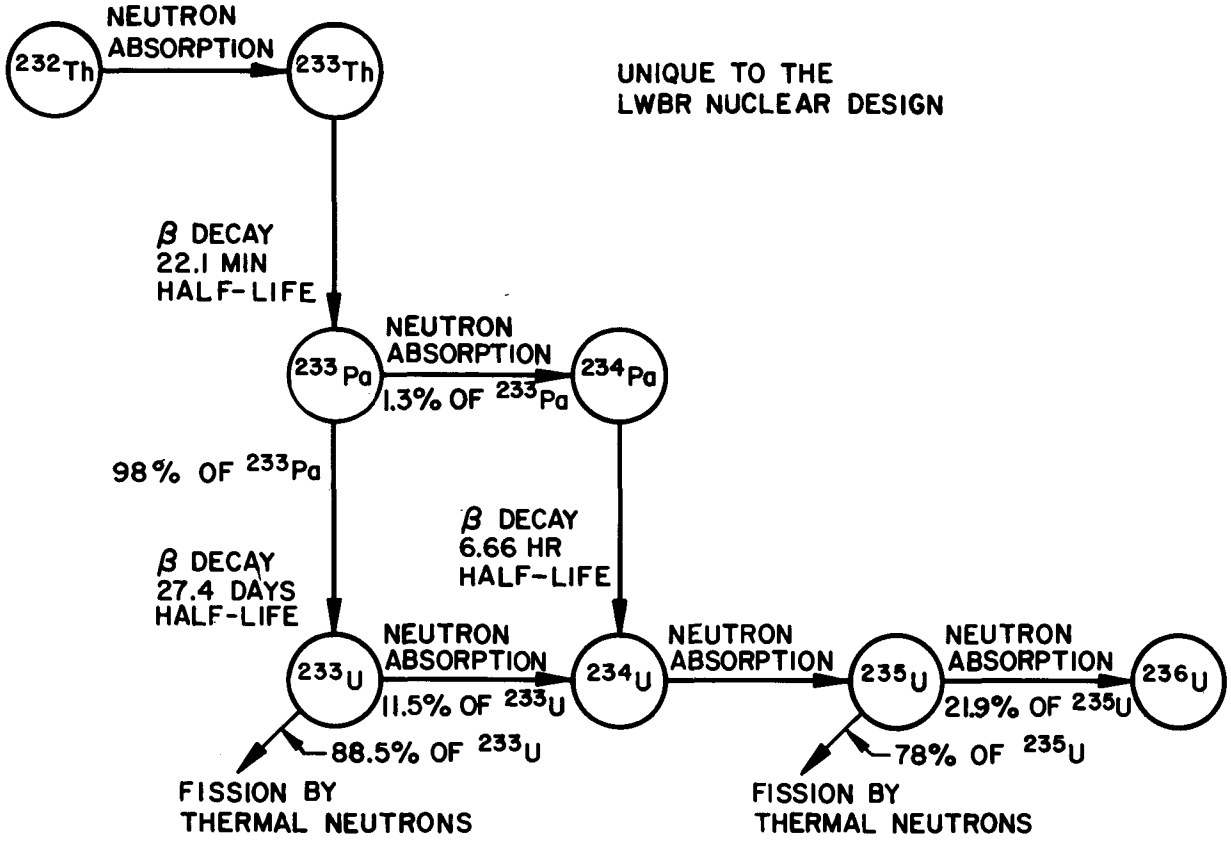

Figure 1. Thorium-232 to Uranium Breeding Process

half-life of protactinium, its buildup during operation and its decay after shutdown result in a very slow reactivity transient. During operations, the buildup of protactinium reduces core reactivity and, after shutdown, the decay into ^{233}U increases core reactivity.

Nuclear design of the LWBR core utilized a seed-blanket concept similar to that successfully applied to the first two PWR cores operated at Shippingport (Reference 2), but with reactivity control provided by core geometry changes (movable fuel) instead of poison rods. The seed-blanket concept provided flexibility for separately optimizing the two core regions to carry out their individual functions: the seed to provide neutrons as efficiently as possible in the burning of the fissile fuel, and the blanket and reflector regions to utilize the neutrons efficiently in producing new fissile fuel by neutron absorption in the fertile fuel. In LWBR, the seed, blanket, and reflector were each optimized to maximize neutron absorption in thorium and to minimize neutron loss.

1.2.2 - Thermal and Hydraulics

The fundamental thermal design objective for LWBR operation was the assurance that critical heat flux (CHF) was not exceeded for steady state, full-power operation and transient operation, including the design accidents, that could occur during core life.

To assure the thermal-hydraulic design objective, the core flow distributions were optimized between the blanket and seed regions to provide the desired core operating lifetime at design full-power conditions.

A diagram of the LWBR core flow path is presented in Figure 2. The flow entered the reactor vessel through four bottom inlet nozzles, where a portion of it was routed between the vessel and outer thermal shield barrel to cool both the vessel and thermal shield. This flow rejoined the main coolant stream above the reactor inlet flow baffle, and the flow proceeded into the core. The reactor inlet baffle acted as a flow straightener.

The total flow entering the core region was distributed by differential orificing of the blanket and reflector flow paths. About 27 percent of the

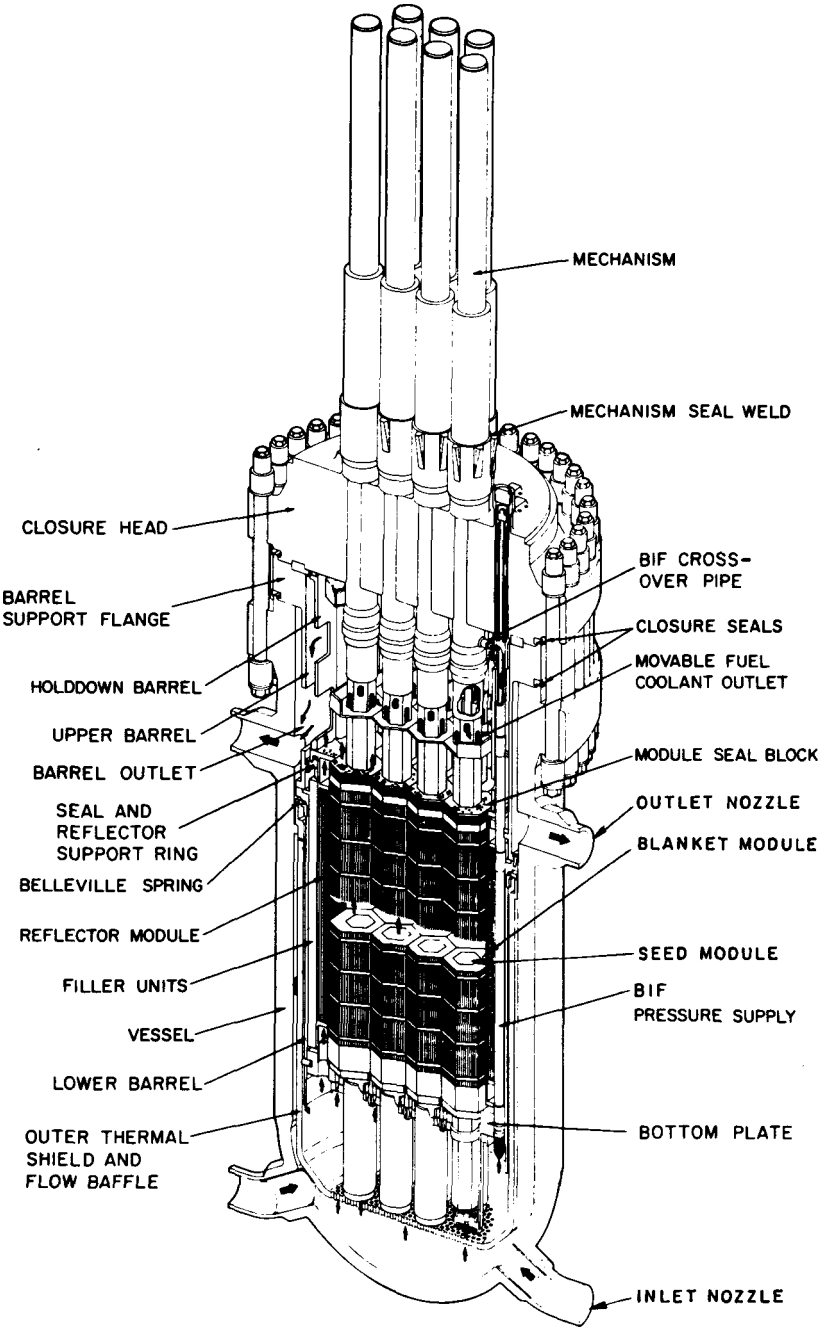

Figure 2. LWBR Core in Shippingport Reactor Vessel

core flow went to the seed region, 54 percent to the standard blanket/power flattening blanket, and 10 percent to the reflector region. The remaining 9 percent was apportioned to the bypass inlet flow (BIF) balancing system and leakage paths. The outlet plenum served as a mixing chamber for the flow before the coolant exited the vessel through the top outlet nozzles.

The LWBR BIF (hydraulic force balancing system) was designed to ensure reliable operation of the movable fuel assemblies for normal and rapid negative reactivity insertion control requirements.

Figure 3 presents a schematic representation of the bypass inlet flow balancing system, which assured control element insertion during scram. The control drive mechanism was attached to the top of the balance piston. As shown, a downward-acting pressure force was developed across the balance piston by routing higher-pressure inlet flow around the core in low hydraulic resistance conduits to locations above each balance piston. The piston was sized so that the steady state downward force from above the piston counterbalanced the upward hydraulic force on the movable module so that gravity provided a net downward force on the movable module. Consequently, upon receipt of a scram signal, each movable assembly unlatched and accelerated downward under the force of gravity until the terminal velocity for downward motion was achieved.

A hydraulic buffer was incorporated into each BIF system to limit the contact velocity when a seed module reached the full down position and to prevent damage to components.

1.2.3 - Core Mechanical Description

Figure 2 shows positioning of the LWBR core and related components in the Shippingport reactor vessel. The components are labeled and the coolant flow path is indicated for this single-pass core.

A cross-section view of the LWBR core is given in Figure 4. The binary fuel was contained in 12 hexagonally shaped modules. Each module had a central movable fuel region (seed) and was surrounded by a stationary blanket. The fuel was in the form of ceramic pellets, which were either thoria pellets

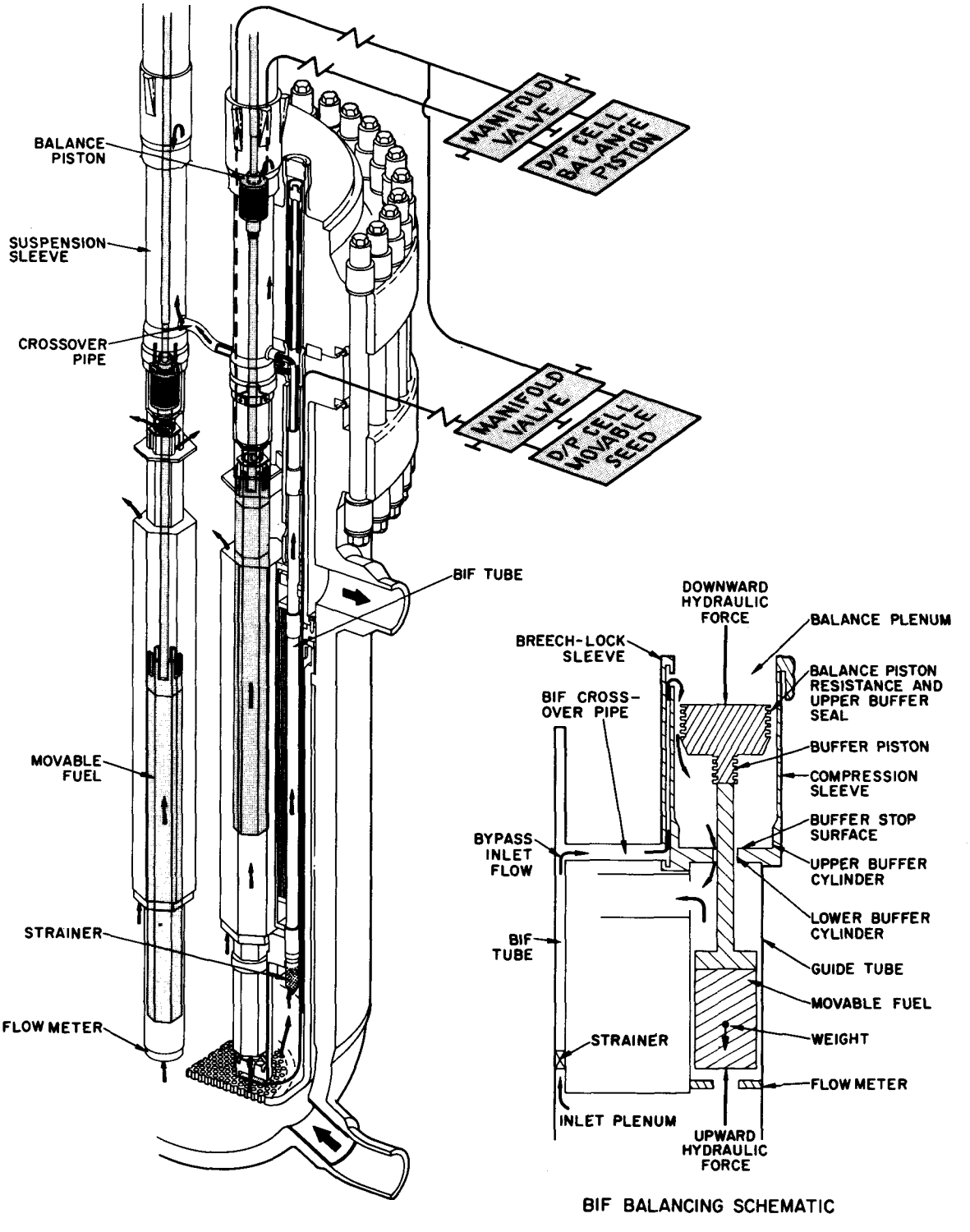

Figure 3. Bypass Inlet Flow Balance System

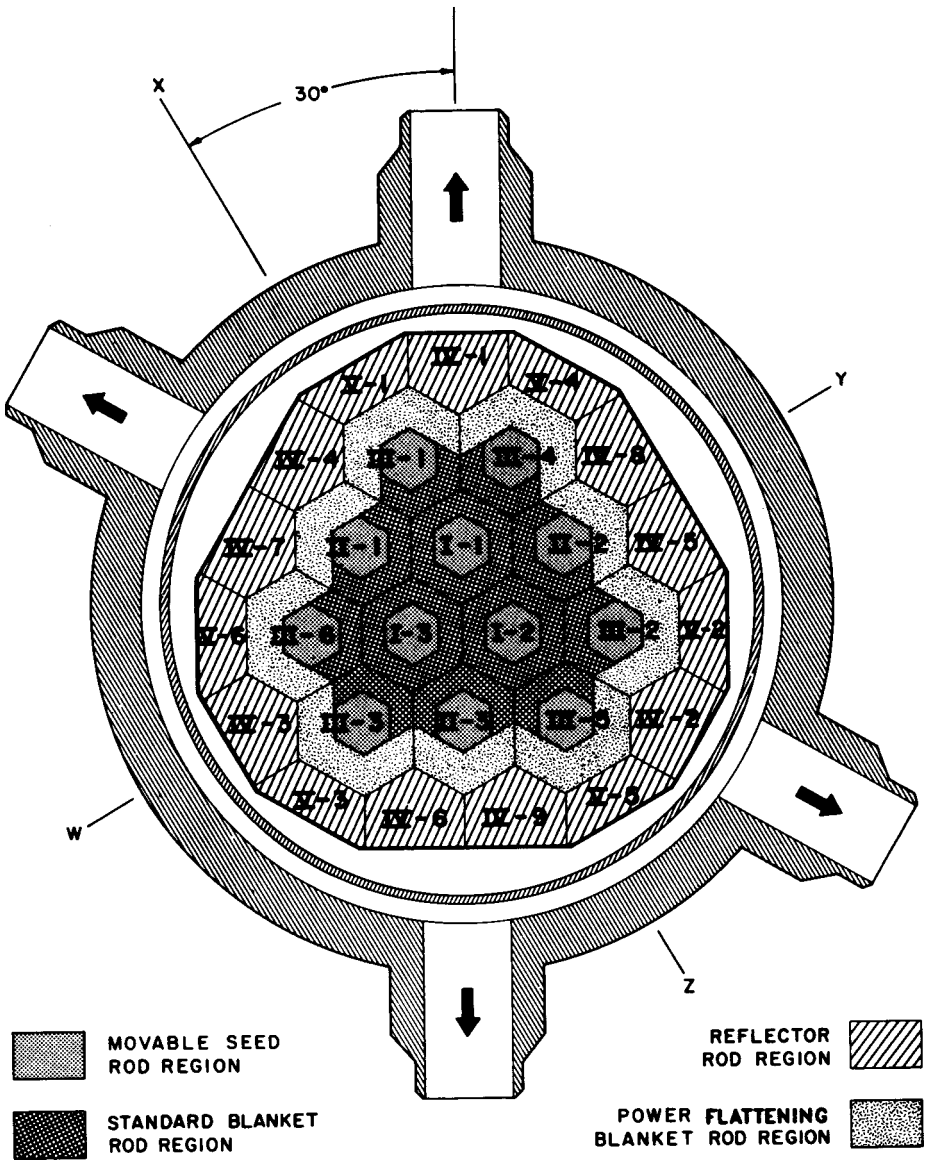

Figure 4. Cross Section Module Identification

or a mixture of urania and thoria (binary fuel) pellets. The pellets were contained within Zircaloy cladding. The fuel was distributed over 104 inches in height, which includes a 10-inch high ThO_2 reflector above and below the binary fuel. Fifteen reflector modules consisting of rods with only thoria pellets were located on the outer periphery of the core.

Axial positioning of the individual movable seeds was accomplished by a collapsible-rotor, reluctance-type control drive mechanism similar to those used successfully during operation of the first two Shippingport cores. When energized, the LWBR mechanism was connected to a drive screw that supported the seed. Safety shutdown was accomplished by deenergizing the control drive mechanism stator, thus collapsing the rotor and releasing the drive screw. This permitted the movable fuel to drop into its least reactive (lowest) position. A continuously engaged out-motion latch was incorporated in the mechanism to provide positive prevention of any unsignaled up-motion of a seed module. A net downward force on the module was achieved under all conditions of flow by the use of the BIF balance system (Figure 3). A buffer region was incorporated to prevent excessive forces on the movable assemblies as they came to rest during insertion. This method of reactivity control improved neutron economy.

The blanket modules were stationary as were the 15 reflector modules around the core periphery. Stainless steel filler units surrounded the reflector to fill the space between the flat surfaces of the modules and the cylindrical inner surface of the barrel. The filler units limited the leakage flow that bypassed the core in this region.

1.2.4 - Fuel Element Design

The LWBR fuel elements were designed to complement the nuclear, thermal and hydraulic, and mechanical requirements of the reactor. Several unique fuel element design features were required to meet the LWBR objective and guarantee the primary goal of neutron economy in the interest of breeding.

Four fuel rod regions (seed, standard blanket, power flattening blanket, and reflector) were utilized in LWBR. These regions are identified in

Figure 4. The fuel rods in each of these regions were of different diameter and initial uranium loadings. In addition, radial and axial variations of fuel loading were employed in every region except the reflector. A total of 23 different rod types were used.

To improve neutron economy, the blanket and reflector fuel elements were designed with nonfreestanding, thin-walled Zircaloy-4 tubing, highly cold worked and stress relief annealed. The seed fuel rods, because of their higher duty demands, were fabricated with freestanding recrystallization-annealed Zircaloy-4 cladding. All cladding was fabricated from selected Zircaloy-4 ingots with less than 50 ppm hafnium content which is lower than normal, to reduce parasitic absorption of neutrons. Also, in the interest of neutron economy, both the number of fuel support grids and the spacing between fuel rods were minimized. Details of the fuel rod design are given in Sections 3 and 4, and the fuel rod performance considerations are described and evaluated in Section 5.

Two additional unique features of the LWBR fuel system were the movable seed fuel modules (to provide reactivity control) and fuel rods fixed at either the top or bottom baseplate. The movable seed was used to control reactivity by effectively utilizing the thorium as a control poison, thereby eliminating separate neutron-absorbing control rods. The mounting of the LWBR fuel rods was such that approximately equal numbers of fuel rods were bolted to the top and bottom baseplates. This mounting arrangement was employed to equalize axial forces on the support grids.

The unique demands and features of the LWBR fuel elements and the methods used to predict fuel rod performance form the basis of this report. Also discussed are fabrication problems that affected fuel element design and lessons learned in design and fabrication of the LWBR fuel elements.

SECTION 2 - OPERATIONAL REQUIREMENTS AND ENVIRONMENTAL CONDITIONS

2.1 - DUTY REQUIREMENTS

Figure 5 and Table 1 give the duty requirements for each of the LWBR fuel regions at the maximum operating power. Maximum operating power was 100 percent of core rated power to 18,000 effective full power hours (EFPH), 80 percent from 18,000 to 27,400 EFPH, then was decreased gradually to 57 percent at 29,047 EFPH. Power was decreased in extended lifetime (beyond 18,000 EFPH) to safeguard the fuel rods as described in Reference 3. Further power decreases occurred near end of life to maintain criticality as the fuel depleted. The curves in Figure 5 represent the upper envelope of linear power output of a fuel rod at any axial or radial position in the region as a function of fuel burnup. The design curves include the upper 2-sigma extreme of all uncertainty factors to maximize power and burnup. The best estimate curves include only the bias portion of the uncertainty factors.

Table 1 gives the peak local power and burnup of each region at maximum operating power, consistent with the design curves of Figure 5. The burnup values are given at 18,000 and 29,047 EFPH, which were the design lifetime and the subsequently extended actual lifetime, respectively. The table also provides the peak fast neutron (>1 Mev) fluence in each region at 18,000 and 29,047 EFPH.

2.2 - OPERATIONAL REQUIREMENTS

Table 2 gives the operational requirements for the LWBR fuel elements. These requirements are based on an 18,000 EFPH, 6-year design lifetime. For each listed operation, the table gives the allowable power range, power change rate, primary system pressure, and the expected number over the design lifetime. The listing includes operations of normal startup, controlled shutdown, scram, plant load follow (swing load operation), load transients, and pressure-power cycling.

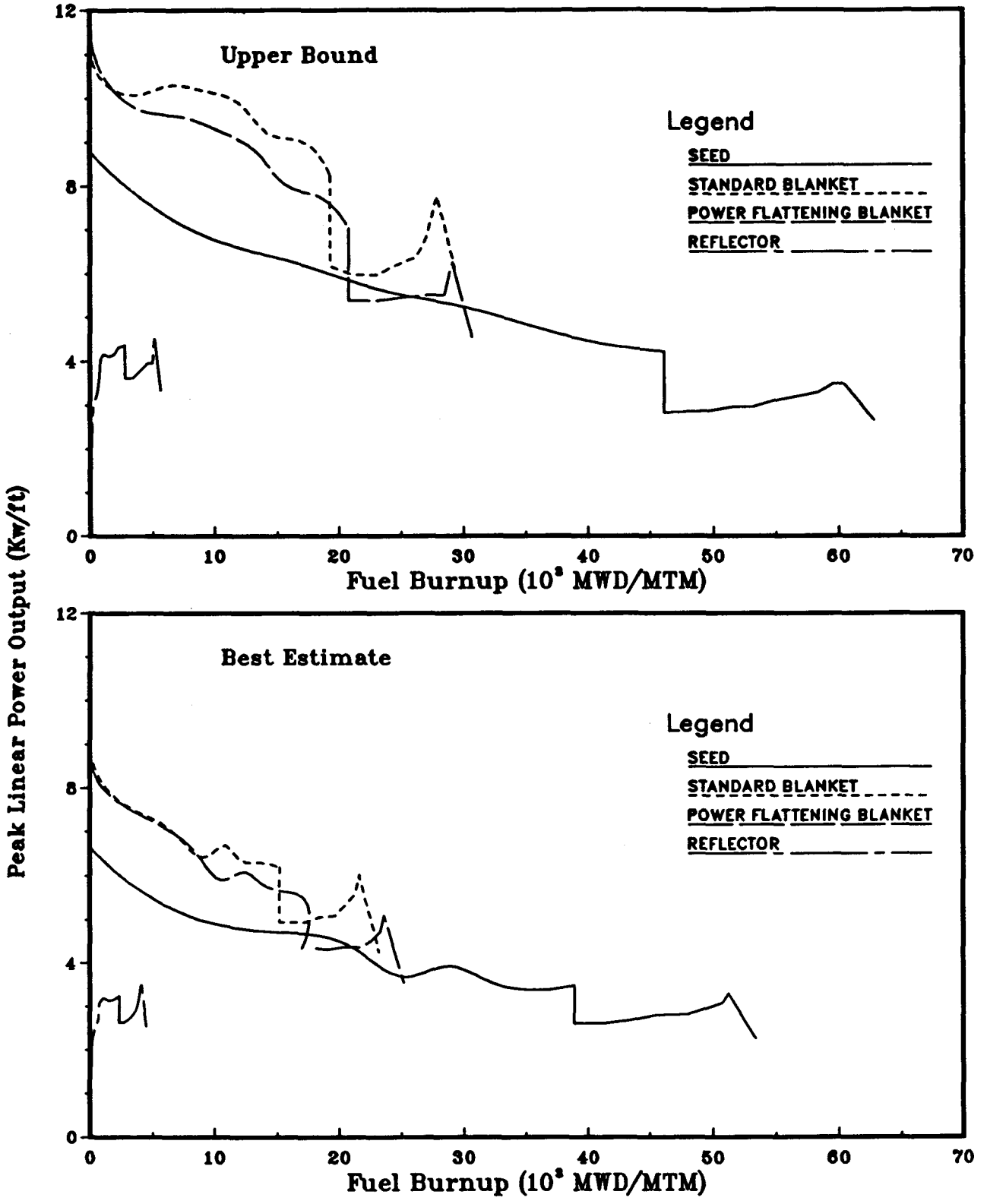

Figure 5. Power Duty Requirements

Table 1 - Peak Local Linear Power Rating, Burnup, and Fluence for Each of the LWBR Fuel Regions

Parameter	Fuel Region			
	Seed	Standard Blanket	Power Flattening Blanket	Reflector
Peak Linear Power (kw/ft)				
Best Estimate	6.7	8.9	8.7	3.6
Design	8.8	11.7	11.5	4.7
Peak Depletion (10^{20} f/cc)				
Best Estimate at 18,000 EFPH	8.3	3.4	3.9	0.5
Best Estimate at 29,047 EFPH	11.4	5.3	5.7	1.0
Design at 18,000 EFPH	9.7	4.3	4.6	0.6
Design at 29,047 EFPH	13.4	6.7	7.0	1.3
Peak Burnup (MWD/MTM)				
Best Estimate at 18,000 EFPH	38,900	15,200	17,000	2,400
Best Estimate at 29,047 EFPH	53,400	23,200	25,200	4,500
Design at 18,000 EFPH	45,300	19,000	20,500	2,800
Design at 29,047 EFPH	62,500	29,600	30,800	5,600
Maximum Rod - Average Depletion (10^{20} f/cc)				
Best Estimate at 18,000 EFPH	4.4	2.0	2.2	0.3
Best Estimate at 29,047 EFPH	6.4	3.0	3.3	0.5
Design at 18,000 EFPH	4.7	2.2	2.5	0.3
Design at 29,047 EFPH	7.0	3.5	3.8	0.6
Maximum Rod - Average Burnup (MWD/MTM)				
Best Estimate at 18,000 EFPH	20,500	8,700	9,800	1,200
Best Estimate at 29,047 EFPH	29,800	13,200	14,700	2,200
Design at 18,000 EFPH	22,100	9,700	10,900	1,300
Design at 29,047 EFPH	32,900	15,500	16,800	2,700
Peak Fluence (10^{20} n/cm^2, >1 Mev)				
Best Estimate at 18,000 EFPH	66.3	48.4	38.5	17.7
Best Estimate at 29,047 EFPH	96.5	73.8	58.6	27.8
Design at 18,000 EFPH	70.3	53.8	44.0	20.0
Design at 29,047 EFPH	104.7	84.0	69.0	32.1

Table 2 - Operational Requirements of LWBR Fuel Elements

Requirement	Power Range (Mw(e))	Rate of Power Change (Mw(e)/min.)	Primary System Pressure (psia)	Number Over a 6-Year Design Life
Normal Startups	0 to 15	<3.5	2000 ±30	132
Controlled Shutdowns	<15 to 0	≤3.5	2000 ±30	60
Scrams	Any Power to 0 Power	Instantaneous	2000 ±30	72
Plant Load Follow (Swing Load Operation)	15 to 72 or 72 to 15	≤3.5	2000 ±30	1095
Load Transients	±20	≤25	2000 ±30	12,000
Pressure-Power Cycles	0 to 72	Any Rate	<1000 to 2000 to <1000	30

2.3 - ENVIRONMENTAL CONDITIONS

Table 3 lists the environmental conditions to which the LWBR fuel elements were designed for 18,000 EFPH operation. As described later and in Reference 3, operations beyond 18,000 EFPH required reductions in coolant temperature and system pressure as well as the power reductions described above. Coolant average temperature was decreased one time, only at 18,000 EFPH, for operations throughout extended lifetime. The decrease was 10F, from 531F to 521F. System pressure was decreased in four steps to 1615 psia and maintained at that level throughout extended lifetime. Unless noted for specific design concerns in Section 5, seed rod performance was conservatively evaluated on the basis of 2000 psia for operations to 18,000 EFPH.

Table 3 - Environmental Conditions for Operation to 18,000 EFPH

Inlet Temperature (F)	520
Average Temperature (F)	531 ±3
Outlet Temperature (F)	543
Total Reactor Flow (lb/hr)	32×10^6
Thermal Power (Mw)	236.6
Electrical Power (Mw(e) gross)	72
Nominal Pressure (psia)	2000 ±30
Nominal Flow Region Velocities for Four-Loop Flow (ft/sec):	
Seed	17.3
Standard Blanket	13.2
Power Flattening Blanket	16.7
Reflector	4.7

2.4 - TRANSIENTS AND ACCIDENTS

Fuel rod performance for LWBR was evaluated for accident conditions which could produce peak power levels higher than the full-power ratings shown in Figure 5 and Table 1 and for accidents where fuel element heat removal is reduced. These overpower transient conditions are of short duration, and usually terminated in seconds or minutes by the automatic control systems. A brief description of each is presented below. The loss-of-flow accident was accommodated in reactor design with flywheel generators to reduce the rate of flow coastdown and to provide thermal capability.

1. Reactivity Insertion Transient

   A reactivity insertion transient (RIT) is defined as a power excursion resulting from the uncontrolled addition of reactivity to a reactor core. Such a transient could occur either during reactor startup (sub-power range) or during reactor operation in the power

range. Positive reactivity could be added to the LWBR core by lifting the movable fuel modules or by introducing cold primary coolant into the core. Also, decay of xenon and other fission product poisons in the core would introduce positive reactivity. The most severe RIT in the LWBR concept was that resulting from accidental withdrawal of the movable fuel modules resulting in a peak power of 128 percent of full rated power. Fuel rod capability to withstand this overpower transient is evaluated in Section 5.

2. Loss-of-Coolant Accident

It was required to demonstrate the capability of the LWBR safety injection system to prevent excessive fuel element temperatures and subsequent fission product release if a postulated loss-of-coolant accident occurred, assuming that one-half of the safety injection system failed to operate.

3. Steam Line Rupture and Oversteam Demand Accidents

A sudden and excessive demand for steam from one or more of the steam generators could cause excessive cooling of the primary coolant and result in increased reactivity. The sudden steam demand could be caused by a breach of integrity of the secondary steam system, or by an oversteam demand caused by operator error or failure of the turbine load limit and speed changer governor controls. These types of accidents are termed steam line rupture accidents and oversteam demand accidents, respectively. As a class, the steam line rupture accidents are more severe than the oversteam demand accidents because the rate of primary coolant temperature reduction is higher and the core power becomes asymmetric during the transients. Fuel rods were protected against damage from all steam line rupture accidents since reactor power would not exceed 128 percent and the minimum design power ratio was greater than 1.05.

4. Cold Water Accident

Reactivity could be accidentally increased by rapid cooling of the primary system, possibly caused by the addition of coolant having a temperature less than that of the normal coolant temperatures.

Because of the negative temperature coefficient of reactivity of the moderator (coolant), the reactivity of the reactor (and thus the power level) increased when the moderator was cooled. The reactivity remained high in the absence of corrective measures until the moderator temperature increased to its normal level. The lowered temperature of the coolant water decreased the effectiveness of the power-to-flow scram signal and hot-leg temperature scram signal because the cold water attenuated the neutron flux at the detector and lowered the coolant hot leg temperature. This negated the utility of the hot-leg temperature scram signal for cold water accidents. As the core inlet temperature decreased to drive the power transient, the nuclear instrument signal was attenuated and the effective trip point of the high power-to-flow scram signal increased because of the temperature attenuation error.

Since power excursions resulting from cold-water accidents in LWBR had the potential to heat the fuel elements beyond the LWBR design limits, cold water accidents were prevented by interlocks and operating procedures.

5. Anticipated Transients Without Scram

A deviation from normal operating conditions which might be expected to occur one or more times during the life of the reactor plant is called an "anticipated transient". Anticipated transients may demand action of the nuclear protection system, which may fail concurrently. The definition of anticipated transients excludes major coolant line ruptures, major steam line ruptures, and other similar very low probability accidents. Examples of anticipated transients include inadvertent opening of primary or secondary relief valves, rapid load increases and decreases, and various loss-of-flow accidents.

Postulating a set of "anticipated" conditions for which a scram is expected to occur, but for which it does not, results in an anticipated transient without scram (ATWS) event. Analysis of LWBR operations showed that the plant had sufficient capability to limit the consequences of an ATWS to acceptable levels in the improbable event that one should occur.

6. Mechanism Nozzle Rupture Accident

Each of the 12 movable fuel assemblies (seed modules) was driven by a control drive mechanism. In the unlikely event of rupture of the mechanism nozzle, hydraulic pressure above the balance piston would be relieved and upward fuel motion could result. A holddown structure was installed above the control drive mechanisms to prevent ejection of a mechanism and to limit upward fuel motion. The amount of fuel motion that could occur would result in a power excursion. Nuclear analysis of the power excursion for an upward fuel shift showed that the power transient in the affected module would peak at 638 percent power in 0.1 second due to Doppler feedback on reactivity. Scram protection would then return power below 100 percent in less than 1 second. Worst-case fuel rod assessments indicated that fuel and cladding temperature would remain below melting due to the short duration of the power transient.

Analyses of postulated failures in the bypass inlet flow nozzle showed the corresponding upward force and movable fuel assembly displacement to be insignificant in comparison to the mechanism nozzle rupture accident.

SECTION 3 - MECHANICAL DESIGN OF THE FUEL RODS

3.1 - GENERAL DESCRIPTION

Fuel elements in the LWBR core were composed of right circular cylindrical fuel pellets stacked inside a hollow cylindrical tube. The tube was closed off at both ends with solid cylindrical shouldered end plugs welded to the tube. Within the tube and above the fuel stack, there was a plenum void to house the plenum spring, to allow fuel stack expansion, to accept fission gas released from the fuel, and to minimize internal gas pressure. The plenum spring maintained pellet stack continuity, and a surrounding support sleeve prevented tube collapse in the standard blanket, power flattening-blanket, and reflector fuel rods. The seed tubing was freestanding because it had a thicker wall relative to its diameter; thus, a support sleeve was not required. The plenum sleeve was permanently attached to the top end plug by means of a tight-fitting pin through the holes aligned in the sleeve and end plug insert inside the sleeve. The clearance between the bottom of the sleeve and the top of the pellet stack accommodated differential axial movement of the pellet stack relative to the cladding. Fuel ends were dished to minimize pellet stack axial elongation.

Cladding diameters and wall thicknesses of the LWBR fuel rods, as well as the physical characteristics of both the binary and thoria fuel pellets are listed in Table 4. Table 5 gives the materials of construction of the fuel rod components. Drawings of the fuel rods and components are shown in Figures 6 through 8. These figures provide the nominal dimensions for the seed (Figure 6), blanket (Figure 7), and reflector (Figure 8) fuel rods and components. Cross sections of typical fuel pellets for all rod types are shown in Figure 9.

The different rod types required different pellet geometries. Edge chamfers were ground on the edges of all seed pellets and blanket thoria pellets. Blanket binary pellets were tapered at the ends. Reflector pellets were ground with square edges. Each of these geometries was required for reasons of fabrication or fuel rod performance as described in Section 4. Their predicted effects on fuel rod performance are given in Section 5.

Table 4 - Fuel Element Dimension Specifications*

Zircaloy-4 Cladding	Seed	Standard Blanket	Power Flattening Blanket	Reflector
Outside Diameter	0.306 ± .0015 avg +.003 -.002 local	0.5715 ± .0015 avg ± .0025 local	0.5275 ± .0015 avg ± .0025 local	0.832 ± .003 avg ± .003 local
Inside Diameter	0.262 ± .002 local ± .001 avg	0.516 ± .002 local ± .001 avg	0.475 ± .002 local ± .001 avg	0.748 ± .001 avg ± .0025 local
Nominal Wall Thickness	0.022	0.02775	0.02625	0.042
Outside Diameter to Thickness Ratio	13.9	20.6	20.1	19.8
Cladding Heat Treatment**	RXA	SRA	SRA	SRA
UO_2-ThO_2 Fuel Pellets				
Diameter	0.252 ± .0005	0.5105 ± .0005	0.4695 ± .0005	-
Length	0.445 ± .020	0.530 ± .020	0.870 ± .020	-
	0.615 ± .020	0.870 ± .020	0.785 ± .020	-
		0.785 ± .020	0.700 ± .020	-
End Shoulder Width	0.046 ± .008	0.055 ± .015	0.055 ± .015	-
Endface Dish Depth	0.009 ± .003	0.014 ± .004	0.014 ± .004	-
Chamfer or Taper- Depth	0.015 ± .005	0.001 - 0.004	0.001 - 0.004	-
Length	0.015 ± .015	0.100 - 0.200	0.100 - 0.200	-
Range of Individual Pellet Densities, % of Theoretical	94.55 - 99.27	96.55 - 99.38	95.26 - 98.60	-
Fuel-Cladding Diametral Gap	0.0085 - 0.0115	0.004-0.007	0.004-0.007	-
ThO_2 Fuel Pellets				
Diameter	0.2555 ± .0005	0.5105 ± .0005	0.4695 ± .0005	0.7415 ± .0005
Length	0.530 ± .020	0.615 ± .020	0.445 ± .020	0.740 ± .060
End Shoulder Width	0.055 ± .010	0.055 ± .010	0.055 ± .010	0.074 ± .010
Endface Dish Depth	0.009 ± .003	0.014 ± .004	0.014 ± .004	0.014 ± .004
Edge Configuration	0.015 ± .005 Chamfer	0.006 ± .004 Chamfer	0.006 ± .004 Chamfer	Square Edge
Range of Individual Pellet Densities, % of Theoretical	95.14 - 99.75	93.10 - 99.36	95.37 - 99.95	93.08 - 99.08
Fuel-Cladding Diametral Gap	0.005 - 0.008	0.004 - 0.007	0.004 - 0.007	0.005 - 0.008

* All dimensions are in inches, except as noted.
** RXA = Recrystallization Annealed
SRA = Stress Relief Annealed

Table 5 - Materials of Construction

Item	Material	Source
Cladding Tube	Zircaloy-4	Seamless Tubing
Fuel Pellets:		
Binary	UO_2-ThO_2	Compacted Powder
Thoria	ThO_2	Compacted Powder
End Plugs	Zircaloy-4	Rod Stock
Support Sleeve	348 Stainless Steel	Seamless Tubing
Pin	304 Stainless Steel	Bar Stock
Spring	Inconel X-750	Wire
Fuel Rod Nut	Zircaloy-4	Rod Stock

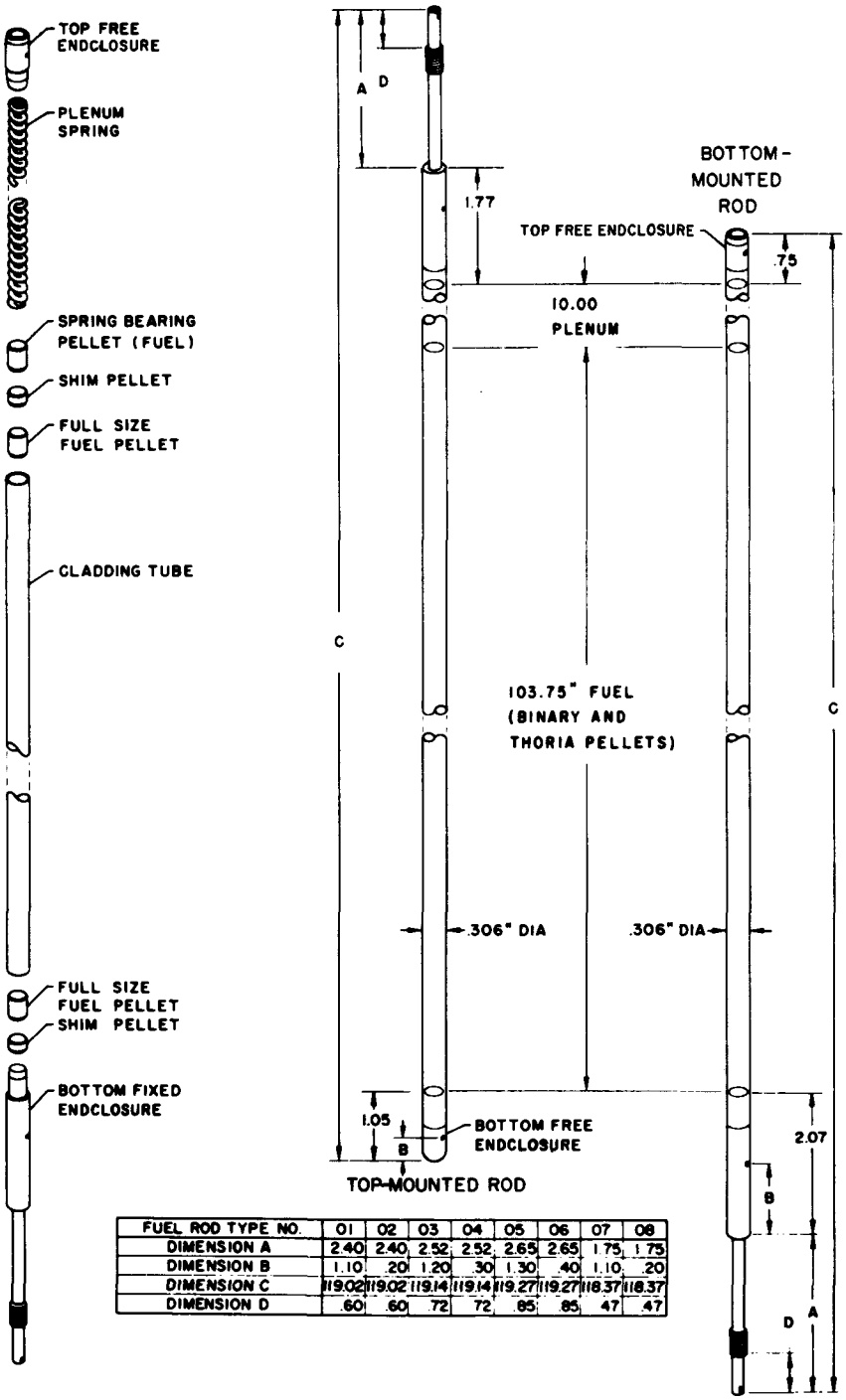

FUEL ROD TYPE NO.	01	02	03	04	05	06	07	08
DIMENSION A	2.40	2.40	2.52	2.52	2.65	2.65	1.75	1.75
DIMENSION B	1.10	.20	1.20	.30	1.30	.40	1.10	.20
DIMENSION C	119.02	119.02	119.14	119.14	119.27	119.27	118.37	118.37
DIMENSION D	.60	.60	.72	.72	.85	.85	.47	.47

Figure 6. General Dimensions and Components of Seed Fuel Rods

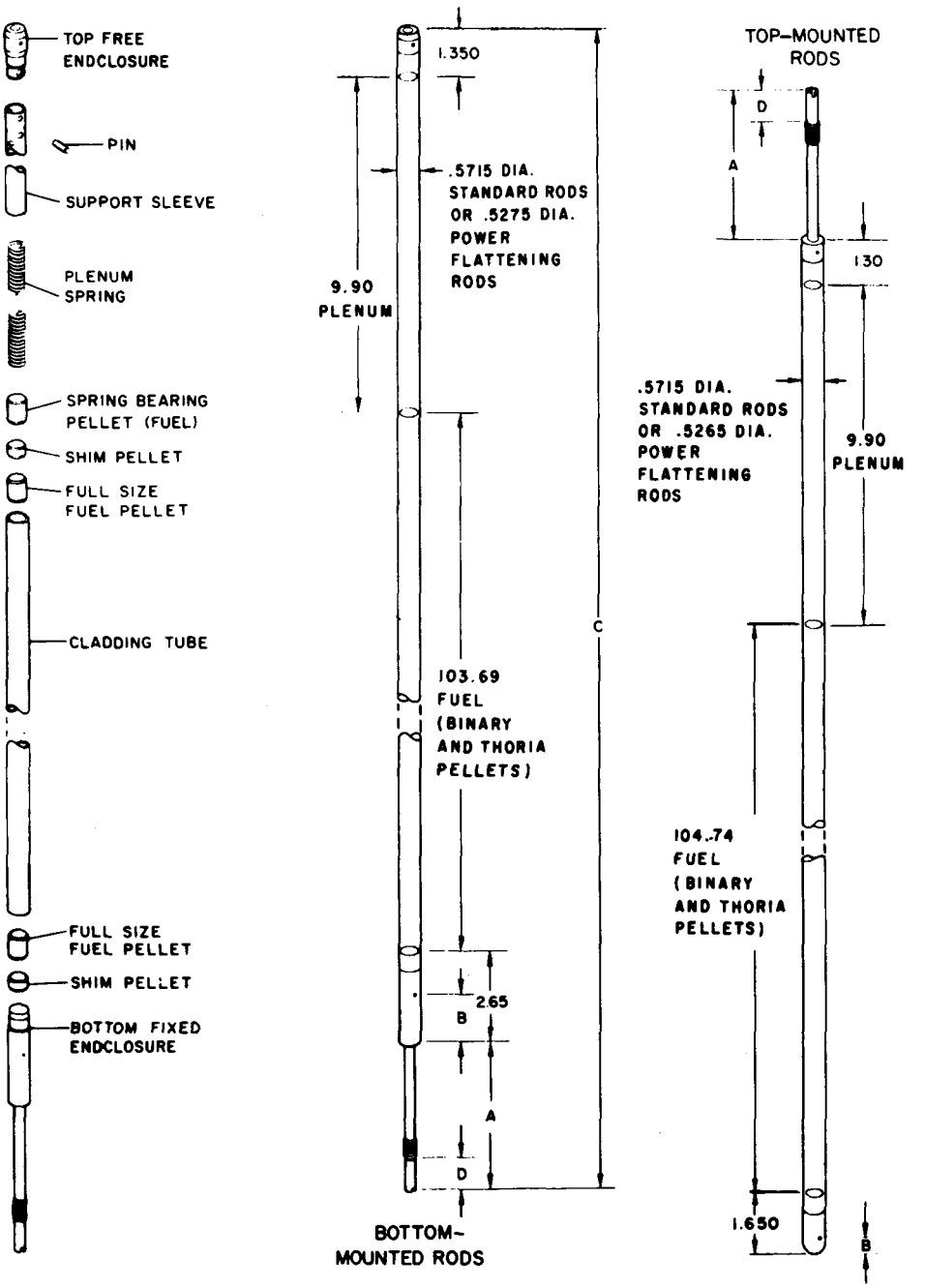

FUEL ROD TYPE NO.	11	12	13	14	15	16	21	22	23	24	25	26	27
DIMENSION-A	4.23	4.23	4.35	4.35	4.47	4.47	4.23	4.23	4.35	4.35	4.47	4.47	4.60
DIMENSION-B	1.40	50	1.50	.60	1.60	.70	1.70	.80	1.80	.90	1.90	1.00	2.00
DIMENSION-C ± .07	121.9	121.9	122.0	122.0	122.1	122.1	121.9	121.9	122.0	122.0	122.1	122.1	122.3
DIMENSION-D	.78	.78	.90	.90	1.03	1.03	.78	.78	.90	.90	1.03	1.03	1.16

Figure 7. General Dimensions and Components of Blanket Fuel Rods

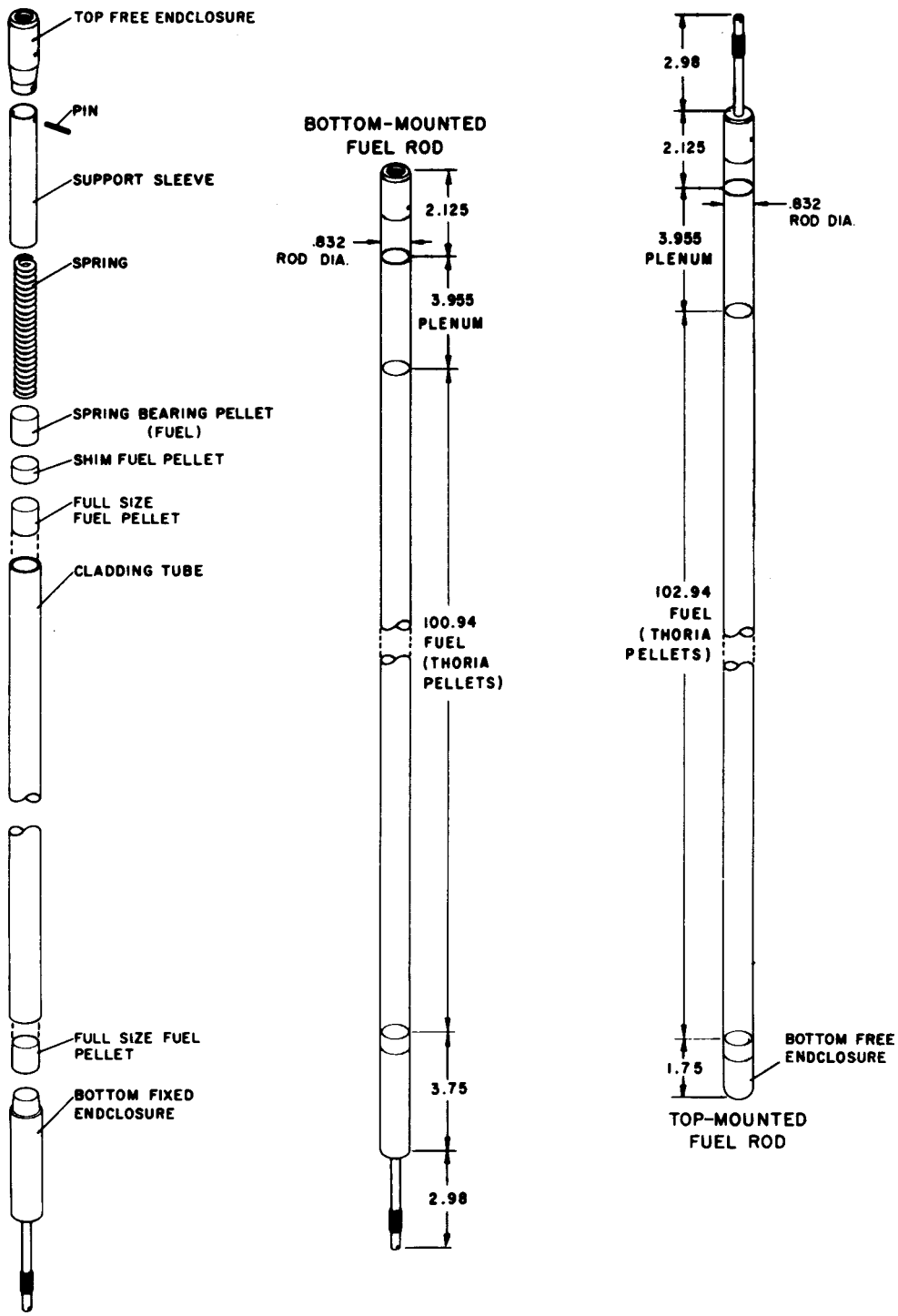

Figure 8. General Dimensions and Components of Reflector Fuel Rods

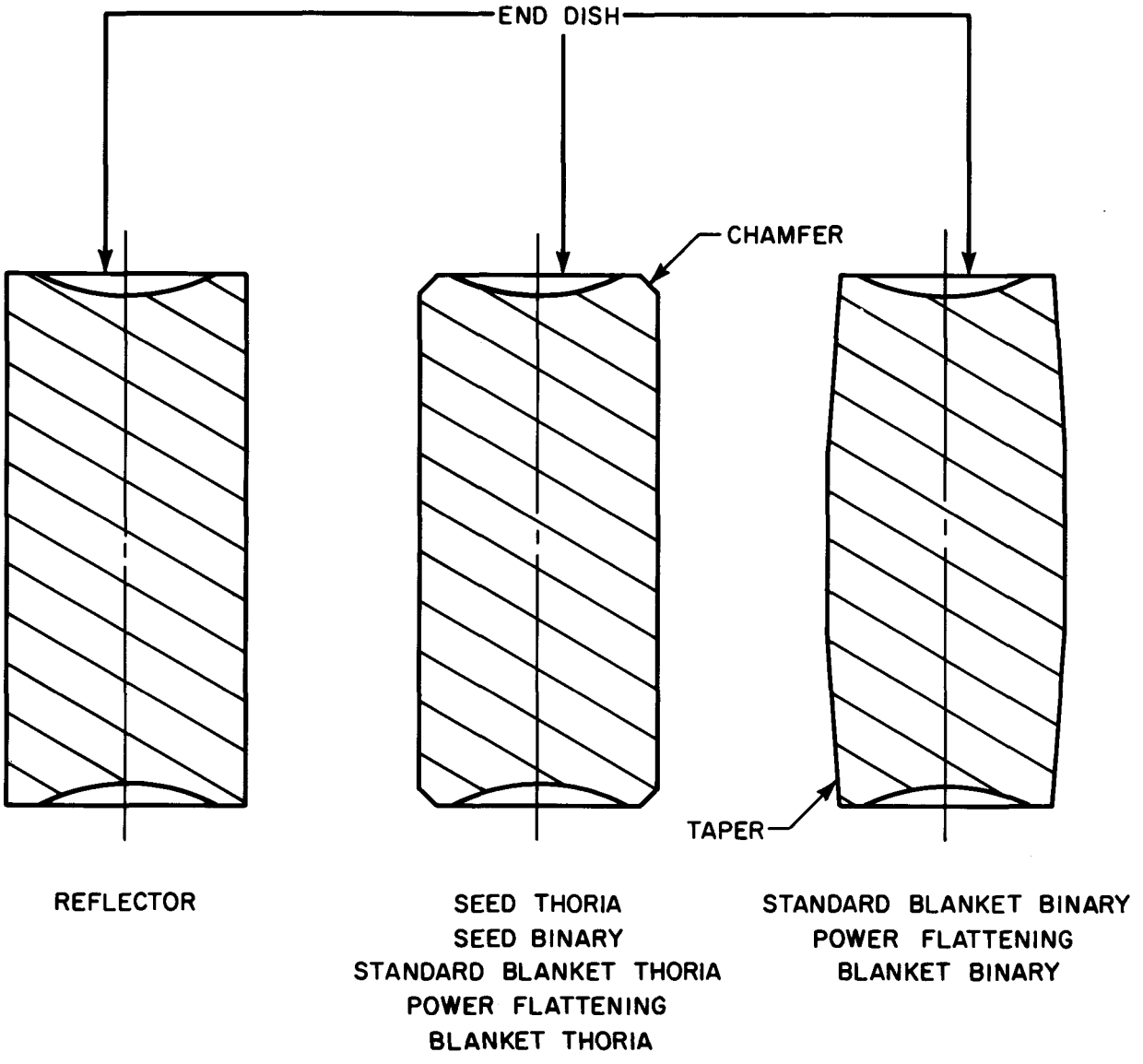

Figure 9. Cross Sections of Typical LWBR Fuel Pellets

(Intentionally Blank)

SECTION 4 - UNIQUE FEATURES OF THE FUEL ROD DESIGN

Because of the unique breeding demands of the light water breeder reactor, the LWBR fuel elements were fabricated with many features which had never been used in fuel elements of commercial reactors. A discussion of these unique features and the design concerns that evolved from the fuel elements is presented in the following subsections.

4.1 - URANIUM-233 FUEL

Uranium-233 is chemically similar to the uranium used in the commercial nuclear power industry. However, it does have two unique features of importance to the operation of LWBR.

First, ^{233}U was selected for the fissile fuel for LWBR because it has the largest neutron regeneration factor* in the thermal and epithermal region of any of the potential fissile fuels (^{239}Pu, ^{241}Pu, and ^{235}U and ^{233}U). Indeed, ^{233}U is the only fuel capable of breeding in a light water cooled reactor. During lifetime, the ^{233}U fuel inventories decrease in the seed and standard blanket regions and build up in the power flattening blanket and reflector regions.

Second, the fission product yield is different for ^{233}U than for ^{235}U. About twice as much iodine is produced, which has the following impact: Based on out-of-pile data, doubling the amount of iodine would decrease the threshold stress for iodine stress corrosion cracking in the cladding by about 12 percent. The increased iodine and lower threshold stress would be a direct penalty for the ^{233}U fuel system if the fuel system iodine release rate were the same as for the normal ^{235}U-based system. However, ^{233}U has a much lower total fission gas release at typical operating heat flux conditions. Under the assumption that the release of iodine is proportional to the total fission gas release, ^{233}U in thoria is actually a factor of two and one-half better (less iodine release) than the normal uranium system resulting in an increase of threshold stress by 19 percent.

---

*Neutron regeneration factor, symbolized by η, is the average number of neutrons produced in fission per neutron absorbed in fissile fuel.

4.2 - URANIA-THORIA FUEL SYSTEM

The thorium cycle is used in the LWBR to convert fertile ^{232}Th to fissile ^{233}U. The thorium cycle was employed to take advantage of the high thermal neutron regeneration factor of ^{233}U to provide as large an excess of neutrons as possible during the depletion of fissile fuel. These excess neutrons are utilized efficiently in the production of fissile ^{233}U by neutron capture in fertile ^{232}Th.

As illustrated in Figure 1, the thorium cycle proceeds by neutron absorption in ^{232}Th to form ^{233}Th, which quickly β-decays (22-minute half-life) to form ^{233}Pa. Protactinium-233 β-decays with a 27-day half-life to ^{233}U. The presence of ^{233}Pa in the core means that power densities lower than those of a commercial PWR lead to improved breeding performance. In addition, ^{233}Pa induces long-lived (compared to xenon) reactivity transients in the core.

Thorium-232 also undergoes an (n, 2n) reaction to produce ^{231}Th, which β-decays with a 25-hour half-life to ^{231}Pa. A subsequent neutron capture leads to ^{232}Pa, followed by another β decay with a 32-hour half-life to ^{232}U. The ^{232}U is radioactive and decays through a chain of five successive α particle emissions to ^{212}Pb and, by additional β and α emission, to ^{208}Pb. This conversion is characterized by the high α particle emission and by the high energy gamma radiation (2.6 Mev) from ^{208}Tl. The high-energy gamma radiation necessitated special handling considerations for new fuel and for irradiated fuel. Initially, the ^{233}U fuel used for the LWBR contained approximately 6 ppm of ^{232}U. Because of the (n, 2n) reaction, ^{232}U gradually built up during core operation and, at the end of life, the fuel contained approximately 700 ppm ^{232}U.

The thoria-based fuel system is described in Reference 4. This system has many operating advantages over the urania system and some fabrication disadvantages worthy of note. Fabrication difficulties of importance to design included fuel homogeneity, which was difficult to obtain with a single fire process; attainment of full density because of the high melting temperature; and reduced diffusion coefficients at normal sintering temperature. Attainment of design homogeneity was achieved by comicronizing and thoroughly mixing

the binary compositions. High density was achieved by combining the micronized powder with slightly higher than normal sintering temperature.

The operating advantages of the thoria system over the urania system include: (1) higher melting temperature, (2) higher thermal conductivity, (3) lower fission gas release, (4) lower coefficient of thermal expansion, and (5) more corrosion resistance.

At a given linear power output, the margin to melting in LWBR fuel rods (compared to those in commercial reactors) is directly related to thermal conductivity and melting point of the respective fuel systems. Table 6 compares the best estimate melting point of the various unirradiated fuels.

Table 6 - Unirradiated Fuels Best Estimate Melting Point

Fuel System	Melting Point (F)
UO_2	5150
ThO_2	6090
ThO_2 + 2 w/o UO_2	6070
ThO_2 + 4 w/o UO_2	6050
ThO_2 + 6 w/o UO_2	6030

In addition, thermal conductivity of the thoria is higher than urania as shown in Table 7 (the comparison is also on a best estimate basis).

The thoria fuel system also has reduced fission gas release due to the higher threshold temperatures for release from internal dislocations and grain boundaries as shown in References 4 through 6.

Pellet-cladding interaction during power changes is highly dependent on fuel thermal conductivity and thermal expansion coefficient. Table 8 lists typical expansion coefficients for the urania and thoria fuel systems, again illustrating the advantage of thoria.

Table 7 - Unirradiated Fuels Best Estimate Thermal Conductivity

Temperature (F)	UO_2 Fuel (Btu/hr-ft-F)	ThO_2 Fuel (Btu/hr-ft-F)
500	3.4	4.1
1000	2.7	3.2
2000	1.8	2.1
3000	1.4	1.6
4000	1.1	1.2

Table 8 - Unirradiated Fuels Best Estimate Thermal Expansion Coefficients

Temperature (F)	UO_2 Fuel (10^{-6} F)	ThO_2 Fuel (10^{-6} F)
500	4.97	4.75
2000	7.44	5.98
3500	9.06	6.81

The thoria fuel system is inherently more corrosion resistant than the urania systems where UO_2 can oxidize to U_3O_8 when exposed to hot water (defect operation). Conversion of UO_2 to U_3O_8 results in a volume increase potentially overstraining the cladding and can result in a buildup of hydrogen inside the rod. Internal free hydrogen can result in formation of hydride blisters and, ultimately, massive cracks in the cladding. Experiments documented in References 7 and 8 demonstrate the improved corrosion resistance of thoria over that of urania. Additionally, 19 intentionally defected rods were tested in the LWBR irradiation testing program. Four of these defected rod tests experienced some form of waterlogging, but in all 19 tests the fuel itself was very stable with no evidence of corrosion or erosion (References 9 and 10).

General performance of the ThO_2-UO_2 fuel system was supported by an extensive irradiation test program conducted with LWBR reference rods. No fuel or cladding failures occurred because of any attribute unique to the thoria-based system.

4.3 - TIGHT LATTICE (High Metal-to-Water Ratio)

The rod lattice of the LWBR core was extremely tight in order to reduce neutron capture in the water and increase capture in the thorium atoms and thereby enhance the breeding properties of the core. Metal-to-water ratios of the seed, standard blanket, and power flattening blanket regions were 1.72, 3.50, and 1.75, respectively, whereas the typical commercial PWR lattice has a metal-to-water value of 0.82.

The tight lattice requirement of LWBR nuclear design resulted in a rod-to-rod spacing that was only one-half the spacing used in a typical commercial reactor. Likewise, the radial rod-to-support structure spacing in the fuel rod support system (grid) was decreased to about one-half the typical commercial spacing.

These reduced spacings required the use of a hexagonal grid structure (Reference 11) instead of a square grid structure used for commercial grids. This geometry complicated manufacturing by requiring: (1) small precision pieces instead of egg-crate strips, (2) fixtured brazing instead of gas tungsten arc (GTA) welding, and (3) post-braze manual and machine adjustments of individual cell dimples to achieve a properly controlled spacing among rods and to the structure.

Tight tolerances specified for rod spacing acted to improve worst-case rod-to-rod and rod-to-grid spacings, but because these are coupled with rod manufacturing, assembly and operational effects, they could not preclude rods touching rods or rods touching grid panels by end of life in the case of tolerance buildups.

Normal grid manufacturing variations from brazing and heat treatment could significantly reduce the nominal spacing. Minimum rod-to-panel spacings were established (normally six panels of the hexagonal cell) so that there was a statistically small probability of contact. Nonetheless, on a worst-case basis these requirements still permitted potential interferences in blanket and reflector modules.

The radial rod-to-grid spacing was sufficient to accommodate asymmetric curvature of grid cell springs when deflected. This required development of spring repair procedures to improve symmetry in the spring deflection and thereby limit spring intrusion into the adjacent cell. However, adequate clearance to preclude intrusion interference under worst-case conditions was not attainable. As in rod-to-grid spacing, requirements were selected to provide a high expectation of no intrusion interference, but with some small number of potential contacts.

A cladding temperature assessment was performed for rods touching or in proximity (approximately 1 mil) to grids, posts, and connectors. Seed and blanket cladding local temperatures for rods touching grid panels, support posts, and connectors were calculated to be less than or equal to the fuel element steady state and transient limits of 750 and 800F, respectively.

In-pile and out-of-pile tests were performed to assess the impact of rods touching on cladding temperatures and corrosion rates, and the resulting impact on core performance. The S-5 in-pile test had three seed rods on a triangular pitch, with each contacting the other at approximately the same axial location over some small (~0.3-inch) axial distance.

Based on these test results, Zircaloy corrosion rates were determined and used to infer cladding temperatures at contact points. These cladding temperatures were then adjusted to the full range of core operating conditions (i.e., local fluid conditions and heat fluxes) for both seed and blanket geometries based on parameter sensitivities established from out-of-pile

electrically heated rod tests. The out-of-pile tests consisted of three seed rods touching, three blanket rods touching, and two blanket rods touching. The touching rods were banded together over a contact length of approximately 2 inches.

4.4 - LOW-HAFNIUM ZIRCALOY TUBING

Zircaloy-4 ingots used for manufacture of LWBR tubing were limited in hafnium content to a maximum of 50 ppm. This requirement was met by selecting ingots from those available and not by any special ingot fabrication treatment. Thus, mechanical performance equal to standard commercial Zircaloy was expected, while maintaining a low level of parasitic neutron absorption. Ingot requirements for low hafnium Zircaloy-4 material are given in References 12 and 13.

Extensive out-of-pile material property programs were conducted for over 10 years on low hafnium material. Irradiation tests of both low and high hafnium (<50 ppm compared to 50 to 100 ppm) were conducted with no apparent difference in tubing response attributable to hafnium content.

4.5 - NONFREESTANDING BLANKET TUBING

To improve breeding in LWBR, the blanket cladding was made as thin as possible; this resulted in a relatively high compressive hoop stress under external coolant pressure such that it was expected that the cladding would collapse onto the fuel pellets. To provide beginning-of-life strength, the tubing was highly cold worked and stress relief annealed (SRA). Table 9 presents hoop stress for LWBR blanket and commercial reactor fuel elements.

Because of the high hoop stress and relatively high in-pile creep rate of SRA Zircaloy, the blanket tubing must be supported by the fuel pellets. Thus, completely sintered, stable, void-free pellets are required. Some commercial reactors use relatively thinner cladding, but have lower system pressure or prepressurized fuel elements to reduce cladding stresses, as indicated in Table 9.

Table 9 - Typical Cladding Hoop Stress in Pressurized System

Application	Hoop Stress (psi)	System Pressure (psi)
LWBR Standard Blanket	20,600	2000
LWBR Power Flattening Blanket	20,100	2000
CANDU (Canadian Fuel Systems)	16,000	1400
Beaver Valley (Pressurized Rods)	10,400	2250

Creation of an axial gap in the fuel stack would result in loss of cladding support and caused many failures in early commercial reactors. Early in the LWBR program, fuel pellet densification and cladding growth were recognized as contributors to axial gap formation. A design procedure for calculating differential fuel-cladding axial expansion using the CYGRO computer program (Reference 14) was benchmarked to irradiation test data and this procedure was applied to all fuel types to predict the expected axial gap at the top of the fuel stack. The calculated gap was a strong function of fuel burnup and fast neutron fluence. These calculations were used to estimate the gap size which could form between pellets in the stack and which was assumed to be at the worst axial location from the standpoint of cladding collapse. Analyses using the conservative approach indicated that gross collapse of cladding in LWBR fuel rods was highly unlikely for operation to 30,000 EFPH.

Restrictions on fabricated pellet voids (missing fuel chips) were specified to improve grid spring follow capability (spring deflection required to remain in contact with the shrinking cladding throughout lifetime) and to minimize cladding strain. Additional grid spring follow capability required because of voids was 2.2 mils, and cladding strain at maximum voids was 3.4 percent. Thus, nonfreestanding blanket cladding resulted in limits for grid spring follow, one of the most difficult of LWBR design areas.

4.6 - RECRYSTALLIZATION ANNEALED SEED TUBING

Commercial reactors generally use cold-worked tubing with a final stress relief anneal (SRA) treatment, whereas the seed rods of LWBR used highly cold-worked tubing followed by a recrystallization anneal (RXA) treatment. The design approach for the seed rod was to separate the fuel from the cladding (to minimize potential for bowing and fuel-cladding interaction early in life) by using a large fuel-cladding gap (8.5 to 11.5 mils) and to select a cladding thickness to maintain low hoop stress (16,000 psi stress at 2000 psi system pressure). Given these conditions, the cladding heat treatment was then selected to minimize in-pile creep for late-in-life concerns. At 20,000 psi and a fast neutron flux of >5 x 10^{13} neutrons/cm^2-sec, the creep rate of RXA tubing is a factor of 2.6 less than SRA tubing based on creep data from irradiation tests. Screening-type irradiation tests were performed early in the LWBR program in parallel with the selection of seed detailed attributes, including direct comparisons of SRA and RXA tubing. These irradiation tests were then followed by prototype tests. The prototypical irradiation tests had exposures up to 100 x 10^{20} n/cm^2 fluence and 13 x 10^{20} f/cc depletion (62,000 MWD/MTM).

Seed rod performance under power ramp and overpower transient conditions was dependent on the design approach of separating the fuel from the cladding and the use of low-growth RXA cladding with freestanding properties. Overpower transients were limited by cladding yield strength, which is low for RXA tubing at beginning of life but increases with irradiation.

Based on oxide corrosion tests on LWBR tubing (Reference 15), RXA seed tubing has a 25 percent lower corrosion rate than SRA tubing when tested in 680F water.

From the experience gained in the irradiation and corrosion test programs, it was concluded that the use of RXA tubing, at low stress, would result in improved seed fuel rod performance over the use of SRA tubing. Care in initial startup was required, because of the low beginning-of-life yield strength of RXA tubing; therefore, a programmed startup procedure was performed for LWBR.

4.7 - TAPERED FUEL PELLETS

LWBR binary pellets had either tapers (blanket) or chamfers (seed) on the ends of the pellets to decrease chips and voids during manufacture, to improve axial stack movement capability of the fuel in the cladding, and to reduce pellet-cladding interaction (PCI) effects at the ends of the pellets. In general, commercial reactors do not have chamfered/tapered pellets, although some vendors (General Electric Company) are starting in that direction. Reports on commercial fuel rod failures emphasize the high frequency of cladding defects at pellet ends.

The only technical area of concern identified for tapered pellets was associated with grinding tolerances. In general, a taper depth of 2 mils was desired. Manufacturing tolerances were first specified to give a range of 1 to 5 mils. The larger taper depths were found to be limiting with respect to grid spring follow and rod-to-grid proximity. Selective assembly of pellets in the fuel rods was required to limit the taper depth range at grid elevations to 1 to 2.5 mils in the standard blanket and early power flattening blanket rods; specifications for later power flattening blanket fuel blends were changed to confine all pellet taper depths between 1 and 3.8 mils, thus eliminating selective assembly requirements.

A minimum taper of 1.0 mil reduced cladding stress by 2800 psi from that calculated for a square-ended pellet during a reactivity insertion transient and by 3000 psi during a power ramp at end of life. If a maximum sized fuel chip were found to be present at the taper, the advantage of tapers would be compromised. However, tight limits were imposed on the number and location of chips based on radiographic inspections. Thus, on the average, performance was improved with tapered pellets.

As noted above, deep blanket pellet tapers would result in larger grooving of the cladding than shallow tapers, which could adversely affect grid spring follow and rod-to-grid proximities. To compensate for the reduced effective diameter of the rod as cladding grooves into the pellet taper, grid

fixed dimples were adjusted so that the original cell center line was moved away from the panel between the fixed dimples. Thus, if grooving occurred and the rod moved toward that panel, sufficient clearance would be maintained to avoid rod-to-panel proximity violations.

Thus, the unique use of tapered pellets in LWBR to improve fuel element performance put added requirements on the grid support system. This is one of the most critical parts of the design because of the tight lattice spacing, especially in the standard blanket region. Selective assembly of pellets at the grid elevations improved the situation, but even then the calculated loss in spring follow was as high as 4.3 mils at the 95-percent tolerance interval level.

However, all irradiation test information and fuel rod performance analysis demonstrated a significant fuel rod performance gain due to the use of tapers. In fact, calculations showed that extended lifetime would not have been successful if pellet tapers had not been specified.

4.8 - FUEL ZONING FOR CONTROL OF REACTIVITY AND POWER PEAKING

There were many fuel zones in the LWBR core. Each of the 12 binary modules contained a central seed surrounded by a blanket. The seed had two radial binary zones with different enrichments, and the blanket had four radial binary zones composed of three distinct enrichments. The power flattening blanket was composed of rods smaller than those found in the standard blanket region, and had four radial binary zones composed of three distinct enrichments. The fuel densities of the various zones were designed to minimize power peaking adjacent to the water channels between the modules and between the seed and blanket.

The LWBR values in Table 10 are for the limiting seed region at beginning of life. The peaking factor is defined as the ratio of local to average power density for the seed region. The commercial values listed in Table 10 are for the Westinghouse Trojan design; however, they are typical of most commercial core designs. Light Water Breeder Reactor peaking factors were considerably higher due to the necessity of designing a core for the relatively small

Shippingport reactor vessel. Large commercial size LWBR's (~1000 Mw(e)) would have much smaller peaking factors.

Table 10 - Peaking Factors - LWBR Versus Commercial

	LWBR	Commercial
Local Heat Flux	6.3	2.22
Rod Average Power	2.4	1.44

Surrounding the 12 binary modules were the 15 modules that constituted the radial reflector region. These modules were composed of rods initially fueled with thorium oxide. The purpose of the radial reflector was to reduce the neutron leakage by utilizing the otherwise escaping neutrons to increase thorium conversion. Similarly, a 10-inch thoria region was placed at the top and bottom of all binary rods to act as axial reflectors and reduce neutron leakage from the binary region of the core.

Additional axial fuel zoning enhanced the worth of the movable seeds. The outer four rows of seed rods consisted of partial-height binary fuel, with the remainder of each rod composed of unenriched thoria. Similarly, in the standard blanket and power flattening blanket regions, the first four rod rows had partial-height binary fuel and the remainder of the rod was composed of thoria. The thoria in these wedge rod regions of the seed module was loaded preferentially at the top of the outer rod rows to form a sequence of decreasing thoria lengths as the rod row distance from the seed-blanket interface increased. The thoria in the blanket module was loaded preferentially at the bottom of the binary rods, but arranged similarly to the seed module to form a sequence of decreasing thoria lengths as the rod row distance from the seed increased. Hence, relative to the aligned position, where seed and blanket modules were at the same height, the lowering of the seed increased the thoria volume sandwiched between the seed binary and the blanket binary. This increased neutron capture in thoria and decreased neutron capture in the binary regions, which resulted in a decrease in core reactivity. As the seed

was raised, the thoria region between seed and blanket binary was reduced so that fewer captures occurred in the thoria and more in the binary fuel, resulting in an increase in core reactivity. Thus, fuel zoning was used to enhance both reactivity and peak power control. No poisons were built into the core or dissolved in the coolant to achieve this control.

Strict quality control was used during fabrication and inspection to ensure that every pellet in every rod was loaded properly. This was a major effort during the fabrication process and was unique to LWBR.

4.9 - MOVING AND SCRAMMING FUEL

Reactivity control in LWBR was obtained, not by use of poison control rods, but by axial motion of the movable seed modules. Each of the 12 seed modules, containing 619 rods, was designed to move independently, although banked module control was planned for normal operation. A buffer system prevented high contact velocity during module scram.

Extensive scram testing was conducted using both full-scale prototypic (including actual core components such as balance piston, compression sleeve, and buffer cylinder) and preprototypic design hardware covering the core range of operating conditions on module flow, temperature, pressure, movable fuel assembly alignment, and friction. The test results were used to qualify the scram prediction program. Scram results obtained during prototypic testing using core hardware were superior to the core design limits as shown in Table 11.

Hydraulic testing of the balance piston was also conducted to establish the hydraulic sensitivity of the piston-compression sleeve radial clearance and eccentricity. The test data showed that a concentric balance piston had a hydraulic resistance 1.2 times larger than an eccentric piston, and that the smallest radial clearance allowed by design drawings resulted in a resistance 1.6 times larger than that obtained with maximum design clearances.

To provide additional insight into the operability of the movable fuel system, each LWBR movable fuel assembly was instrumented with two timers. One was to detect a module that became inadvertently stuck, and the other was to measure the scram time.

Table 11 - Scram and Contact Velocity

	Bypass Inlet Flow ΔP (psi)	Minimum Terminal Scram Velocity (in/sec)	Test Data Maximum Contact Velocity (in/sec)
	0.0	15.8	6.8
	5.5	15.8	6.8
	21.5	13.0	5.4
	34.5	11.2	2.5
Design		6.0	9.0

It was determined that the LWBR fuel rods would withstand shock loads resulting from scramming of the movable seed modules. Extensive testing and analyses were performed to ensure that integrity of fuel and cladding could be maintained. A flow test module containing 36 seed, blanket, and reflector rods with thoria fuel pellets was intentionally scrammed more than 200 times, while being subjected to the range of coolant temperatures and flow rates expected in LWBR. Radiographic inspection of the rods revealed no significant increase in pellet cracking or chipping due to scramming. The buffer system was designed to limit the maximum contact velocity of the seed modules to 9 in/sec, equivalent to free fall from less than 1/8-inch height. As part of the LWBR test program, 11 irradiated rods, with peak fluence exposures to 33×10^{20} n/cm^2, were intentionally dropped from heights of up to 8 inches without loss of cladding integrity or noticeable damage. A scram shock load assessment and an assessment of the effect on cladding stress of a combined shock load and RIT incident also indicated satisfactory performance.

4.10 - BOLTED TOP- AND BOTTOM-MOUNTED FUEL RODS

In the LWBR support system, fuel rods were firmly attached to either the top or bottom baseplates. In commercial cores, the rods are not fixed, but

are free to move axially in the grids. Fuel rods were attached to baseplates to maintain fuel zone alignment, to minimize grid loads, and to provide space at the top and bottom of the core for flow holes.

In LWBR, about one-half of the rods were attached to the top baseplate, and the other half to the bottom baseplate. The maximum difference within a module was seven rods. This feature significantly reduced loads on grids due to rod growth. The rod growths essentially opposed one another, ideally reducing growth loads on the grid to zero. Based on design analysis, the maximum grid load due to an up-power transient was less than 2000 pounds (hot), whereas sliding of all rods in a grid in the same direction would have resulted in a grid load of about 10,000 pounds. In commercial reactors having about 250 rods per grid, design load would be about 4000 pounds, with grid spring loads equal to those of LWBR. Thus, with fewer rods and a smaller grid, commercial reactors can have grid loads greater than the LWBR design.

Bolting the fuel rods to the top and bottom baseplate did, however, result in additional demands on the fuel rod support system. Nonperpendicularity of the fuel rod and baseplate surfaces and misalignment of the grid cells with the baseplate resulted in some small initial bowing of the fuel rod when the rod was bolted down. For the seed, blanket, and reflector, the additional rod bows which could have occurred were 1.7, 4.3, and 5.0 mils, respectively. This affected rod-to-rod clearances.

In-pile and out-of-pile tests, reported in Reference 16, supported the adequacy of the end stem design for resistance to grid friction loads, flow-induced vibration, and joint loosening due to hydriding. Increased hydrogen pickup could be expected due to nickel contamination at the contact area between the Zircaloy end stem nut and the Inconel baseplate. Extensive testing demonstrated that, for seed and reflector rods, the hydride area on the nut would be localized and that the joint would remain tight. On blanket rods, chromium-plated washers were used to prevent nickel contamination. End-of-life metallographic examination of the seed and reflector rod nuts revealed only the minor localized hydriding that was expected (Reference 17).

4.11 - NEOLUBE IN THE SYSTEM

Neolube is a lubricant applied to the rod surface during installation in the module assembly. It is a colloidal graphite suspension in isopropyl alcohol. The effectiveness of neolube to minimize scratching was demonstrated in numerous in-pile and out-of-pile rod-bundle assemblies (Reference 18). This experience with neolube coatings indicated that LWBR cladding scratches would not exceed a depth of 1 mil in the worst case (and, in general, were significantly lower -- in the range of 0.1 to 0.6 mil). In the commercial industry, Babcock and Wilcox Company procedures require that the springs be held away from the rods during assembly to eliminate scratching; other vendors pull fuel rods in without neolube (or even a corrosion film) for protection.

To support and qualify the use of neolube, tests and analyses were performed which showed neolube was acceptable. Zircaloy specimens coated with neolube indicated long-term corrosion resistance, and hydrogen absorption characteristics of Zircaloy-4 tubing were not altered by neolube. Heat transfer tests demonstrated that there was no change in critical heat flux power level for rods coated with neolube, nor was there any significant change in pressure drop for rod surfaces with or without neolube. Analyses showed that as much as 48 pounds of carbon dispersed in the primary loops during LWBR operation would have no effect on the radiation levels of the plant. It was calculated, using test measurements of the weight of neolube adhering to the fuel rod cladding in a typical assembly application, that in total only about 9 pounds of neolube solids would be introduced by coating all LWBR fuel rods with this lubricant. It was also concluded that the small amounts of gaseous decomposition products (carbon monoxide and methane) would readily be removed from the primary system during normal degasification.

A demonstration test confirmed that graphite suspended in the LWBR coolant would be adequately removed by purification system operation and by deposition on primary system hardware after a short period of hot plant operation. The effect of neolube on the fissile inventory ratio (FIR) would be

negligible (<-0.0001 ΔFIR). In-pile test experience with neolube-coated fuel rods confirmed that no significant problems in the area of corrosion, hydriding, heat transfer, crud deposition and pressure drop were attributable to neolube.

(Intentionally Blank)

SECTION 5 - SPECIFIC FUEL ELEMENT DESIGN CONSIDERATIONS

A background and detailed description of each fuel element design concern is presented in this section. Included are the design criteria, analysis model, and the resulting technical requirements for each category.

5.1 - FUEL PELLET TEMPERATURE

A fuel pellet design criteria was the avoidance of fuel melting and central void formation. Melting temperatures near 6100F were used for this thoria-based fuel system (Reference 4) at beginning of life (BOL). Irradiation effects decreased the melting temperature by 9F per 10^{20} f/cc of fuel depletion. The temperature limit was further decreased by 200F to provide for the effect of pellet circumferential cracking. The resulting temperature limits used for LWBR fuel are listed in Table 12.

Table 12 - Maximum Fuel Temperatures and Design Limits

Fuel Region	Seed	Standard Blanket	Power Flattening Blanket	Reflector
Peak Centerline Temperature (F)				
at Full Power, Normal Rod	3765	2985	3050	1450
at 128% Overpower, Normal Rod	4380	3415	3500	1570
at Full Power, Defected Rod	5100	3650	3785	1920
at 128% Overpower, Defected Rod	5815	4070	4235	2100
Fuel Temperature Limit (F)*	5825 at BOL	5860 at BOL	5855 at BOL	5865 at 18,000 EFPH

*Limit temperature is fuel melting temperature at the lifetime corresponding to peak power, decreased by 200F allowance for circumferential cracks.

Fuel temperatures under operating conditions were computed with the FIGRO program (References 19 through 22). This program was qualified to in-pile measured fuel temperatures in standard benchmark fuel rods used by the Nuclear Regulatory Commission.

Peak centerline temperatures (PCT) were computed for worst-case fuel pellet locations in each of the four fuel regions and compared with design melting temperature for thoria-based fuel. Several operating conditions were used in the temperature calculations. Both normal and defected rods were considered, with the major difference resulting from fuel-cladding gap conductance. The highest temperatures were calculated for a defected rod during a 128-percent overpower transient, an accident condition that is limited by the reactor scram system. Resulting calculated peak centerline temperatures are given in Table 12.

Maximum fuel temperatures were predicted to occur near BOL in the three binary fuel regions and at 18,000 EFPH in the thoria-fueled reflector region. Reduced reactor power after 18,000 EFPH precluded higher temperatures later in life. This timing of maximum temperatures is consistent with the power histories shown in Figure 5. Comparison of the maximum PCT for a potentially defected rod (temperature maximized by the presence of steam in fuel-cladding gap) at peak overpower with the corresponding temperature limit given in Table 12 indicates that the fuel was safe from melting under the most adverse conditions.

Formation of a central void in fuel pellets is caused by pore migration from cold to hot regions of the pellet. This phenomenon is a long-term temperature-driven event that can be avoided by maintaining fuel temperatures below a threshold level defined by the pore migration model of Reference 23. The threshold temperature for central void formation in 18,000 EFPH is 3640F according to this model. If a void does not form by that time, it was calculated that it would not form later at reduced power operation. The 3640F threshold was predicted not to be exceeded during normal long-term operations in the standard blanket, power flattening blanket, or reflector fuel regions. Seed fuel was above 3640F, on a worst-case basis, for the first 1000

hours of operation. This time duration was too short to cause central coring. Therefore, no fuel region was in violation of the central void limitation to 18,000 EFPH and, by extension, to end of life at 29,047 EFPH.

5.2 - AXIAL GAPS

5.2.1 - Design Concern

Two concerns arise from axial gaps forming in the fuel stack of LWBR fuel elements. A major concern is the potential for collapse of cladding into the unsupported axial gap, and a lesser concern is power peaking in adjacent fuel rods which results from the absence of fuel.

5.2.2 - Mechanism for Forming Axial Gap

Two factors which influence the formation of axial gaps in the fuel stack are fuel and cladding length changes. Fuel stack length change occurs because of fuel densification, fission product swelling, hot pressing, and creep caused by loads imposed on the fuel stack by the cladding (pellet-cladding interaction). Cladding length change occurs from irradiation growth, anisotropic mechanical properties of the Zircaloy tubing, fuel-clad interaction effects, and fuel rod-support interaction. Another factor contributing to axial gap formation is the keying of a pellet in position by fuel stack thermal contraction, by pellet end face nonperpendicularity, or by lodged fuel chips.

Several fabrication steps were taken to minimize the formation of axial gaps in LWBR fuel elements. Fuel densification during reactor operation was minimized in LWBR pellets by the high average density (approximately 97.5 percent of theoretical density) and high minimum blend-average density requirements (96.5 percent for a blend of binary fuel and 96 percent for thoria). The fuel was sintered to high densities at 1700 to 1800C for more than 12 hours and, therefore, met all finished product microstructural requirements. Although a single binary pellet can have a density as low as 96 percent, the potential stack shrinkage is a function of the average density of the stack, or the fuel blend density. For the LWBR minimum blend-average density limits, the fuel was essentially stabilized and no significant further in-pile sintering was expected during core operation.

Pellet hot pressing and creep were minimized in LWBR fuel pellets by fuel microstructure requirements for a well-developed grain structure and a minimum number of small, intragranular pores. Stack settling was minimized by fabrication controls and by inspection of in-motion radiographs of each fuel rod to ensure that significant gaps between pellets were not present in as-built rods. Cladding elongation caused by fuel-cladding interaction (axial ratchetting), also an important concern in meeting cladding stress and strain limits, was minimized by design features such as pellet dishes, chamfers, and tapers, by inspections to meet minimum fuel chip requirements, and by specifications limiting the inside surface roughness of the cladding.

5.2.3 - Analytical Model

The size of axial gaps expected to form in LWBR fuel elements throughout their lifetime was calculated with the CYGRO computer program (Reference 14). This program, which includes the primary mechanisms that influence the axial gap, was qualified to perform these calculations by using specific input parameters and the results were then compared to the observed cladding elongation and fuel stack shrinkage of test specimens from the irradiation test program. The input was then adjusted to conservatively predict (calculated values always equal to or greater than observed axial gaps) the magnitudes of the observed axial gaps formed in the irradiation specimens. This conservative model was then used to calculate the sizes of axial gaps expected to form in LWBR fuel elements.

The axial gaps calculated with CYGRO were then analyzed with the ACCEPT program (Reference 24) to determine if the likelihood for cladding collapse existed throughout the lifetime of the LWBR fuel elements. Predicted axial gaps and a description of the ACCEPT program are given in Section 5.14.

5.3 - ROD LENGTH INCREASE

5.3.1 - Design Criteria

The LWBR design criterion with respect to fuel rod elongations was that there be sufficient clearance between the rod free end and the baseplate flow

holes to preclude unacceptable mechanical or hydraulic effects. This required a minimum clearance equivalent to one rod diameter.

5.3.2 - Analytical Model

The CYGRO computer program (Reference 14) was used to calculate length changes of LWBR fuel rods. The CYGRO program includes mechanistic models which influence rod elongation. This program is similar in scope and capability to other fuel rod analysis programs, such as ESCORE (Reference 25) being developed by the Electric Power Research Institute (EPRI). The following components included in CYGRO are the major contributors to in-core fuel rod elongation:

1. Stress-free, irradiation-induced Zircaloy growth which is dependent upon fluence and the metallurgical texture of the cladding.
2. Elongation resulting from diametral shrinkage and anisotropic mechanical properties of the Zircaloy tubing under the influence of system pressure. This contribution to elongation is a function of the metallurgical texture of the tubing and is proportional to the magnitude of the diametral shrinkage.
3. Elongation induced by fuel-cladding interaction effects. This component, once pellet-cladding contact occurs, is a function of the relative strengths of fuel and cladding, and is related to fuel-cladding differential thermal expansion and irradiation-induced fuel volume swelling.
4. Rod-support grid interaction. This component is a function of thermal expansion of the support grid and the fuel rod and friction forces established between the two.

5.3.3 - Qualification of CYGRO Model

A model was developed, using the CYGRO program, by establishing input which resulted in a best fit to dimensional change data from irradiated test samples from the LWBR test program. These samples were built and operated over a range which encompassed that of the fuel elements in the LWBR reactor. After the best fit to the data was established, the input was then

adjusted to give an upper-bound fit (calculated values always equal to or greater than actual values) to the length change data.

5.3.4 - Design Calculations

The upper-bound parameters were then used to calculate the elongation of the LWBR fuel elements. Table 13 gives the calculated elongations for the most limiting fuel rod from the seed and standard blanket regions, and also the net clearance between the rod free end and the baseplate at 18,000 EFPH.

Table 13 - Calculated Elongations of LWBR Fuel Elements (at 18,000 EFPH)

	Seed (in.)	Standard Blanket (in.)
Initial As-Fabricated Clearance Between Free End and Baseplate	1.81	2.93
Module Shell Growth	0.33	0.22
Calculated Rod Elongation	1.50	1.24
Net Clearance*	0.64	1.91
Required Clearance (Rod Diameter)	0.31	0.57

*Net Clearance = Initial Clearance + Shell Growth - Rod Elongation.

For all regions, the calculated clearance was greater than one rod diameter. Therefore, rod elongation through 18,000 EFPH was not expected to impede coolant flow at the baseplate holes.

5.4 - STRESS CORROSION CRACKING

Stress corrosion cracking (SCC) was recognized by fuel rod designers in the mid 1970's as a significant cladding defect mechanism. Test rods were failing with hairline cracks at cladding stress levels far below the ultimate strength of Zircaloy. This type of cladding failure was distinct from the familiar cladding ductile rupture caused by stresses beyond yield strength. The

separate failure mechanisms and the power operations causing each type of failure were described in Reference 26. Hairline cracks were apparently caused by SCC, which could occur during normal power ramping. Mechanical rupture was attributed to overpower ramps which stressed the cladding beyond yield. In the LWBR irradiation test program, two cladding defects occurred during planned power ramps. Both were hairline cracks attributed to the SCC mechanism.

Stress corrosion cracking was shown in laboratory tests on unfueled tubing specimens (References 27 and 28 for LWBR seed and blanket tubing, respectively) to occur at stress levels as low as 20,000 psi in the presence of controlled amounts of iodine gas at typical fuel rod operating temperatures. These stress levels were lower than the 40,000 to 60,000 psi yield strength of irradiated Zircaloy. Stress levels of 20,000 to 30,000 psi could be attained in the cladding of LWBR fuel rods during normal power ramping under certain conditions and, therefore, could lead to SCC defects if sufficient corrosive products were formed from the fissioning process.

In the LWBR development program, tests on unfueled tubing included the corrosive elements iodine and cesium in separate specimens and in combination. Iodine emerged as the more likely reactant to cause SCC. This confirmed the results of earlier tests by Weinberg (Reference 29) and Rosenbaum (Reference 30) that iodine vapor was capable of causing through-wall cracks in stressed Zircaloy tubing.

Iodine isotopes are generated in the fissioning process in thoria-based fuel. As demonstrated in Reference 31, a small fraction of iodine is released to the fuel-cladding gap during power operations. Fractional release of iodine is considered equal to the release fraction of the dominant fission gases, xenon and krypton. Measured amounts of iodine release in LWBR irradiation test rods are correlated in Reference 32 with a prediction formula based on fuel depletion, fission gas release, and the fissile isotope (either ^{233}U or ^{235}U).

A fracture mechanics model for predicting crack propagation in Zircaloy cladding was reported in Reference 33. Pressurized tube data from Bettis and

EPRI reports, using unirradiated and irradiated tubing samples, provided the qualifying basis for the model for analysis of SCC defects occurring within 100 hours of a power ramp.

Test data in References 27 and 28 indicate that a threshold stress level exists, below which SCC will not occur for any time duration of exposure. It is this concept of a threshold stress level that was used in the performance evaluation of LWBR fuel rods and in subsequent power operation guidelines.

Threshold stress for the onset of SCC was shown to vary with cladding texture (resulting from RXA or SRA fabrication), cladding temperature at the inside surface during power operation, and the iodine concentration available at the inside surface. The threshold stress levels for LWBR fuel rod analysis were derived from cladding stress analyses of both defected and nondefected fuel rods using the CYGRO computer program (Reference 14). Reported data from irradiation tests conducted by Bettis and by international projects such as for the OVER-RAMP project at Studsvik (Reference 34) were used to determine the threshold stress below which cladding defects did not occur. Calculated stress levels for the irradiation test rods were adjusted to account for temperature and iodine concentration and to obtain separate threshold stress levels for RXA and SRA cladding.

The following correlations were used to calculate threshold stress as a function of temperature and iodine concentration in accordance with the pressurized tube test results:

$$\sigma_{th}(\text{RXA}) = 26{,}310\ (I/0.28)^{-0.19525}(1572.8 - 1.059T)/805$$

$$\sigma_{th}(\text{SRA}) = 30{,}000\ (I/0.29)^{-0.1875}(2710 - 3T)/535\ ,$$

where:

σ_{th} = threshold stress for onset of SCC (psi)
I = iodine concentration (mg/dm^2)
T = cladding inside surface temperature (F).

Typical values for RXA cladding were 725F, 0.28 mg/dm^2 iodine concentration, and 26,310 psi threshold stress. For SRA cladding at 725F and 0.29 mg/dm^2, the threshold stress was 30,000 psi.

To account for variability in cladding inside surface conditions and to provide a conservative design basis, a factor of 0.57 was applied to these threshold levels based on observed surface flaws on LWBR production tubing. The EPRI approach to surface condition variability, reported in Reference 35, was that such variation is caused by higher than average concentrations of alloying elements or impurities. In either the Bettis or EPRI approach, the observed effect of material variability was accounted for in the threshold stress correlations.

Calculated cladding stress was used for predicting SCC defect occurrence and for assessing the LWBR fuel rod power ramping capability. Cladding stress levels at the peak of a power ramp were compared with the specified SCC stress limits. The peak cladding stress levels were computed in two phases. First, the uniform stress was computed using the CYGRO program with fuel element parameters and CYGRO representations that resulted in worst-case cladding stress levels. To those uniform stress levels were added any local stress concentrations that were not included as allowances in the generation of stress limits.

The CYGRO model used to compute cladding stress was a modification of the model which best represented rod dimensional changes measured in irradiation test rods. To ensure that worst-case stress levels were being computed, the model was modified in the areas of fuel densification, Zircaloy creep properties, and fuel swelling rates. All modifications were in the direction that resulted in increased cladding stress. The modified model was used to compute maximum uniform cladding stress at postulated power ramps from a range of steady state power levels throughout lifetime. To these uniform cladding stresses were added a local stress concentration caused by lodged fuel chips. The effect of chips on cladding stress is formulated in Reference 36. Local effects of such items as radial pellet cracks, pellet hourglassing

causing cladding ridges, and cladding thickness variations were considered to be included in the SCC threshold stress since it was based on irradiation test rod experience.

Each fuel region was represented in this power ramping evaluation by the highest duty fuel rod in the region. The analysis was focused on two worst-case rods, one seed and one standard blanket, after it was demonstrated that margins between peak cladding stress and the SCC threshold stress were less for the standard blanket rod than for the representative rods from the power flattening blanket and reflector regions.

High cladding stresses were prevented in LWBR with control of plant operations to avoid those power histories which would lead to stress levels above the SCC threshold stress. Such control was administered through a parameter called the lifetime equivalency parameter (LEP). The LEP value is a calculated equivalent constant power level which would result in maximum power ramp cladding stresses equal to those resulting from the same power ramp following the actual time-varying power history. It is a measure of the power level to which the cladding has become conditioned over recent long-term operations. A power ramp from any temporary power level to full power will result in no higher stresses than a ramp from the conditioned power level, or LEP, to full power. A method was devised for the plant operator to calculate the moving LEP daily from the power history. This was supported by monthly calculations of LEP based on computed cladding stresses in the worst-case fuel rods. Plots of the LEP values throughout lifetime are shown in Figure 10.

Also shown in Figure 10 is the minimum allowable LEP for unrestricted operation to full power. This curve is labeled DLEP, for delimiting lifetime equivalency parameter. The shape of the DLEP curve is discussed in Reference 3. If the LEP were to decrease to the DLEP or lower, then a ramp to full power would result in cladding stresses above the SCC threshold stress. In that event, power ramping restrictions would be imposed until the LEP could be raised above the DLEP, thus conditioning the cladding to again be capable of withstanding power ramps to full power. For efficient plant utilization, it was prudent to maintain the LEP above the DLEP and thus preserve full power

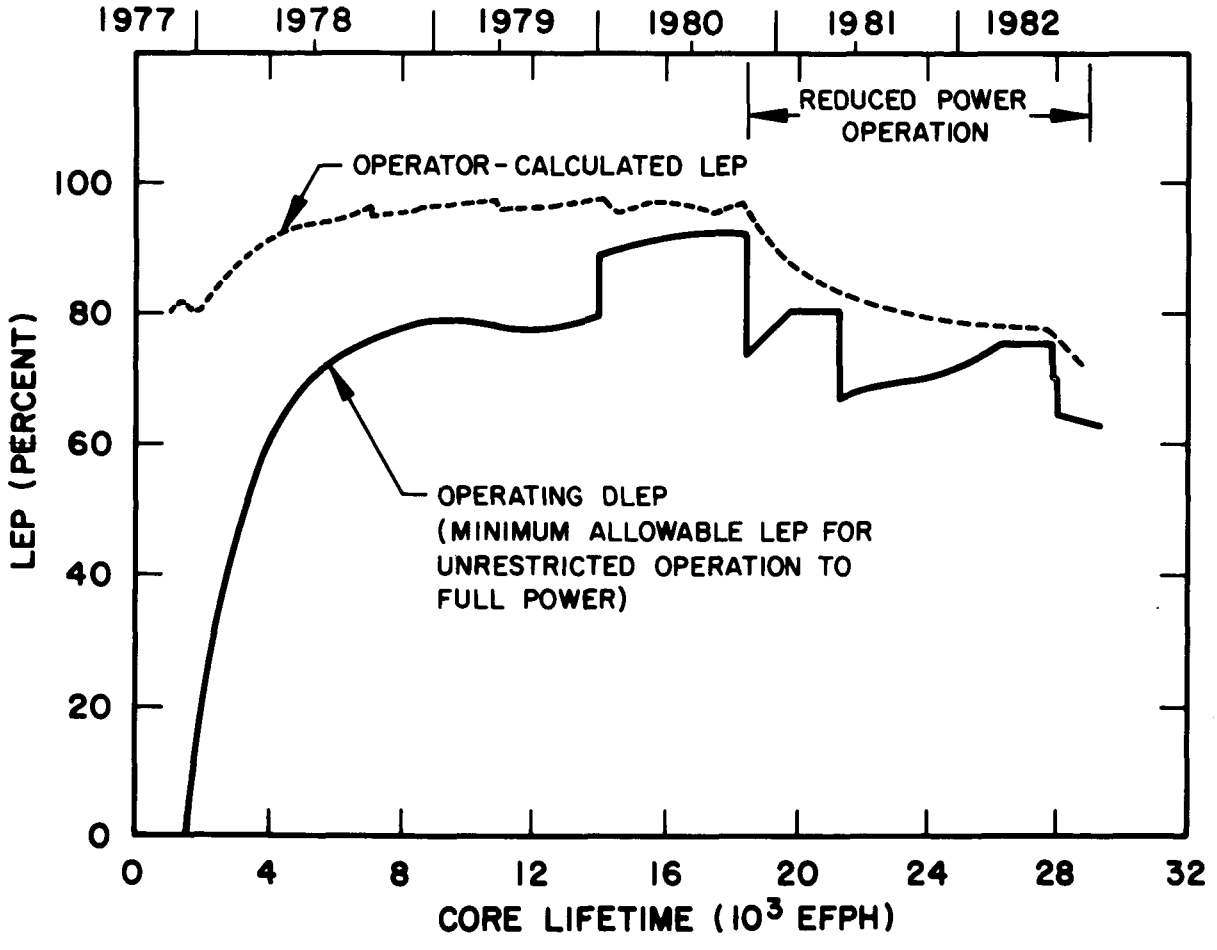

Figure 10. Lifetime Equivalency Parameter Versus Lifetime

capability at all times. As shown in Figure 10, this was accomplished throughout LWBR lifetime, allowing for the reduction of maximum allowable power to 80 percent of rated power after 18,000 EFPH.

In summary, the major corrosive agent recognized in the LWBR method for assessing the effects of SCC is iodine. The exclusive use of iodine concentrations in the LWBR assessment procedure provided a conservative and predictable basis for evaluation of SCC susceptibility in both irradiation test rods and in LWBR fuel rods. The effect of cladding interior surface conditions was included in the conservatism of design assessments. Cladding stress was used for predicting iodine-induced failures and for assessing the LWBR fuel rod ramping capability. The resulting procedure for maintaining cladding integrity against SCC was similar to methods employed in CANDU reactors (Reference 26) and others promoted by EPRI (Reference 37).

5.5 - OVERPOWER TRANSIENTS

Overpower transients are power ramps to levels above full rated power. They are short-lived transient conditions, usually terminated within minutes by the scram system. From a fuel rod standpoint, cladding integrity is jeopardized during fast transients only if the Zircaloy tensile strength is exceeded. The lower stress corrosion cracking (SCC) stress limits are actually time-dependent, decreasing from the material tensile strength at short time durations (minutes) to the threshold level described in Section 5.4 at approximately 100 hour and longer durations. Among the many postulated accident conditions causing overpower transients, the module withdrawal accident causing a reactivity insertion transient to 128 percent power is the most severe on fuel rods.

A cladding failure resulting from an overpower transient usually has the characteristics of a ductile rupture caused by plastic instability (Reference 38). Defects can be avoided, however, by assuring that cladding stresses do not exceed specified limits, with a method similar to that of avoiding SCC threshold stress in normal power ramping. In fact, a CYGRO calculation of cladding stresses in a simulated overpower transient showed that the protection system devised to prevent cladding defects from SCC during normal power

ramps is sufficient to prevent defects from cladding overload during overpower transients to 128 percent power.

Cladding stress limits indicative of the onset of plastic instability were derived from uniaxial tensile test data. Typical yield stress curves are shown in References 39 and 40. To apply the reference stress limits to fuel element cladding under irradiation conditions, further adjustments were made for:

1. Thermal annealing during core operation, which reduced the irradiation hardening of the cladding (this adjustment tends to level off the rising stress limits at the higher fluence levels),
2. Strain rate sensitivity, which reduced the reference stress limits for cladding strain rates less than the strain rate of the tensile tests, and
3. An engineering design factor incorporating uncertainties in the above two effects and in the basic tensile test data.

The reference stress level, adjusted by these three factors, was then the plastic instability stress limit to which computed cladding stresses for overpower transients were compared (to determine the potential for loss of fuel rod integrity).

The cladding stress used in this analysis was a generalized stress as defined in Reference 41 and calculated by the CYGRO program. The generalized stress combines the principal stresses from the biaxial stress system of a cylindrical fuel rod into a single stress level directly comparable to the stress limit curves derived from uniaxial stress data. In addition to the uniform generalized stress calculated at the peak of simulated overpower transients, local stress concentrations are determined to provide conservative margin to stress limits. Calculated uniform stress is thus increased for the local effects of: (1) pellet hourglassing causing cladding ridging, (2) pellet radial cracking increasing circumferential strain on the cladding, (3) fuel chips lodged in the fuel-cladding gap causing local stress concentrations, and (4) local cladding thin spots. This last effect includes fabricated nonuniformities, surface scratch marks, loss of wall thickness to

corrosion and formation of a hydride rim, and wear marks caused by contact with the grid support system.

From a parameter study of peak cladding stresses at 128 percent power following cladding conditioning at various power levels, an LEP-DLEP system was derived for overpower transients similar to the system described in Section 5.4 for normal power ramps. Comparison of this system to the system protecting LWBR fuel rods against SCC during normal power ramps showed that the SCC system adequately protected rods against plastic instability during overpower transients limited to 128 percent peak power by the reactor scram system. Therefore, the SCC system was used to govern reactor operations throughout the core lifetime.

5.6 - CLADDING CORROSION AND HYDRIDING

5.6.1 - Design Concern

Design concerns for the corrosion and hydriding of nondefected LWBR fuel rods were: (1) decrease in effective cladding metal thickness due to the formation of an oxide film and/or a solid hydride rim, and (2) decrease in cladding ductility due to a uniformly distributed concentration of hydride phase. Massive hydriding was precluded in a nondefected fuel rod because fuel was out-gassed after fabrication to remove moisture, and hydrogen ingress was limited to prefilmed external surfaces of the rod (Reference 42).

5.6.2 - Analysis

Limits were established on the amount of LWBR fuel rod cladding corrosion and hydriding permissible to avoid excessive material loss and weakening of fuel element cladding and endclosure welds. The corrosion weight gain and oxide thickness on the Zircaloy was calculated using an analysis procedure qualified to LWBR irradiation test rods and out-of-pile tubing tests, a Shippingport PWR long-life test (MELBA*), and several commercial reactor fuel rods (References 15, 43, and 44). Examination of the qualification data base,

*Multipurpose extended life blanket assembly.

summarized in Table 14, shows that it extends beyond 30,000 EFPH for RXA Zircaloy. The SRA data base has shorter exposures (≤20,424 EFPH), but conservative extrapolations were made using the analysis procedure.

5.6.3 - Corrosion Model

The water corrosion tests revealed differences in the corrosion product weight gains and oxide thicknesses between RXA and SRA Zircaloy. The SRA Zircaloy corroded faster than RXA material. A computer program, designated CHORT (Corrosion and Hydriding of Reactor Tubing), was developed from LWBR test data (References 15, 43, and 44). The model attributes the observed difference in corrosion behavior of RXA and SRA Zircaloy to a difference in the periodicity of a cyclic transition of the oxide corrosion film. Adding a neutron flux correction term to the weight gain correlation accounted for the slightly enhanced corrosion observed during in-reactor testing. The in-pile corrosion model agreed with measured data when the enhancement factor was kept linearly proportional to the fast neutron flux (>1 Mev).

5.6.4 - The CHORT Program Calculations

Calculations using CHORT for each of the four LWBR rod types were performed for irradiation histories of 18,000 and 30,000 EFPH. The assumptions were as follows:

1. Nucleate boiling occurred throughout life (constant temperature of 645F at the metal-oxide interface).
2. The total EFPH was equal to the total hot water hours.
3. An average neutron flux was used throughout life such that integration gives a total peak fluence.

These were conservatively established assumptions since longer exposure time at lower temperature results in less oxide corrosion; i.e., corrosion rate is exponential with temperature but linear with time.

For exposure after 25,000 EFPH, the assumptions were as follows:

1. The power level was a constant 50 percent of full power. Temperature is reduced to 600F at the metal-oxide interface.

Table 14 - CHORT Qualification Data Base

Test/Reactor	Zircaloy Characteristics: Composition	Zircaloy Characteristics: Type	Coolant Chemistry	Number of Specimens	Cladding Temperature (F)	Exposure: Total (hr >400F)	Exposure: Maximum (EFPH)	Exposure: Fluence (10^{20} n/cm^2)
LWBR Autoclave	Zircaloy-4	SRA	H_2O	62	680	10,824	--	--
		RXA	H_2O	152	680	10,824	--	--
LWBR Irradiation Test Program	Zircaloy-4	SRA	NH_4OH	18	581 to 654	--	18,744	86.1
	Zircaloy-4	RXA	NH_4OH	28	551 to 629	--	19,970	101.0
MELBA	Zircaloy-2	RXA	LiOH and NH_4OH	3	516 to 553	108,576	51,139	82.3
Main Yankee	Zircaloy-4	SRA	LiOH	≥1	550 to 600	12,744	11,820	29.4
KWO	Zircaloy-4	SRA	LiOH	≥1	633	--	12,288	44.2
Turkey Point	Zircaloy-4	SRA	LiOH	5	637 to 640	--	20,424	56.0

2. The incremental EFPH was one-half the total hot water hours.
3. The CYGRO calculated flux for 50-percent power was used for each rod type.

The power history assumed for these calculations conservatively represented the actual power history of 100 percent to 18,000 EFPH followed by 80 percent to 27,400 EFPH and a gradual reduction to 57 percent at end of life.

A summary of the CHORT input package is included in Table 15. The results of the CHORT analyses at 18,000 and 30,000 EFPH for corrosion oxide thickness are presented in Table 16, while the hydrogen pickup data are listed in Table 17. Best estimate values multiplied by a 1.5 variability factor were used for the design values. This factor was based on in-pile test data (Reference 43) and accounts for material variability and in-pile test uncertainties (radiation histories, time at temperatures, cladding temperatures, fast neutron fluxes, and oxide film thickness measurements on irradiated samples).

5.6.5 - Discussion of Results

The data of Table 16 shows that the total loss of Zircaloy cladding at the peak power position for all LWBR rod types due to oxidative corrosion is ≤1 mil at 30,000 EFPH. This metal loss is accounted for in the CYGRO stress analysis. The maximum calculated local cladding hydrogen contents at 30,000 EFPH are about 540 ppm and 440 ppm for seed and blanket rods, respectively. (Up to 455 ppm of hydrogen was measured in Shippingport MELBA rods after ~51,000 EFPH exposure (References 45 and 46).)

Test results are available which show that 500 to 1000 ppm of hydrogen in irradiated Zircaloy does not significantly degrade operating temperature mechanical properties, provided the hydride orientation is not predominantly radial (References 47 and 48). The methods for manufacturing LWBR cladding resulted in textures which gave a high degree of hydride orientation in the circumferential direction. In addition, detailed examinations of LWBR seed and blanket irradiated cladding specimens confirmed that the hydride platelets were circumferentially oriented. Thus, the calculated hydrogen content of LWBR fuel rod cladding was predicted to have no significant detrimental effect on cladding behavior.

Table 15 - Input Data for CHORT Analysis of Nondefected LWBR Core Rods

Rod Type	Temperature (F)	Time at Temperature (hr)	Average Neutron Flux (10^{14} n/cm^2-sec)	Cladding Condition
		A. CONDITIONS TO 25,000 EFPH		
Seed	645	25,000	1.14	RXA
Standard Blanket	645	25,000	0.89	SRA
Power-Flattening Blanket	645	25,000	0.75	SRA
Reflector	645	25,000	0.39	SRA
		B. CONDITIONS FROM 25,000 TO 30,000 EFPH		
Seed	600	10,000	0.67	RXA
Standard Blanket	600	10,000	0.445	SRA
Power-Flattening Blanket	600	10,000	0.375	SRA
Reflector	600	10,000	0.195	SRA

Table 16 - CHORT-Calculated Corrosion Oxide Thickness for Nondefected LWBR Core Rods at Peak Power Position

Rod Type	Oxide Thickness (mils)		Equivalent Metal Loss (mils)*	
	Best Estimate	Design†	Best Estimate	Design†
		18,000 EFPH		
Seed	0.66	0.99	0.40	0.60
Standard Blanket	0.68	1.02	0.41	0.61
Power Flattening Blanket	0.64	0.96	0.38	0.57
Reflector	0.52	0.78	0.31	0.47
		30,000 EFPH		
Seed	1.08	1.62	0.65	0.97
Standard Blanket	1.10	1.65	0.66	0.99
Power Flattening Blanket	1.03	1.55	0.62	0.93
Reflector	0.86	1.29	0.52	0.78

*Equivalent metal loss is 0.6 times the oxide thickness.
†Design value is 1.5 times the best estimate.

Table 17 - CHORT-Calculated Hydrogen Pickup in Nondefected LWBR Core Rods at Peak Power Position

Rod Type	CHORT-Calculated Hydrogen Pickup (ppm)*			
	18,000 EFPH		30,000 EFPH	
	Best Estimate	Design†	Best Estimate	Design†
Seed	224	336	345	518
Standard Blanket	185	278	277	416
Power Flattening Blanket	189	284	275	413
Reflector	101	152	144	216

*To obtain total hydrogen content, add 20 ppm which represents the maximum hydrogen level in the purchased tubing.
†Design value is 1.5 times the best estimate.

5.7 - ROD BOW

5.7.1 - Design Concern

Fuel rod bow can affect rod-to-rod spacing. If two adjacent rods deflect to within a few thousandths of an inch of each other, coolant flow is restricted and local hot spots may develop.

5.7.2 - Analysis

The ROBOT and CYGRO computer programs (References 49 and 14) were used to evaluate bowing of LWBR fuel rods. The CYGRO program was used to determine changes in fuel rod geometry and stresses during core life due to changing thermal and neutron environments. The ROBOT program was used to determine the in-reactor fuel rod bow.

General input for the ROBOT program included the following:

1. Cladding and pellet stress states (based on CYGRO calculations).
2. Cladding and pellet material properties.
3. In-reactor environment conditions including power and fast flux gradients.
4. Cladding and pellet diameters (based on CYGRO calculations).
5. Support grid axial locations and reaction point flexibilities.
6. Time varying grid-induced axial compressive load (thrust).
7. Fuel stack bending stiffness efficiency.
8. Fuel crack healing efficiency.

Fuel stack bending stiffness efficiency accounts for interaction between the cladding and fuel pellets. It is a measure of the fraction of fuel pellet stiffness that contributes to overall rod stiffness. Efficiency coefficients ranged from 0.3 for partial pellet-cladding interaction (due to cladding ovaling in blanket and reflector) to 0.8 for full circumferential pellet-cladding contact.

Fuel pellets were modeled in CYGRO as a series of concentric rings. Fuel crack healing efficiency accounted for cracking and healing (closure of a fuel crack) of fuel pellet rings. In ROBOT, transverse cracking of a ring caused

the ring element to lose its bending stiffness and thereby affect rod bow. Other items in the above list are self-explanatory.

Four major sources of fuel rod bow were considered in LWBR blanket and reflector fuel rod bow calculations: (1) rod initial nonstraightness, (2) grid misalignment, (3) flux gradient, and (4) endconnector tightening torque.

Five sources of fuel rod bow were considered for LWBR seed fuel rods: (1) rod initial bow, (2) grid nonperpendicularity, (3) flux gradient, (4) cladding thickness eccentricity, and (5) endconnector tightening torque. Bow of individual rods was determined by using ROBOT to calculate the contribution for each bow contributor in combination with axial thrust.

Table 18 shows the initial rod bows used for LWBR fuel rod analyses. Initial rod bow was assumed to be sinusoidal. In-bundle bow of each LWBR fuel rod was calculated from free-hanging bow measurements to ensure that the calculated bow did not exceed these values.

Table 18 - Initial Fuel Rod Bows

Rod Type	Bow (mils) at Span No.							
	1	2	3	4	5	6	7	8
Seed	9.5	9.5	6.0	6.0	6.0	6.0	9.5	9.5
Standard Blanket	3.5	4.5	4.5	5.7	4.5	4.5	3.5	--
Power Flattening Blanket	5.5	6.0	6.0	7.0	6.0	6.0	5.5	--
Reflector	10.1	6.9	4.8	4.8	6.9	10.1	--	--

Grid misalignment bow accounted for the bow due to misalignment of cells in adjacent grids. Grid misalignment bow was not considered in seed fuel rod bow calculations because the dual dimple arrangement essentially fixed the ends of the rod in each span.

Gradient bow accounts for the bow due to power and fast flux gradients across the fuel rods.

Endconnector tightening-induced bow accounted for bow which resulted from moments imposed from fuel rod endconnector to baseplate seating surface misalignments (nonperpendicularity) and bow due to lateral loads applied to the endconnector during the nut-tightening operation. Bow due to nut tightening was assumed to exist in the two end spans. Initial bow values due to nut torquing used in ROBOT calculations are tabulated in Table 19.

Table 19 - Initial Bow Due to Endconnector Tightening

Rod Type	Bow (mils) at Span No. 1	Bow (mils) at Span No. 2
Seed	15.5	3.9
Blanket	9.9	2.3
Reflector	12.0	3.0

Grid nonperpendicularity bow accounted for the bow which was introduced by offset of the upper and lower dimple pairs in seed grids. Manufacturing allowances permitted grid cell nonperpendicularities of up to 3 mils/in. An arrangement in which grid nonperpendicularity alternated sign between adjacent grids was conservatively assumed in rod bow calculations.

Cladding thickness eccentricity-induced bow accounted for bow which resulted from the uneven stress distribution around the cladding circumference due to varying circumferential wall thickness. This uneven stress distribution could have a significant effect on the bow of seed fuel rods with freestanding cladding. However, tight limits were imposed on wall thickness eccentricity of the purchased tubing used as LWBR fuel cladding. Cladding eccentricity did not affect bow of blanket and reflector fuel rods with nonfreestanding cladding where axial loads were shared by the cladding and fuel pellets.

The procedure for calculating bow in LWBR fuel rods was qualified by comparison with data from LWBR irradiation tests. Input to provide best estimate predictions of observed fuel rod bow was defined. Margin for design calculations was obtained by using bow error allowances to bound all measured irradiation test rod bows.

Table 20 presents calculated bows for each of the bow components discussed above for LWBR seed, standard blanket, and reflector fuel rods after operation to 18,000 EFPH.

Adequate thermal performance of LWBR fuel rods was assured by limiting the minimum clearance between fuel rods in the high power regions to the values given in Table 21. Beginning at 14,000 EFPH, however, in anticipation of extending core lifetime, rod bow was assumed to result in rod-to-rod contact at worst-case locations. A probabilistic analysis was used and design performance allowances were made to accommodate rod-to-rod contact as described in Reference 3.

Rod-to-rod clearance reductions due to rod dimensional changes (diameter shrinkage, cladding wear, etc.) as well as clearance reductions due to bow were considered in determining minimum rod-to-rod spacing.

5.8 - FISSION GAS RELEASE AND LOSS-OF-COOLANT ACCIDENT PERFORMANCE

5.8.1 - Design Concern

Fission gas release from the fuel was required to remain below levels which would result in the following:

1. Fuel rod internal pressure exceeding the system pressure.
2. Unacceptable cladding diameter expansion during a postulated worst-case LOCA.
3. Unacceptable increase in fuel pellet peak central temperature.

5.8.2 - Discussion

The analysis procedures used to calculate the amount of fission gas released from LWBR fuel are reported in References 6, 50, and 51. The

Table 20 - Bow Components by Rod Type (18,000 EFPH)

Seed Fuel Rod Bow Components

Bow Contribution Due to	Bow (mils) at Grid Span No. 1 or 8	2 or 7	3 or 6	4 or 5
Initial Bow	10.6	11.3	7.3	7.0
Grid Nonperpendicularity	11.6	10.7	16.6	16.5
Gradient Bow	1.1	0.5	0.3	0.9
Endconnector Tightening	16.4	4.9	--	--
Clad Eccentricity	2.3	1.8	4.6	3.0
Bow Error Allowance	4.0	4.0	4.0	4.0
Total	46.0	33.2	32.8	31.4

Blanket Fuel Rod Bow Components

Bow Contribution Due to	Bow (mils) at Grid Span No. 1 or 7	2 or 6	3 or 5	4
Initial Bow	5.0	6.3	6.0	7.0
Grid Misalignment	0.5	0.8	0.8	0.4
Gradient Bow	1.7	2.3	2.9	2.9
Endconnector Tightening	14.4	3.2	--	--
Bow Error Allowance	12.0	12.0	12.0	12.0
Total	33.6	24.6	21.7	22.3

Reflector Fuel Rod Bow Components

Bow Contribution Due to	Bow (mils) at Grid Span No. 1 or 5	2 or 4	3
Initial Bow	11.1	14.3	16.6
Grid Misalignment	5.1	6.9	4.8
Gradient Bow	3.0	3.0	4.0
Endconnector Tightening	26.0	5.0	--
Bow Error Allowance*	--	--	--
Total	45.2	29.2	25.4

*A bow error allowance was not included for reflector fuel rods because of the unavailability of irradiation test data.

Table 21 - Fuel Rod Spacing Limits

Region	Minimum Allowable Rod-to-Rod Spacing (mils)
Seed	9
Standard Blanket	11
Power Flattening Blanket	11
Reflector (high power)	17
(low power)	9

calculated fission gas release values (as a percent of gas generated in the fissioning process) as a function of lifetime for the highest depleted rods in each of the four fuel regions of LWBR are shown in Figures 11 and 12 for best estimate and conservative design procedures, respectively.

Knowledge of the plenum gas and its constituents is of utmost importance in demonstrating fuel rod adequacy during a postulated loss-of-coolant accident (LOCA). Plenum gas is considered to consist of four contributions: (1) initial helium atmosphere, (2) volatile gases released from fuel, (3) fission gases released from fuel, and (4) helium produced by a ternary fission mechanism. The volatiles and fission gases are poor heat conductors in comparison to the original helium fill gas. As lifetime increases, this leads to higher fuel temperatures and increased stored energy in the fuel rod. These factors contribute to higher cladding temperatures during the LOCA transient. The released gases also increase the internal rod pressure, which may couple with the high cladding temperature experienced during the LOCA to balloon the cladding and restrict coolant channels. The calculated gas produced in the most limiting fuel rod in each of the four LWBR core regions through 32,300 EFPH is given in Table 22.

The calculated total gas produced in the fuel rod was used to perform additional calculations of the internal pressure generated within the rod

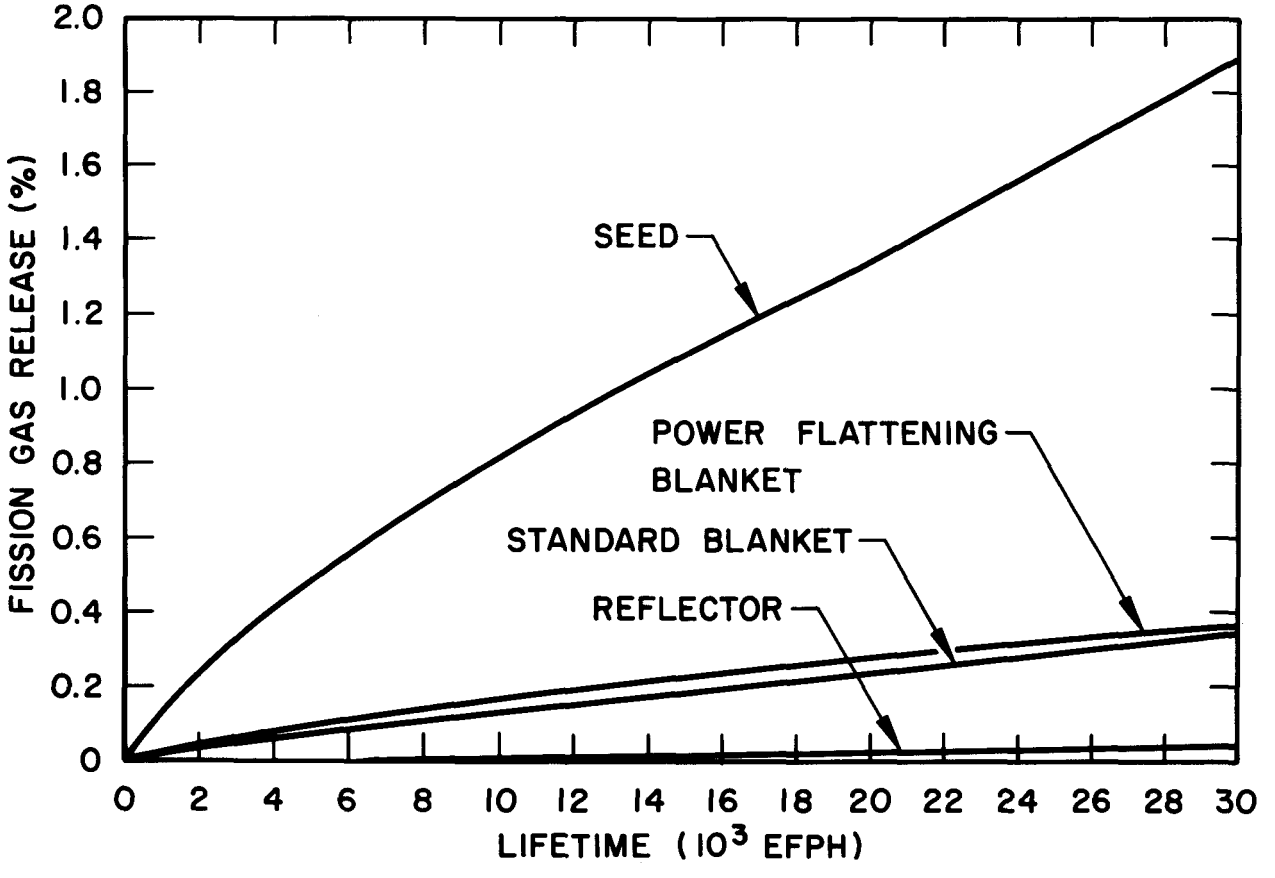

Figure 11. Best Estimate Fission Gas Release

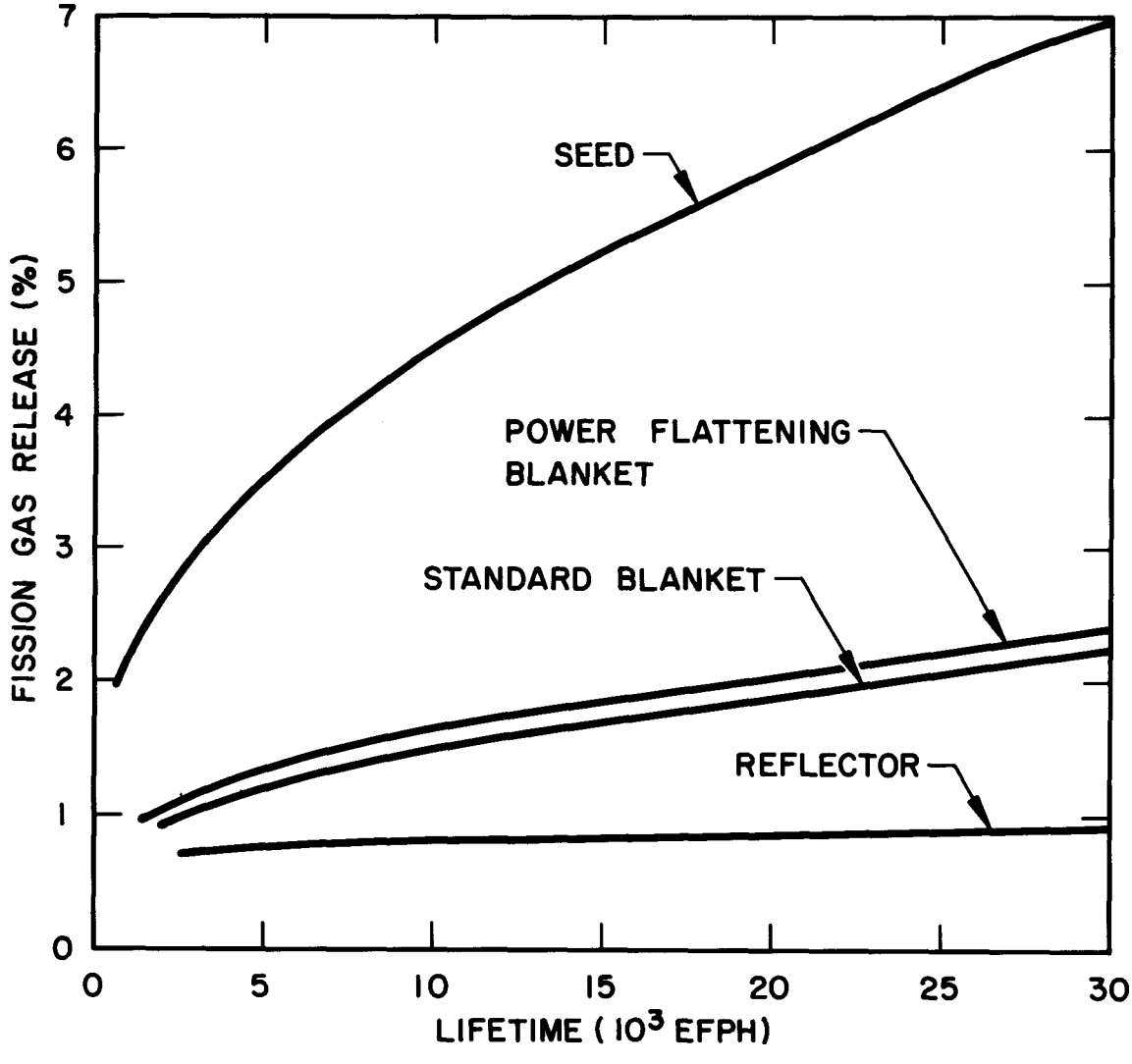

Figure 12. Design Fission Gas Release Over Lifetime

Table 22 - LWBR Fuel Rod Internal Gas Composition

Rod Type	Time (EFPH)	Calculated Gas Composition (10^{-3} moles) Initial He	Volatiles	Fission Gas	Ternary He	Total
Seed	0	0.616	0.082	0.0	0.0	0.698
	2,500	0.616	0.082	0.117	0.024	0.839
	5,000	0.616	0.082	0.288	0.046	1.032
	10,000	0.616	0.082	0.677	0.085	1.460
	15,000	0.616	0.082	1.112	0.122	1.932
	18,000	0.616	0.082	1.412	0.144	2.254
	25,300	0.616	0.082	2.008	0.192	2.898
	27,500	0.616	0.082	2.233	0.205	3.136
	32,300	0.616	0.082	2.708	0.233	3.639
Standard Blanket	0	1.441	0.335	0.0	0.0	1.776
	2,500	1.441	0.335	0.072	0.038	1.886
	5,000	1.441	0.335	0.171	0.077	2.024
	10,000	1.441	0.335	0.399	0.149	2.324
	15,000	1.441	0.335	0.679	0.223	2.678
	18,000	1.441	0.335	0.869	0.265	2.910
	25,300	1.441	0.335	1.233	0.365	3.374
	27,500	1.441	0.335	1.394	0.393	3.563
	32,300	1.441	0.335	1.729	0.456	3.961
Power Flattening Blanket	0	1.300	0.283	0.0	0.0	1.583
	2,500	1.300	0.283	0.091	0.037	1.711
	5,000	1.300	0.283	0.221	0.075	1.879
	10,000	1.300	0.283	0.508	0.142	2.233
	15,000	1.300	0.283	0.836	0.208	2.627
	18,000	1.300	0.283	1.060	0.248	2.891
	25,300	1.300	0.283	1.440	0.337	3.360
	27,500	1.300	0.283	1.547	0.362	3.492
	32,300	1.300	0.283	1.779	0.416	3.778
Reflector	0	1.715	0.694	0.0	0.0	2.409
	2,500	1.715	0.694	0.004	0.002	2.415
	5,000	1.715	0.694	0.022	0.012	2.423
	10,000	1.715	0.694	0.053	0.030	2.492
	15,000	1.715	0.694	0.094	0.052	2.555
	18,000	1.715	0.694	0.135	0.072	2.616
	25,300	1.715	0.694	0.229	0.122	2.760
	27,500	1.715	0.694	0.258	0.137	2.804
	32,300	1.715	0.694	0.324	0.172	2.905

throughout lifetime. These calculations, along with their impact on the fuel rod diametral expansion as it relates to a LOCA, are presented in Reference 52. Table 23 lists the internal fuel rod gas pressure reported in Reference 52, and extended to 30,000 EFPH. The table shows that the calculated internal pressures are well below the coolant pressure of 2000 psi at beginning of life and 1600 psi after 18,000 EFPH.

Table 23 - Calculated Internal Fuel Rod Gas Pressure

	Internal Gas Pressure (psi)*			
Fuel Rod	BOL	5000 EFPH	18,000 EFPH	30,000 EFPH
Seed	114	180	455	730
Power Flattening Blanket	110	134	217	255
Standard Blanket	105	121	181	223
Reflector	172	176	189	207

*Pressure corresponding to reactor normal operating temperature at maximum allowable power prior to a postulated LOCA transient.

5.8.3 - Impact of Fission Gas Internal Pressure on Loss-of-Coolant Accident

Reference 52 presents the results of an analysis where a combined LOCA and seismic accident are evaluated. From this analysis, it was concluded that the diametral expansion and cladding stresses and strains resulting from these accidents using the calculated gas pressures within the LWBR fuel rods were within acceptable limits. A summary of the results of this assessment is given in Table 24.

Table 24 - Summary of Results of Assessments of Seismic and LOCA Events

Assessment	Cases Examined	Limiting Rod - Time in Life	Results	Design Limit	Safety Margin (%)
Cladding Diameter Increase	1. Hottest Rod	Standard Blanket - BOL	3.29%	5%	52
	2. Average Rod in Hottest Module	Seed - BOL	0.57%	5%	770
Cladding Stress	1. Average Rod in Hottest Module	Seed - 18,000 EFPH*	Generalized Stress (σ_g) = 1782 psi	σ_g <6600 psi	270
Cladding Strain	1. Average Rod in Hottest Module	Seed - 18,000 EFPH	Generalized Strain (ε_g) = 0.39%	ε_g <13.6%	>1000

*Although cladding stress is higher at 28,730 EFPH, the stress limit is much higher due to lower cladding temperature. The net result is that 18,000 EFPH is the most limiting time in life.

5.9 - CLADDING FATIGUE

Cladding fatigue was evaluated from two perspectives: (1) low-cycle fatigue adequacy, and (2) fracture mechanics evaluation assuming an initial cladding surface flaw.

Analysis of low-cycle fatigue adequacy was based on cladding creep conditions during low-frequency power cycling. This method set a limit on the number of cycles permitted as a function of plastic strain range (i.e., the change in plastic strain per power cycle). The design analysis procedure required that a total number of cycles equivalent to an average of one cycle per day over core lifetime be accommodated within the established design curve of Reference 53 for irradiated Zircaloy material. Since, for a fuel element in any one region of the core, the plastic strain range changes throughout lifetime, the number of cycles at each strain range was ratioed to the allowable number of cycles for that strain level from the design curve. The sum of all ratios was then the fatigue usage factor for that fuel element.

The LWBR limit for swing load fatigue was a usage factor of 0.8. Conservative assessments indicated that the fuel rods in all fuel regions met this criterion. Seed and reflector rods had calculated fatigue usage factors less than 0.1 due to their predicted low cladding stresses. Blanket rods had a usage factor of 0.8 based on the design specification of 1095 swing load cycles plus the allowable number of startups, shutdowns, scrams, and pressure-power cycles specified in Table 2. Since all rods were within the 0.8 usage factor limit on a conservative design basis, it was feasible that the LWBR plant could meet the operations objective of demonstration of load-follow capability.

Irradiation testing of two short (6.1-inch fuel stacks in 11.3-inch rods) test rods under daily swing load conditions also indicated that core rods were capable of load-follow operation. These rods were representative of LWBR blanket rods in diameter and cladding heat treatment (SRA). The two rods were subjected to 260 cycles between 20 and 100 percent power in a test reactor with no deleterious effects. This test rod experience supported the low-cycle

fatigue adequacy of blanket cladding over approximately one-fourth of the required number of cycles.

The fracture mechanics evaluation, in which the stress cycling of cladding material assuming an existing flaw was considered, was analyzed using stress intensity factors similar to those used in the analysis of stress corrosion cracking. If cladding stress levels at a surface flaw were greater than the SCC threshold stress, then the SCC mechanism dominated and fatigue effects were not limiting. Since cladding stresses were maintained below the SCC threshold stress as described in Section 5.4, the major concern was crack propagation due to stress cycling fatigue at the lower stress levels.

The LWBR design limit for crack propagation at a surface flaw was one-tenth the cladding thickness. It was shown by stress intensity analysis that initial defects on the order of 1.4 mils deep would be required to propagate through more than one-tenth the cladding thickness at stress levels equal to the SCC threshold stress. Surface examination of blanket production tubing revealed an average flaw depth of 0.19 mil, and a maximum of 0.73 mil among 19 tubing samples as shown in Reference 28. Thus, tensile cycling fatigue at a flaw location was insignificant relative to the stress corrosion mechanism, which was controlled by administrative restrictions on power operations, as described previously.

5.10 - ENDCLOSURE WELDS

The welding of endclosures in fuel rods must provide high-integrity, leakproof sealing of the fuel within the cladding. Equally important, the welds must be designed to ensure that they will not fail in fatigue under the relatively large cyclic axial loads to which they can be subjected during power cycling of the reactor plant. Bottom end welds in LWBR fuel rods were potentially subject to cyclic loading as the result of a thermal gravity-ratchetting effect of the fuel pellet stack induced by large power changes. The top end welds were not subjected to this problem because the top endclosure was effectively decoupled from the fuel stack by a plenum chamber which contained a coil spring for accommodating differential length changes.

A new type of endclosure referred to as the "friction grip endclosure" (Reference 54) was devised for LWBR fuel rods. This type of endclosure had a significantly greater fatigue life than the more conventional tapered insert design. Schematics of the two types and the force balances are shown in Figure 13. The friction grip endclosure had a cylindrical insert with a controlled interference fit; hence, a substantial fraction of the applied load was diverted from the weld to the press fit between the endclosure and the cladding.

A fatigue assessment of endclosure capability in LWBR fuel rods was based on the actual core power operation to 18,000 EFPH. Results of the assessment indicated that the fatigue usage factor of the bottom end welds in all types of fuel rods was well below the maximum allowable usage factor of 0.8 as shown in Table 25.

A review of prototypic testing of blanket and seed endclosure joints confirmed the conclusions drawn from analytical considerations alone. No evidence of looseness was observed in tests performed with the endclosure design employed in the LWBR fuel rods. In fact, residual joint elasticity was found to be present after rather long exposure times (20,000 hot water hours) under conditions conducive to material stress relaxation.

From the foregoing considerations, it was concluded that acceptable performance of the fuel rod endclosure was expected to 30,000 EFPH. It is noted that this conclusion was based on the following conservatively chosen computational factors for the fuel rod end connectors:

1. Endclosure temperatures of 600F for seed and blanket rods were assumed to act continuously for 50,000 hot water hours.
2. Upper-bound fast neutron fluxes were selected, producing greater than expected fluence levels.
3. Endclosure axial friction loads were conservatively calculated.
4. Comparison of axial friction loads applicable to 18,000 EFPH were made with the preloads calculated at 30,000 EFPH.

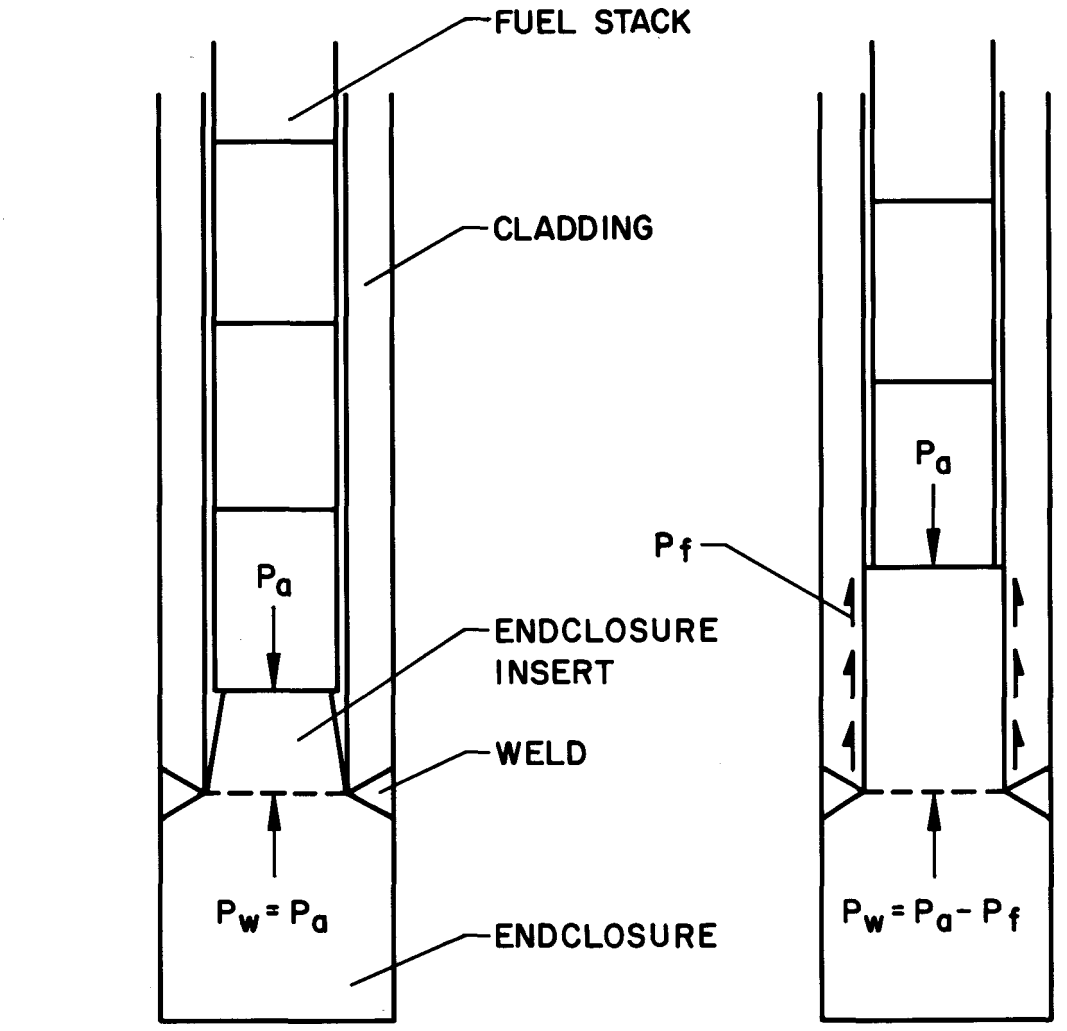

LEGEND: P_a = LOAD APPLIED TO ENDCLOSURE

P_w = WELD LOAD

P_f = FRICTIONAL RESISTING FORCE

Figure 13. Tapered Insert and Friction Grip Endclosures

Table 25 - Endclosure Weld Fatigue to 18,000 EFPH

Fuel Rod Type	Bottom End Weld Fatigue Usage Factor	
	365 Power Cycles*	1197 Power Cycles†
Seed	0.09	0.25
Power Flattening Blanket	0.10	0.32
Standard Blanket	0.10	0.32
Reflector	0.13	0.44

*Approximate number of power cycles, including 250 swing load cycles, estimated to occur in LWBR core through 30,000 EFPH.
†Number of LWBR design cycles, including 1095 swing load cycles.

An out-of-pile cyclic load test of a friction-grip endclosure representative of those used on an LWBR seed fuel rod resulted in satisfactory performance for 60,000 loading cycles. The 60,000 loading cycles were considerably in excess of the number of loading cycles during LWBR operation, including appropriate safety factors to account for unknowns in the analytical procedures. Details of the proof test are given in Reference 54.

The friction grip endclosure offered advantages in addition to improving the fatigue resistance of bottom end welds. It was easier to weld than the tapered insert design. Experience showed that the weld location was not as critical due to the uniformity of heat transfer between the endclosure and tubing along the entire length of the cylindrical insert during welding. Also, the press-fitted assembly of a cylindrical insert provided better dimensional control with respect to perpendicularity of the endclosure, thus eliminating a potential straightening operation.

The friction grip concept was also applied to the top endclosure to facilitate welding at the top end of the fuel rods. Welding operations using tapered insert endclosures required a tack weld to hold the top endclosure in place against the force of the plenum spring during the end weld operation. The tack welds were believed to introduce surface perturbations and localized

heat conductance paths, causing weld defects. Tack welding was eliminated by using the friction grip endclosure with a press-fit length sufficient to withstand the force of the plenum spring before and during welding.

5.11 - DEFECT OPERATION

5.11.1 - Design Concern

Cladding defects should not lead to further loss of cladding integrity or ejection of fuel material into the coolant.

5.11.2 - Design Basis

LWBR fuel rods were designed to operate over full lifetime and under all normal and abnormal design modes in such a manner that through-cladding defects were not expected to occur. However, as core lifetime was extended, the probability of cladding defects occurring, while small, was increased. Likely defect mechanisms included cladding collapse and pellet-cladding interaction. Although these mechanisms were evaluated as low-probability isolated events, a design basis for defect operation was established. The design basis was that the defect was not self-propagating, considering the consequences of massive hydriding and waterlogging, and did not lead to a more extensive failure condition which could result in damage to adjacent rods (e.g., by fuel deposition on adjacent rods leading to accelerated corrosion).

5.11.3 - Analysis

Successful defected fuel rod operating experience was demonstrated in the LWBR irradiation test program (References 9 and 10).

A series of in-pile tests was performed using fuel rods with intentional defect holes drilled through the cladding. The objective of these tests was to demonstrate the inherent stability of bulk ThO_2-UO_2 oxide fuel and the good performance of Zircaloy-clad fuel rods, even in the presence of a cladding defect. The defected rods successfully operated up to 20,000 EFPH with no loss of cladding integrity or unacceptable release of fission products. All of the defected rods had high levels of corrosion at the cladding inner surface (relative to the outer surface), and high levels of hydrogen pickup in the

cladding (relative to nondefected rods). Several rods had localized massive hydriding that resulted in through-cladding cracks. However, none of the irradiation test rods experienced gross failure in-reactor, no detectable fuel was released, and adjacent rods in the same test holder were unaffected.

5.11.4 - Corrosion Model for Defected Rods

A design procedure for the calculation of oxide weight gain and film thickness for the inside surface of defected rods was qualified to available inside diameter oxide thickness measurements (Reference 9). This procedure is based upon the CHORT computer program (Section 5.6), which was modified to account for the additional corrosion caused by fission activity on the inner Zircaloy cladding surface. Since surface fissioning enhancement effects are assumed to be caused by fission product recoil, the enhancement effect is linear with respect to time and directly proportional to the fuel fissioning rate.

However, hydrogen concentrations were higher than predicted in the lower power segments of the defected Zircaloy fuel rods and were not proportional to oxide thickness (Reference 9). Thus, hydrogen absorption models like CHORT (in which hydrogen pickup is calculated to be directly proportional to local corrosion oxide weight gain and film thickness) are adequate for the prediction of external hydrogen in nondefected rods. They are unsuitable for prediction of axial hydrogen distribution in defected Zircaloy rods.

5.11.5 - The CHORT Program Calculations

In order to assess the inside diameter rod corrosion weight gain and oxide thickness for defected LWBR core rods, a detailed 25,000 EFPH operation history was constructed for each rod type (seed, standard blanket, power flattening blanket, and reflector). The history was that of the hottest spot in the hottest rod (peak power and heat flux) from each category.

Next, CYGRO analysis was performed for each rod type throughout life. This program generated the essential temperature and irradiation history for the inside diameter surface of each rod. These data were then used as input to the CHORT computer program for the determination of oxide weight gains and

thicknesses. A summary of the CHORT input data for each rod type is included in Table 26. In the analysis, temperature and irradiation time steps were omitted for operation at <400F. This simplification was possible because the contribution to corrosion in this low-temperature regime is negligible.

Analysis of operations beyond 25,000 EFPH was performed, assuming that the core would operate at 50 percent power for an additional 10,000 hot water hours. This projected power history was a conservative representation of the actual power history. Results of the CHORT analysis are presented in Table 27 for all rod types.

The results of CHORT analysis for the case of defected rods occurring at various periods in core lifetime (after 10,000 to 25,000 EFPH) are listed in Table 28. The CHORT-calculated outside diameter corrosion oxide thickness, tabulated in Section 5.6, are combined with the inside diameter values in Table 27 to give a total corrosion film thickness and metal loss.

5.11.6 - Discussion of Results

The data of Table 27 shows that the calculated loss of Zircaloy cladding at the peak power position for all LWBR rod types due to internal corrosion is ≤3.4 mils at 30,000 EFPH. When combined with the maximum 1-mil loss for

Table 26 - CHORT Input Parameters for Defected LWBR Core Rod Calculations to 25,000 EFPH

Rod Type	Cladding Condition	Cladding ID Temperature (F)		Fast Neutron Flux (10^{13} n/cm^2-sec)		Rod Surface Fissioning Rate (10^{13} f/cc-sec)	
		Minimum	Maximum	Minimum	Maximum	Minimum	Maximum
Seed	RXA	694.7	732.3	4.0	8.7	0.88	2.16
Standard Blanket	SRA	705.7	724.4	4.0	8.3	0.57	0.84
Power Flattening Blanket	SRA	698.8	726.8	3.2	6.4	0.47	0.89
Reflector	SRA	660.7	705.4	0.16	0.35	0.01	0.17

Table 27 - CHORT-Calculated Internal Corrosion Oxide Thickness for Initially-Defected LWBR Core Rods at Peak Power Position

Rod Type	Internal Oxide Thickness (mils)		Equivalent Metal Loss (mils)*	
	Best Estimate	Design†	Best Estimate	Design
		25,000 EFPH		
Seed	3.12	4.73	1.87	2.84
Standard Blanket	3.01	4.57	1.81	2.74
Power Flattening Blanket	2.72	4.13	1.63	2.48
Reflector	1.33	2.05	0.80	1.23
		30,000 EFPH		
Seed	3.79	5.74	2.27	3.44
Standard Blanket	3.69	5.59	2.21	3.35
Power Flattening Blanket	3.36	5.09	2.02	3.05
Reflector	1.78	2.72	1.07	1.63

*Equivalent metal loss is 0.6 times the oxide thickness.
†Design value is 1.5 times the best estimate plus a 0.05 mil constant.

outside diameter corrosion given in Section 5.6, a total metal loss of 4.4 mils is calculated.

The absence of significant coolant activity in LWBR early in life indicated that there were no fuel rod cladding defects. In order to eliminate initial defect formation due to internal (primary) hydriding in LWBR fuel rods, hydrogeneous materials inside the fuel rod were minimized by stringent controls on the manufacturing process (Reference 42). Thus, the calculations listed in Table 28 are more realistic.

This data shows that defects occurring later in core life would have much less internal oxide corrosion and less reduction in thickness of the Zircaloy cladding. In addition, defected LWBR irradiation test rods successfully

Table 28 - CHORT-Calculated Corrosion at 30,000 EFPH for Defected LWBR Core Rods at Peak Power Positions

Rod Type	Corrosion Oxide Film Thickness (mils) Internal Best Estimate	Internal Design	Combined* Best Estimate	Combined* Design	Total Equivalent Metal Loss (mils)†
		Defected After 10,000 EFPH			
Seed	2.32	3.53	3.40	5.15	3.09
Standard Blanket	2.39	3.64	3.49	5.29	3.17
Power Flattening Blanket	2.11	3.22	3.14	4.77	2.86
Reflector	1.28	1.97	2.14	3.26	1.96
		Defected After 15,000 EFPH			
Seed	1.74	2.66	2.82	4.28	2.57
Standard Blanket	1.79	2.74	2.89	4.35	2.61
Power Flattening Blanket	1.61	2.47	2.64	4.02	2.41
Reflector	1.00	1.55	1.86	2.84	1.70
		Defected After 20,000 EFPH			
Seed	1.23	1.90	2.31	3.52	2.11
Standard Blanket	1.26	1.94	2.36	3.59	2.15
Power Flattening Blanket	1.15	1.78	2.18	3.33	2.00
Reflector	0.75	1.18	1.61	2.47	1.48
		Defected After 25,000 EFPH			
Seed	0.67	1.06	1.75	2.68	1.61
Standard Blanket	0.68	1.07	1.78	2.72	1.63
Power Flattening Blanket	0.64	1.01	1.67	2.56	1.54
Reflector	0.45	0.73	1.31	2.02	1.21

*Total inside and outside diameter oxide thickness at 30,000 EFPH.
†Total equivalent metal loss is 0.6 times the combined design oxide thickness.

operated up to 20,000 EFPH with internal oxide corrosion film thicknesses up to 3.6 mils and localized hydrogen contents up to 16,300 ppm (Reference 9).

5.11.7 - Fuel Rod Failure*

During power operations, incidents such as stress corrosion cracking (SCC), fuel swelling, pellet-cladding interaction, power ramps, and aggressive fission product attack, could cause a breach in the cladding and allow coolant to enter and hydride the rod. The technical concern connected with the hydriding of such operationally defected rods is that as the degree of hydriding increases in severity, the probability of survival during operation decreases. Gross hydriding could create a large opening in the cladding through which appreciable amounts of fission products and fuel would be released to the coolant. The resulting high-radioactivity level might impose operating restrictions on the reactor plant. In addition, released fuel could deposit on neighboring rod surfaces and result in accelerated cladding corrosion, defect formation, and even failure of the contaminated rods.

It was judged that there was low probability of the above sequence of events occurring in the LWBR core. By careful manufacturing procedures, successful initial operation without any apparent defects, conservative operational and design limits, the possibility of in-pile fuel rod defection was minimized, but not necessarily eliminated. For example, since more of the long-lived ^{129}I isotope is generated with a longer core life, it was critical that the LWBR iodine SCC limits not be exceeded at higher depletion levels. Yet, even such an incident need not lead to catastrophic failure. One LWBR irradiation test rod defected during test reactor operation, due to iodine SCC, but operated successfully (~12,000 EFPH) even though massively hydrided (Reference 9).

---

*A defect is a breach of cladding integrity [i.e., a perforation (slit, crack, or pinhole)] that slowly leaks fission products to the coolant. Many defected Zircaloy-clad fuel rods have operated satisfactorily in commercial reactors without diminishing core performance (Reference 10). Failures consist of gross cladding loss, high activity levels, and contamination of the coolant by particulate fuel; they must be removed from the reactor to avoid serious air, coolant, or plant contamination.

Failure of a rod would require sufficiently massive hydride formation to affect its mechanical properties. Also, sufficient mechanical loading must occur in the hydrided areas to cause catastrophic failure. It was established through mechanical testing that severely hydrided LWBR fuel rod end connectors maintain their structural integrity (References 16 and 55). In addition, the thoria-low urania LWBR fuels exhibited high corrosion-erosion stability in both in-pile and out-of-pile tests (Reference 8) and release of fuel through cladding defects would be minimal. Finally, surveys of defected and failed fuel rod operation revealed that no multiplication of failures occurred even with severe overheating and cladding loss (References 56 and 57).

Locke (References 56 and 58) has developed an empirical approach for analyzing coolant hydride failures. His analysis correlates the period of time a defect rod can operate in-pile before failure with the surface heat flux. Surface heat flux determines both the thermal gradient and the inside cladding temperature for a given geometry and coolant temperature. Heat flux is a function of the fuel fission rate. Locke compiled the available in-pile data up to 1979 (including some Bettis Laboratory data) on both intentionally and operationally defected Zircaloy-clad fuel rods and drew a limit line on the plot of the rod heat flux versus days to failure after defection. He concluded that limiting levels of operation are about 380,000 to 475,000 Btu/hr-ft^2 peak flux at a coolant temperature of 500 to 626F, should it be desirable to operate with defective fuel for an extended period of time.

The peak heat flux history for the LWBR seed rods, listed in Table 29, is compared with Locke's limit line in Figure 14. The peak heat fluxes for LWBR seed and blanket rods were initially $\leq$375,000 Btu/hr-ft^2 and decreased sharply near the beginning of life. For defects occurring at the beginning of life on a seed rod, the time to failure was about 190 days (4560 EFPH). As the core continues to operate, the peak heat fluxes continued to decrease and the time to failure increased until a point was reached beyond which the days remaining in core life are less than the days to failure. The data in Table 29 shows

that defects occurring in seed rods after 9000 EFPH, when the remaining core life was 21,000 EFPH, would have 24,000 EFPH (1000 days) to failure. Similar results were obtained for the blanket rods.

Table 29 - Comparison of Core History and Failure Limit for Defected LWBR Seed Rods

Heat Flux* (10^3 Btu/hr-ft^2)	Core Elapsed Time		Core Time to EOL (days)	Time to Failure† (Days)
	EFPH	EFPD*		
374	0	0.0	1250.0	190
338	1,000	41.7	1208.3	260
291	3,000	125.0	1125.0	400
275	4,500	187.5	1062.5	460
259	6,000	250.0	1000.0	550
244	7,500	312.5	937.5	880
232	9,000	375.0	875.0	1000
223	10,500	437.5	812.5	1050
211	12,000	500.0	750.0	1100
199	13,500	562.5	687.5	1140
197	15,000	625.0	625.0	1140
193	16,500	687.5	562.5	1140
194	18,000	750.0	500.0	1160
160	19,500	812.5	437.5	1250
162	21,000	875.0	375.0	1250
165	24,000	1000.0	250.0	1230
175	27,300	1137.5	112.5	1210
133	30,000	1250.0	0.0	1320

*These columns are plotted as the operating line in Figure 14.
†Obtained from Figure 14.

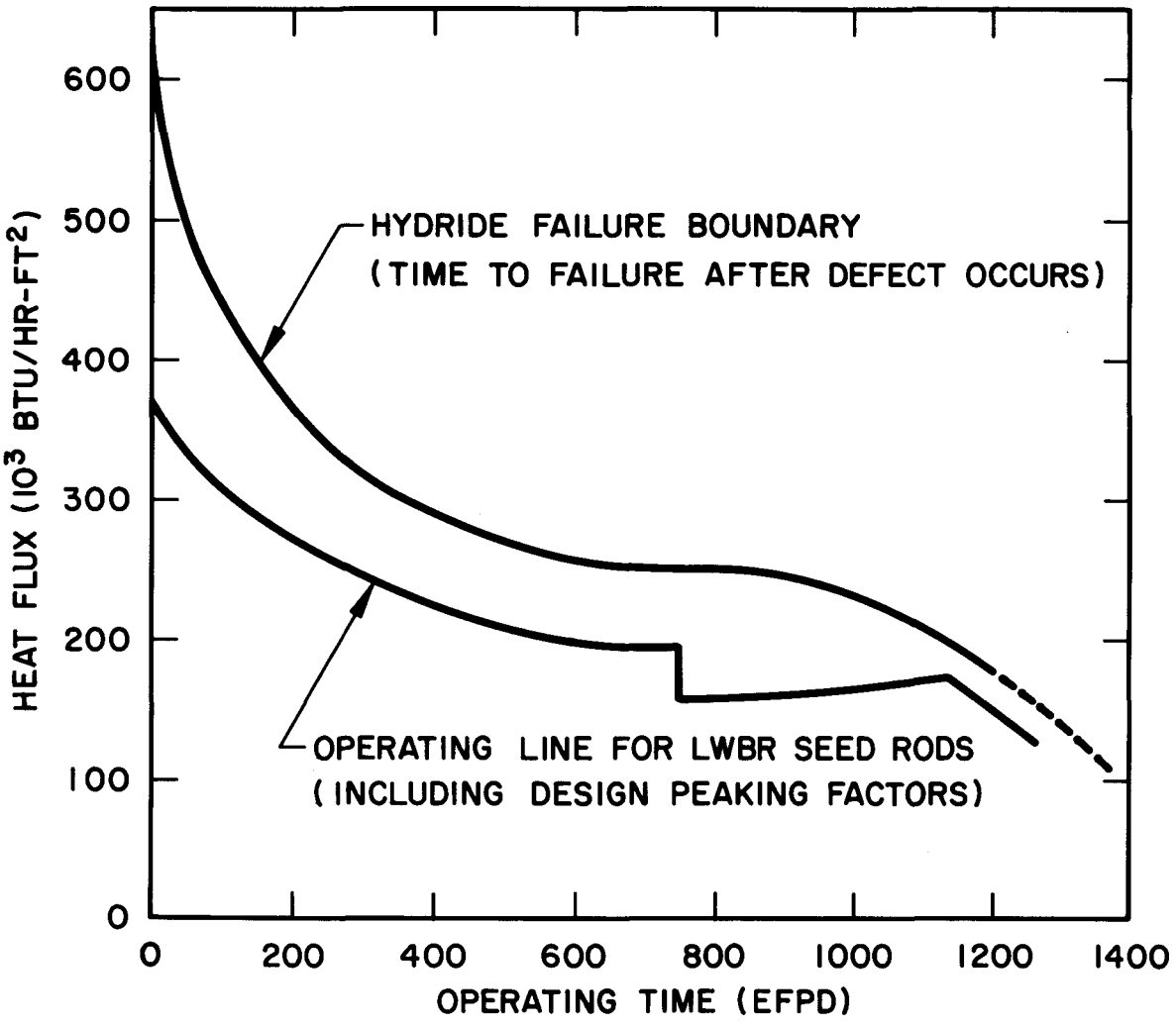

Figure 14. Hydride Failure Limit for Defected Zircaloy-Clad Fuel Rods

The significance of this analysis was that it predicted that core operation with defected fuel rods to a lifetime of 30,000 EFPH was possible even if some fuel rod defects should occur any time after 9000 EFPH. It was realized that this treatment was very qualitative since it was based primarily on the empirical relationship between heat flux and excessive hydriding with no attempt to include factors such as operational history or fuel and fabrication differences. However, since the time of defect detection was often different from the time of defection and since several of the intentionally defected LWBR test rods successfully operated at heat fluxes above Locke's limit (Reference 8), the correlation appeared conservative. Also, the results of LWBR irradiation tests, where both intentionally and operationally defected fuel rods survived accelerated and massive hydride attack, demonstrate that continued safe operation of defected fuel rods in LWBR was feasible. This judgment was consistent with current commercial core experience in which operation continues with about 0.1 percent of the rods in a defect condition (References 48, 56, and 58). LWBR fuel rods, with their lower power rating and high corrosion-erosion resistant thoria-based fuel system, should have longer defected rod lifetime than commercial reactor fuel rods.

5.11.8 - Summary

Based on CHORT calculations and LWBR irradiation test data, it was concluded that the additional internal corrosion oxidation and hydriding in a defected LWBR fuel rod need not significantly degrade its irradiation performance. Defected LWBR irradiation test rods successfully operated in a test reactor up to 20,000 EFPH with internal oxide corrosion film thicknesses up to 3.6 mils and localized hydrogen contents up to 16,300 ppm. In addition, an assessment of the performance of LWBR defected fuel rods, based on an empirical surface heat flux approach developed by Locke (References 56 and 58) predicted that successful defected fuel rod operation was possible even if some fuel rod defects should occur after 9000 EFPH. Thus, except for the unlikely event of a large cladding rupture, defects in LWBR fuel rods should be benign. The

maintenance of basic fuel integrity and no excessive release of fuel to the coolant from defected LWBR fuel rods was anticipated.

5.12 - CLADDING WEAR

Support grid contact with the fuel rods was expected to cause wear marks on the cladding surface. Maximum wear depths were calculated using the procedure outlined below. On a worst-case basis, maximum wear depths of 5.0 mils on seed rods and 8.4 mils on blanket rods were predicted for 29,100 EFPH lifetime and 39,200 hot water hours. Best estimates of maximum wear depths were 2.8 and 5.3 mils, respectively. The effects of cladding wear were taken into account in performance assessments of cladding stress, rod-to-rod clearance, and grid spring follow.

Two types of wear were considered in predictions of wear depth: a vibratory wear caused by flow-induced vibration of the fuel rods, and reciprocating wear caused by thermally induced motions of the fuel rods during power cycling. A prediction procedure was developed from measured wear marks on irradiation test rods and on copper-pelleted rods in out-of-pile tests. Reference 59 describes the irradiation test results used to qualify an empirical relationship for reciprocating wear developed in out-of-pile tests. Vibratory wear effects were studied in out-of-pile tests described in Reference 60. These tests used simulated fuel rods in a grid system enclosed in an autoclave capable of providing the pressure and temperature appropriate to the LWBR primary system. Reference flow rates were used for the vibratory wear tests, except for one series of reciprocating wear tests conducted dry at room temperature.

In addition to the two types of wear, consideration was given to several mechanisms that affect wear depth. Elongation of fuel rod due to irradiation-induced growth of the Zircaloy cladding and due to pellet-cladding interaction continuously moves the points of contact between cladding and support grids. This action alleviates the extent of wear since contact is not maintained at the same locations on the cladding throughout core lifetime. Benefits of a "moving" wear mark are greatest at the free-end grid level, where the maximum wear usually occurs.

Another mechanism affecting wear depth is overlay wear. After a grid contact point has moved on to fresh cladding due to rod elongation, subsequent core operation at lower power levels could return the contact point to a previous wear location and work it deeper. The overlay wear mechanism was included in the procedure due to its significance in extended lifetime operation at reduced power levels.

Additional factors entering into the wear depth predictions and included in the calculations were the effects of low spring force or loose grid cells, rod mounting (top or bottom), cladding diameter, and grid dimple dimensions. The procedure considered the potential for accelerated wear which could occur as a result of wear-induced loosening of the grid cell. Surface scratches were considered also, but these became insignificant when the imposed wear depth was greater than 1 mil.

The first step in the wear depth prediction procedure was selection of the appropriate vibrational wear rate. Wear rates obtained from flow tests for LWBR seed and blanket fuel rods are listed in Tables 30 and 31. Values are given for operation with spring loads above and below the breakaway load, which is the threshold load between loaded cells and loose cells. A loose cell may have contact with the rod, but the force is low enough to permit significant rod vibration.

The wear rates in Tables 30 and 31 were derived from the depth measurements shown in the prototypic phases of the simulated rod tests described in Reference 60. Loose cells were assumed for all grid levels except at the free end. Since less cladding shrinkage and less spring relaxation were expected to occur at the end grids, the assumption of loaded cells at the free end was reasonable. Breakaway loads were 0.8 pound in seed grids and 2.0 pounds in blanket grids, based on the out-of-pile wear tests with well-characterized cell loads. Differences between top- and bottom-mounted rods were negligible except for a loose cell at the free end where the top-mounted rods had greater wear due to flow impingement on the free end of the rod. Best estimate predictions used the mean wear rates and worst-case evaluations used the 2-sigma extremes for a 95-percent confidence level.

Table 30 - LWBR Seed Fuel Rod Vibrational Wear Rates
(For Operation at Full Coolant Flow Rate)

	Top-Mounted Rods Wear Rate (mil^3/hr)		Bottom-Mounted Rods Wear Rate (mil^3/hr)	
Grid Level	Best Estimate	Worst-Case	Best Estimate	Worst-Case
Loaded Cells				
9 (Top)	<0.026	<0.102	0.039	0.141
8	<0.026	<0.102	0.036	0.134
7	<0.026	<0.102	0.034	0.126
6	0.026	0.102	0.031	0.117
5	0.029	0.111	0.029	0.111
4	0.031	0.117	0.026	0.102
3	0.034	0.126	<0.026	<0.102
2	0.036	0.134	<0.026	<0.102
1 (Bottom)	0.033	0.095	<0.026	<0.102
Loose Cells				
9 (Top)	<0.026	<0.102	0.048	0.176
8	<0.026	<0.102	0.036	0.134
7	<0.026	<0.102	0.034	0.126
6	0.026	0.102	0.031	0.117
5	0.029	0.111	0.029	0.111
4	0.031	0.117	0.026	0.102
3	0.034	0.126	<0.026	<0.102
2	0.068	0.250	<0.026	<0.102
1 (Bottom)	50.700	138.500	<0.026	<0.102

Table 31 - LWBR Blanket Fuel Rod Vibrational Wear Rates
(For Operation at Full Coolant Flow Rate)

	Top-Mounted Rods Wear Rate (mil^3/hr)		Bottom-Mounted Rods Wear Rate (mil^3/hr)	
Grid Level	Best Estimate	Worst-Case	Best Estimate	Worst-Case
Loaded Cells				
8 (Top)	0.003	0.107	1.810	3.410
7	0.110	0.270	1.180	2.100
6	0.170	0.430	0.710	1.390
5	0.250	0.590	0.460	0.960
4	0.460	0.960	0.250	0.590
3	0.710	1.390	0.170	0.430
2	1.180	2.100	0.110	0.270
1 (Bottom)	0.650	1.810	0.003	0.017
Loose Cells				
8 (Top)	0.004	0.018	8.400	14.620
7	0.160	0.600	0.740	3.200
6	0.310	0.910	0.710	2.330
5	0.480	1.260	0.650	1.690
4	0.650	1.690	0.480	1.260
3	0.860	2.340	0.310	0.910
2	1.070	3.350	0.160	0.600
1 (Bottom)	10.240	23.300	0.004	0.018

Wear depth was then calculated from the equations in Table 32. The depth due to vibrational wear (h_v) was determined by first choosing between a stationary or a moving wear spot at each grid level. Due to the relatively low growth of RXA Zircaloy (about one-fifth that of SRA Zircaloy), the applicable vibrational wear depth for seed rods is given by the formula for a stationary wear spot. In blanket rods, the applicable vibrational wear depth is given by the formula for a moving wear spot. An exception was made for the two cells nearest the fixed end of blanket rods. The stationary wear spot formula is more applicable to those grid cells.

Table 32 - Summary of Cladding Wear Spot Depth Calculation

$$h_v = \left(\frac{\dot{V}t}{\beta}\right)^{1/2} \quad \text{(stationary wear spot)}$$

$$h_v = \left(\frac{9}{16D}\right)^{1/3} \left(\frac{\dot{V}}{u}\right)^{2/3} \quad \text{(moving wear spot)}$$

$$N_v = 10^{\gamma},$$

where:

$$\gamma = \frac{4}{3} \frac{D^{1/2} h_v^{3/2}}{L^{1/3}} \left(\frac{1}{0.484s + 34.1}\right) + 1.47$$

$$N_r = \frac{ns}{u} \quad \text{(moving wear spot)}$$

$$N_e = N_v + N_r$$

$$A_e = L^{1/3} (0.227s + 16) (2.13 \log N_e - 3.13)$$

$$h_e = \left(\frac{9}{16D}\right)^{1/3} A_e^{2/3}$$

$$\Delta h = f \left(\frac{\Delta V}{2(2 r D)^{1/2} h_e^2}\right) \quad \text{(Appendix A1)}$$

$$h_T = h_e + \Delta h,$$

Table 32 - Summary of Cladding Wear Spot Depth Calculation (Cont)

where:

h_v = wear depth from vibratory wear (mils)

$\dot{V}$ = vibrational wear rate (mil^3/hr)

t = accumulated time in hot water at >400F (hours)

D = fuel rod outside diameter (mils)

A_e = effective area of wear spot at cladding surface (mil^2)

ΔV = overlay wear volume (mil^3)

r = dimple radius of grid spring or reaction dimple (mils)

s = stroke length due to power cycling (mils)

u = net elongation velocity of fuel rod relative to grid (mils/hr)

n = number of power cycles performed per hour

L = grid spring load (pounds)

$\beta = \pi \sqrt{rD/2}$ (mils)

N_e = effective number of reciprocating cycles

N_v = equivalent number of reciprocating cycles to produce a given wear depth due to vibrational wear alone

N_r = number of reciprocating cycles; use actual number for a stationary wear spot and above formula for a moving wear spot

h_e = net wear depth (mils)

Δh = overlay wear depth - moving wear spot only (mils) from Appendix A1, Figure A1-2 or A1-3

h_T = total wear depth (mils)

Derivations of the vibrational wear equations are supplied in Appendix A1. Vibrational wear depth at a stationary wear spot was derived from an

approximation to the common volume in crossed cylinders, representing the geometries of the cylindrical spring or dimple of the grid system (Reference 11) in contact with the cylindrical fuel rod. The equation in Table 32 for vibrational wear depth at a moving spot represents the equilibrium value resulting from the common crossed-cylinders volume being spread out longitudinally on the rod.

Following calculation of vibrational wear depth, the depth value was converted into an equivalent number of reciprocating cycles (N_v) that would produce the same depth. This relationship is based on an empirical correlation between wear mark area, spring load, stroke length, and the number of reciprocating cycles as shown in Reference 59. The number of actual reciprocating cycles (N_r) was then added to N_v to obtain the net effective number of cycles (N_e). The remaining equations in Table 32 follow those of Reference 59 for calculating the net wear depth (N_e) caused by the combined effects of vibrational and reciprocating wear.

For those rods with either stationary or moving wear spots, an overlay wear (Δh) component was added to the net wear. Equations used to calculate overlay wear are described in Appendix A1. Two sources of overlay wear which existed in the LWBR fuel system were:

1. Overlay wear due to fuel rod vibration during plant shutdowns for scheduled maintenance: During a typical plant shutdown, the four coolant pumps were operated at half speed for a period of approximately 4 weeks. The flow-induced vibration of the fuel rod which occurred at a reduced coolant flow velocity during this period resulted in additional vibrational wear, which must be added to that occurring during power operation.

2. Overlay wear due to reductions in core power: This source of overlay wear was applied only to moving wear spots developed in blanket fuel rods. The overlay dwell period was about 2000 hours for a 10 percent power reduction.

No overlay wear depth increment due to power reduction occurs at a stationary wear spot (e.g., wear spots in LWBR seed fuel rods and in blanket fuel rods at grid locations near the fixed end to which the stationary wear spot model applies). This is because the wear contact site of a stationary spot does not, by definition, move relative to the grid at any time in life. Hence, only the overlay wear due to the fuel rod vibration during plant shutdowns was considered for stationary wear spots.

Overlay wear contributions to the total wear listed in Table 33 for LWBR blanket rods were as high as 2.1 mils (best estimate) and 2.9 mils (worst-case). These maximum values occurred at the top grid level of a bottom-mounted rod, and represent about 40 percent of the total predicted wear depth.

The wear depth equations presented in Table 32 apply to the case of wear spots having a depth which does not exceed the depth at which the circumferential width of the spot becomes equal to the width of the cylindrical surface of the grid dimple. Departure from ideal crossed-cylinder contact conditions results in an increase in the wear depth developed for a given amount of wear volume. This is referred to as the "finite dimple width effect". A procedure is described in Appendix A1 for calculating wear depth for cases in which the depth exceeds that at which the wear spot width becomes equal to the dimple width. For LWBR rods, spring and dimples (including beveled ends) were of sufficient width that the finite dimple width effect did not enter into the wear depth calculation.

Results of wear depth calculations for LWBR rods are given in Tables 33 and 34 for blanket and seed rods, respectively. Worst-case wear depths at the high-duty locations (grid levels 4 through 6) were used in the calculation of local cladding stresses in fuel rod performance analyses.

5.13 - PELLET INTEGRITY

Fuel pellets to be loaded into fuel rods were required to meet dimensional, geometric, density, and loading specifications and to be free of surface defects in excess of specified limits. Integrity of manufactured pellets was assured by inspections at each station of the fabrication process and by evaluation of in-motion radiographic film of the final fuel rod. Maintenance of

Table 33 - LWBR Blanket Rod Wear Depths
(Predicted for 29,100 EFPH with
Full Coolant Flow Rate)

Grid Level	Top-Mounted Rods Wear Depth* (mils)		Bottom-Mounted Rods Wear Depth* (mils)	
	Best Estimate	Worst-Case	Best Estimate	Worst-Case
8 (Top)	0.6	1.5	5.3	7.6
7	4.1	8.4	3.2	7.3
6	4.9	7.4	3.2	6.3
5	3.9	7.0	3.2	5.9
4	3.7	6.5	3.1	5.4
3	3.8	6.7	3.1	6.0
2	3.9	7.6	4.3	8.4
1 (Bottom)	3.3	5.3	0.7	1.5

Table 34 - LWBR Seed Rod Wear Depths
(Predicted for 29,100 EFPH with
Full Coolant Flow Rate)

Grid Level	Top-Mounted Rods Wear Depth* (mils)		Bottom-Mounted Rods Wear Depth* (mils)	
	Best Estimate	Worst-Case	Best Estimate	Worst-Case
9 (Top)	<1.9	<3.6	2.8	4.2
8	<1.9	<3.6	2.3	4.1
7	<1.9	<3.6	2.2	4.0
6	1.9	3.6	2.1	3.8
5	2.0	3.7	2.0	3.7
4	2.1	3.8	1.9	3.6
3	2.2	4.0	<1.9	<3.6
2	2.7	5.0	<1.9	<3.6
1 (Bottom)	2.7	3.5	<1.9	<3.6

*Loose cells assumed at all grid levels except for loaded cells at the level nearest the free end.

pellet integrity throughout core lifetime was projected from test experience with irradiation test rods and out-of-pile pellet testing.

This section describes the effects of manufacture and operations on pellet end lands, tapers, and chamfers, and the causes and results of pellet cracking and chipping.

The fundamental goal of the fuel manufacturing process controls and product inspections was to ensure that the fuel components conformed to the established tolerance ranges. Pilot or preproduction programs established the process control parameters which yielded the best product. Many engineering tests and various inspections were performed to relate pellet quality characteristics to process parameters. These were not routinely a part of the production pellet manufacturing inspections. The fuel corrosion characteristics when exposed directly to various conditions of coolant chemistry and temperature were examined. Pellet strength properties were examined by crush testing and by thermal shock testing, consisting of an imposed rapid and extreme temperature change. The as-sintered pellet dimensional stability was examined under conditions of high-temperature exposure for extended times. Extensive product inspections during these pilot programs demonstrated the degree of uniformity in product quality.

During in-production manufacture of fuel pellets, the various steps of powder preparation (such as blending, micronizing, and agglomerating) involved tight process controls prior to compacting the powder into fuel pellets. After pellet compaction, there were inspections of the pellet dimensions, density, and quality (cracks, surface laminations, and other irregularities). The pellets were processed through a pretreat furnace to remove organic binders and through a sintering furnace with atmosphere and temperature control to achieve stable density and dimensions under extended exposure to high temperatures. These pellets were ground to the specified uniform diameter and specified pellet end taper or chamfer configuration. The pellets were processed through a vacuum degassing furnace to minimize moisture or gas content, and subsequently maintained under strict exposure limits of time at humidity and temperature until finally being sealed in a helium atmosphere within the fuel rods.

All pellets in a particular pellet blend were produced from a single mixture or blend of fuel powder. A blend was processed uniformly through the fabrication sequence at a single set of controlled process parameters. Hence, an unacceptable characteristic discovered in the samples examined from a blend was considered to be an unacceptable characteristic of that blend. Conversely, if samples inspected from a blend demonstrated an acceptable high quality, then there was increased assurance that all products within that blend were of uniformly acceptable high quality in that attribute. The pellet inspections determined acceptable pellet quality and also verified the pellet-to-pellet uniformity within the blend. The pellet sampling plan is given in Reference 61.

The chemical composition characteristic of each blend was analyzed to determine isotopic concentration of any contaminants or impurities, the total uranium and total fissile content, as well as the uranium isotopic distribution and the uniformity of fissile content from pellet to pellet within the blend. The pellet size (length and diameter) was a distinguishable identification of pellet type by enrichment.

Both radial and longitudinal pellet cross sections were examined for grain size and distribution of grain size, as well as for internal cracks, voids, or nonuniform porosity distribution. Pellet cross sections were also examined for color or irregular color distribution, foreign inclusions, or particulate inhomogeneities. The uniformity of fissile distribution or indications of uranium microinhomogeneity beyond limits was examined by densitometer evaluation of nuclear track autoradiographs of sample pellets.

Inspections of each blend were performed to determine conformance with the specifications of pellet end perpendicularity and taper and dish dimensions. Sample pellets were inspected for conformance with the length, diameter, and ovality requirements. Pellets were also inspected to strict visual standards for integrity or surface irregularities.

A full-length radiographic inspection of every fuel rod was made at three (reflector), six (seed), or nine (blanket) different orientations. These radiographs were inspected for pellet and fuel stack integrity and plenum spring

uniformity within the finished fuel rod. Fuel chips and pellet voids detected by radiography were characterized in each fuel rod. Limits were placed on their size, location, orientation, and frequency. Rods containing fuel chips or pellet voids within specification limits were later positioned at low-duty locations in the fuel modules. Rods containing no detectable chips or voids were reserved for high-duty locations.

Various tests were performed on a sample of fabricated rods and on irradiation test rods to increase confidence that pellet integrity would be maintained throughout the core lifetime. Pellet crush tests and drop tests were performed to provide data on pellet strength and pellet integrity under shock load conditions. The plenum spring was designed to maintain pellet-to-pellet contact while permitting stack thermal expansion and irradiation swelling. Pellet end land areas, end dish dimensions, and end tapers and chamfers were used in irradiation test rods to check performance capability under irradiation and power swing conditions.

Post-irradiation examination of test rods using LWBR pellet characteristics showed that pellet integrity was maintained to depletion levels of 10.4 x 10^{20} fissions/cc in seed rods and 5.4 x 10^{20} fissions/cc in blanket rods which represent, respectively, 107 and 117 percent of design depletion levels at 18,000 EFPH, and 78 and 77 percent at 29,047 EFPH (Table 1). Chips and voids were intentionally generated in a group of 16 test rods, both seed and blanket types, and the effect on cladding integrity during power ramps was investigated. None of these test rods developed a defect, indicating that the generation of chips during irradiation is inconsequential even under power ramp conditions.

Of three other rods experiencing power ramps, two developed cladding defects and the third remained intact. One rod that developed a defect contained 17 loose chips as detected in preirradiation radiographs. The other rod that failed contained pellets with squared edges and less than 1 mil fuel-cladding clearance. The LWBR fuel rod analysis model was used to calculate cladding stresses, including chip effects, in excess of stress corrosion cracking (SCC) threshold limits for both rods. The third rod also contained chips detected in

preirradiation radiographs, but did not defect because power ramps imposed on this rod were limited to maintain calculated cladding stresses, including chip effects, below the SCC threshold stress.

From these out-of-pile and irradiation test rod experiences, acceptance limits were placed on chips and voids in fuel rods approved for core use. Generation of fuel chips during operations was accounted for in the performance evaluations, although irradiation test experience indicated no significant effect on cladding integrity within the bounds of specified power operations.

Therefore, assurance of pellet fabrication uniform high quality, radiographic inspection of the pellets in every fuel rod, and tests performed on fabricated rods as well as on irradiation test rods provided a high level of confidence that pellet integrity would be maintained throughout core lifetime.

5.14 - CLADDING DEFORMATION

5.14.1 - Design Concern

Five modes of cladding deformation were considered in evaluating LWBR fuel rod performance: (1) diametral shrinkage, (2) ovality, (3) deformation under grids, (4) ridging, and (5) grooving into pellet tapers. Diametral shrinkage could affect fuel rod thermal performance by changing rod-to-rod spacing and cladding stresses due to increased interaction between cladding and fuel pellets. Diametral shrinkage could also affect fuel rod bow and cladding wear due to loss of grid seating force (spring follow). Changes in rod-to-rod spacing due to diametral shrinkage also has an impact on fuel rod nuclear performance by locally changing the metal-to-water ratio. Excessive ovaling of unsupported cladding could result in fuel rod failure due to cladding collapse. Minor ovaling of cladding could also affect fuel rod performance by decreasing spacing between adjacent fuel rods and by decreasing clearance between rods and support structure. Localized creep of fuel rod cladding under support grid loads affects fuel rod performance by decreasing grid seating force from lost grid spring deflection and by reductions in rod-to-rod and rod-to-support structure clearances. Ridging of fuel rod cladding affects fuel rod performance by increasing cladding stresses. Finally, grooving adversely affects fuel

rod performance by decreasing rod seating force due to lost grid spring deflection and by decreasing rod-to-rod and rod-to-support structure clearances.

5.14.2 - Analytical Models

5.14.2.1 - Diametral Changes

The CYGRO computer program (Reference 14) was used to calculate diametral changes for LWBR fuel rods. The CYGRO program includes mechanistic models which influence fuel rod diametral shrinkage. The following components included in CYGRO are the major contributors to fuel rod diametral changes:

1. Zircaloy creep due to system pressure.
2. Stress-free, irradiation-induced Zircaloy growth which is dependent upon fluence and the metallurgical texture of the cladding.
3. Fuel pellet shrinkage due to densification.
4. Diameter shrinkage due to axial loads on cladding caused by pellet-cladding interaction when cladding to pellet clearances exist.
5. Diameter increase due to fuel pellet swelling when there is no radial clearance between cladding and pellets.

Separate CYGRO models were developed for blanket and reflector fuel rods with nonfreestanding cladding versus seed fuel rods with freestanding cladding.

For nonfreestanding cladding, diameter changes were assumed to be related to pressure-power cycling. A pressure-power cycle was defined as a change in fuel element operating conditions from full power and pressure, down to zero power, then a decrease in pressure. This resulted in a ratchetting mechanism in which high axial loads were applied to the fuel rod cladding after system pressure caused the nonfreestanding cladding to become oval and contact the fuel pellets, and high pellet temperatures caused differential axial expansion between the cladding and pellets. These high axial stresses, tensile in the cladding and compressive in the fuel, resulted in plastic deformation (creep) of both the cladding and fuel. The resulting deformation was manifested by cladding elongation, cladding diameter decrease, and fuel stack shrinkage. Reduction in power and system pressure resulted in release of the fuel stack. The high axial stresses were then reestablished in subsequent pressure-power cycles.

For freestanding cladding, where the cladding does not become oval under system pressure, a "chipped pellet" provision was included in the CYGRO model to account for enhanced elongation and diameter changes observed in irradiation test rods containing chips.

Input for the CYGRO models was established by comparisons with irradiation test samples from the LWBR test program. These samples were built and operated over a range which encompassed that for the fuel elements in LWBR. Input for both best fit and "upper bound" fit of the data was developed.

Calculations for diametral shrinkage were made for seed fuel rods (freestanding cladding) and standard blanket fuel rods (nonfreestanding cladding) with the highest average depletion. Table 35 presents the best estimate and upper bound predictions.

There were no specific limits for LWBR fuel rod diameter shrinkage. Both best estimate and upper bound predictions of fuel rod diameter shrinkage were used as input to other analyses (e.g., spring follow, rod spacing, rod-to-support structure clearances).

Table 35 - Fuel Rod Diameter Shrinkage

	Seed		Standard Blanket	
Time (EFPH)	Best Estimate (mils)	Upper Bound (mils)	Best Estimate (mils)	Upper Bound (mils)
18,000	1.8	6.1	3.4	5.3
30,000	2.3	8.0	4.5	6.7

5.14.2.2 - Cladding Ovality (Cladding Collapse)

The ACCEPT finite element computer program (Reference 24) and the METER Monte Carlo computer program (Reference 62) were used to evaluate LWBR fuel rods for cladding collapse. Collapse of unsupported cladding was a primary

concern for standard blanket and power flattening blanket fuel rods with non-freestanding cladding. Excessive ovaling of the cladding was most likely to occur at the top of the fuel stack (plenum region) where it was predicted that the 0.525 to 0.575 inch as-fabricated unsupported length could (as a result of cladding elongation and fuel pellet shrinkage) increase up to 2.5 inches for 30,000 EFPH operation. Cladding ovality was a minor concern for seed fuel rods with their as-fabricated 10-inch unsupported plenum lengths. Collapse of cladding over gaps which might form within the fuel stack was also a design concern. Formation of an in-stack axial gap required that a pellet become jammed somewhere in the stack. Cladding elongation and fuel stack shrinkage below the stuck pellet could result in an unsupported cladding segment. In-stack gaps greater than 0.005 inch were observed in 2.4 percent of the LWBR irradiation test rods.

The ACCEPT computer program was used for deterministic evaluation of cladding deformation over axial gaps. The ACCEPT program calculates elastic-plastic deformation of Zircaloy tubes subjected to applied pressure, temperature, and axial force. Large deformation theory is used to account accurately for finite changes in geometry. A 20-node, tri-quadratic, isoparametric, three-dimensional finite element was used in the program. The curved surfaces of the element allow accurate modeling of the tube geometry, including non-uniformities such as circumferential wall thickness variation and initial tubing ovality. The capability to model frictionless contact separation interaction of inner or outer surfaces of the tube with one or more rigid surfaces enables modeling of interaction between cladding and pellets and of axial gap growth. The material model used in ACCEPT accounted for thermal and irradiation-induced creep of the Zircaloy cladding. Different material constants were used for seed (RXA) and blanket (SRA) cladding. The material model also accounted for the anisotropic behavior of Zircaloy.

Input (material and geometry) for the ACCEPT model was based on fits to uniaxial thermal creep data, data from external pressure tubing collapse DECAG test specimens (References 63 and 64), and irradiation test specimens. Input for both best estimate and design calculations of cladding deformation over plenum axial gaps is defined in Reference 65.

Figures 15 and 16 present best estimate and design predictions for ovaling of cladding in the plenum region of seed and standard blanket fuel rods for operation up to 30,000 EFPH. For seed fuel rods, plenum ovalities were predicted to be 4 mils or less. For blanket fuel rods, best estimate plenum ovalities were predicted to be 6 mils or less. On a design basis, the predicted standard blanket fuel rod plenum ovality was 36 mils.

Figure 17 presents best estimate and design predictions for ovaling of cladding over a standard blanket fuel rod in-stack axial gap assumed to initiate early in core life. Collapse of cladding over an in-stack axial gap was predicted to occur as early as 8000 EFPH on a design basis. For a gap that grew to 1.0-inch length at 30,000 EFPH, the best estimate predicted ovality was 24 mils.

The METER computer program was used for probabilistic assessments of cladding collapse over plenum and in-stack axial gaps. Probabilistic assessment of cladding collapse was required when cladding stability over worst-case calculated in-stack axial gaps throughout core life could not be demonstrated with deterministic design calculations. A response function of the form:

$$W(t, Z(i)) = w_0 \sum \exp\{CF[A(i)\ Z(i) + Z(1)\ B(1,i)\ Z(i)]\},$$

where:

w = cladding ovality

w_0 = best estimate ovality at time of interest

$A(i)$, $B(1,i)$ = fitting coefficients at time of interest

$Z(i)$ = set of random input parameters (coded values)

CF = correction factor which accounts for nonconservatism in system function when more than one parameter is perturbed from the best estimate value.

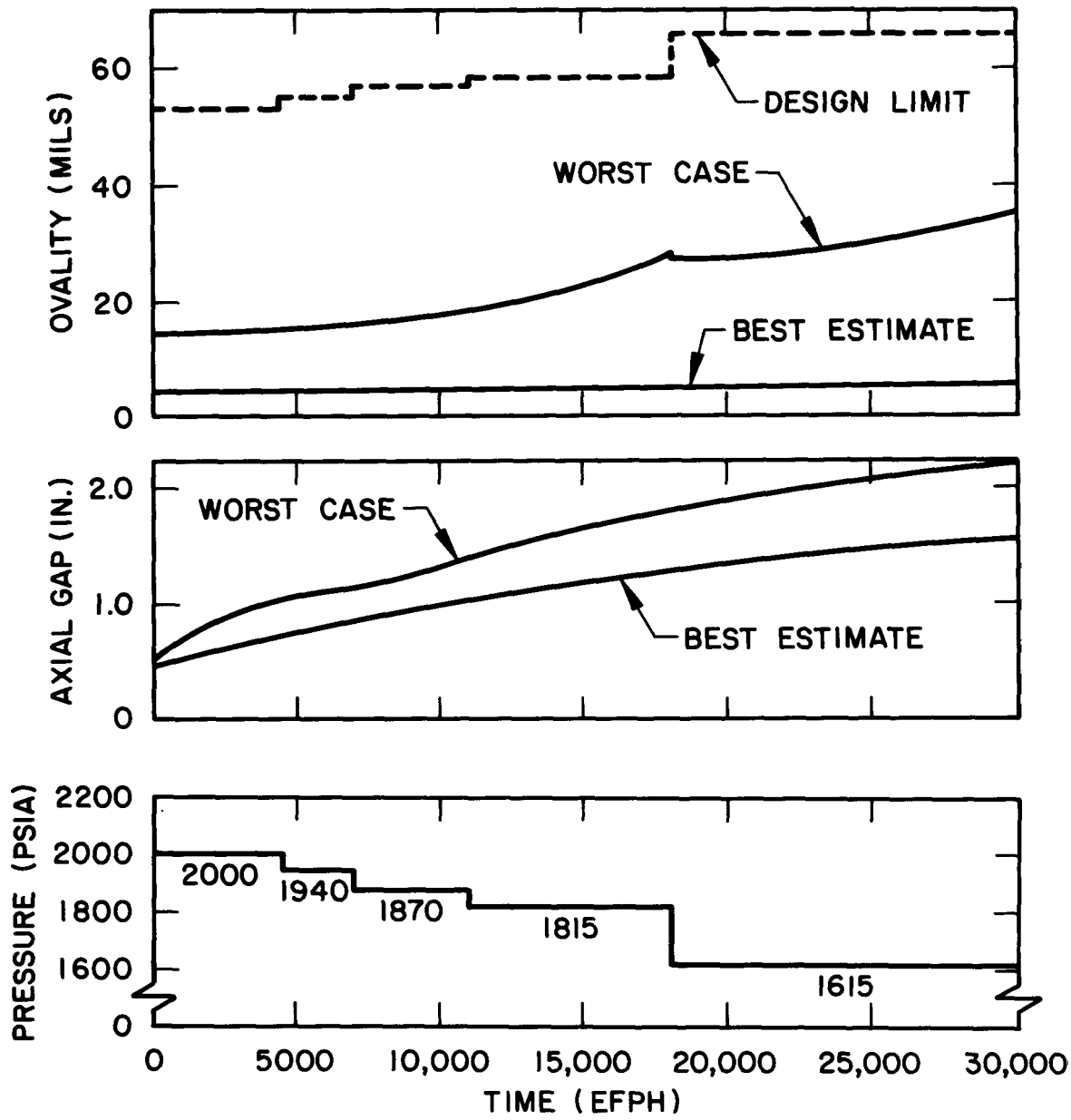

Figure 15. Standard Blanket Fuel Rod Plenum Ovalities

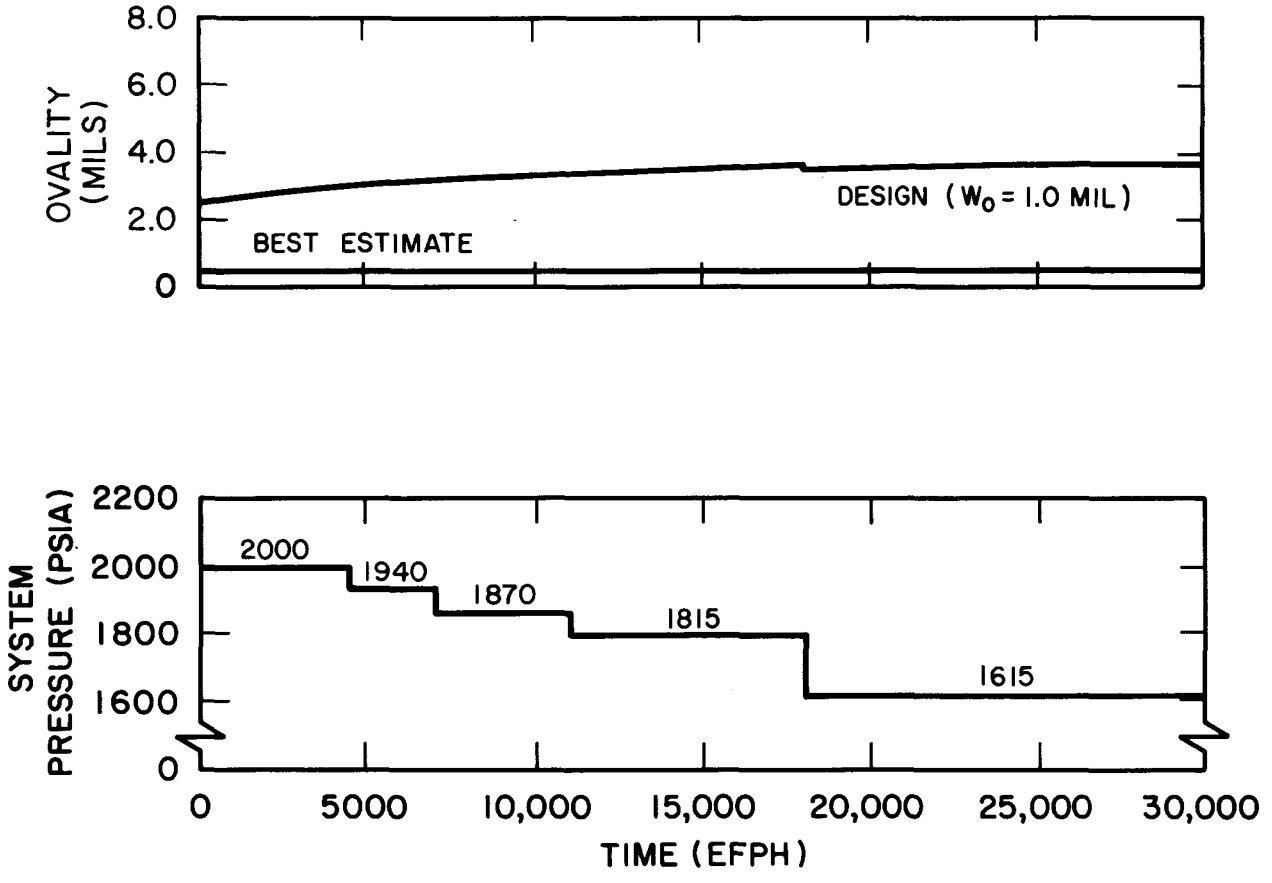

Figure 16. Seed Fuel Rod Plenum Ovalities

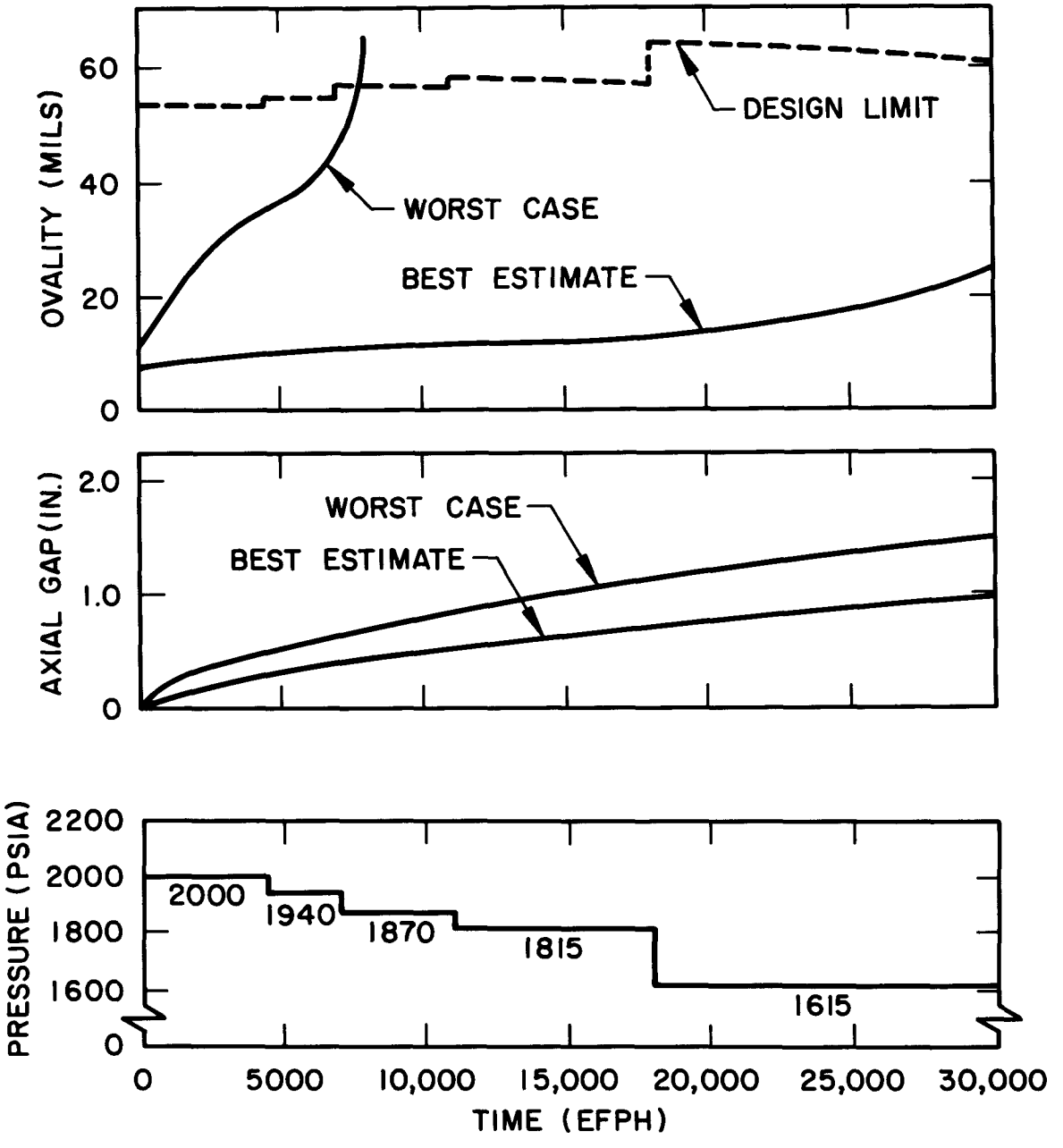

Figure 17. Standard Blanket Fuel Rod In-Stack Axial Gap Ovalities

Coefficients A(i) were derived from the relationship:

$$A(i) = (\ln w/w_0)/Z(i),$$

where:

w_0 = best estimate ovality at time of interest

$Z(i)$ = coded value (generally 2-sigma value) for variable i.

Coefficients B(1,i) were derived from the relationship:

$$B(1,i) = [\ln w/w_0 - A(1)\ Z(1) - A(i)\ Z(i)]/Z(1)\ Z(i),$$

where:

w_0 = best estimate ovality at time of interest

w = ACCEPT-calculated ovality for coded axial gap length equal to Z(1) and coded value for the ith parameter equal to Z(i)

$A(1)$ = linear coefficient for axial gap length

$Z(1)$ = coded axial gap length

$Z(i)$ = coded value for the ith parameter.

One ACCEPT calculation per fitting coefficient plus a best estimate analysis was required to define the response function.

Cladding ovality probability density distributions at selected times in core life were obtained from METER. These density distributions were used with the cladding collapse curve shown in Figure 18 to determine collapse probabilities as a function of core lifetime. The estimated number of fuel rods with collapsed cladding was then determined using the relationship:

$$C = P_1(P_2\ N_{STD} + P_3\ N_{PFB})\ P_4 + (P_5\ N_{STD} + P_6\ N_{PFB}),$$

where:

P_1 = probability of in-stack axial gap formation

P_2 = collapse probability for standard blanket fuel rod in-stack axial gaps

P_3 = collapse probability for power flattening blanket in-stack axial gaps

P_4 = fraction of rod length susceptible to in-stack axial gap collapse

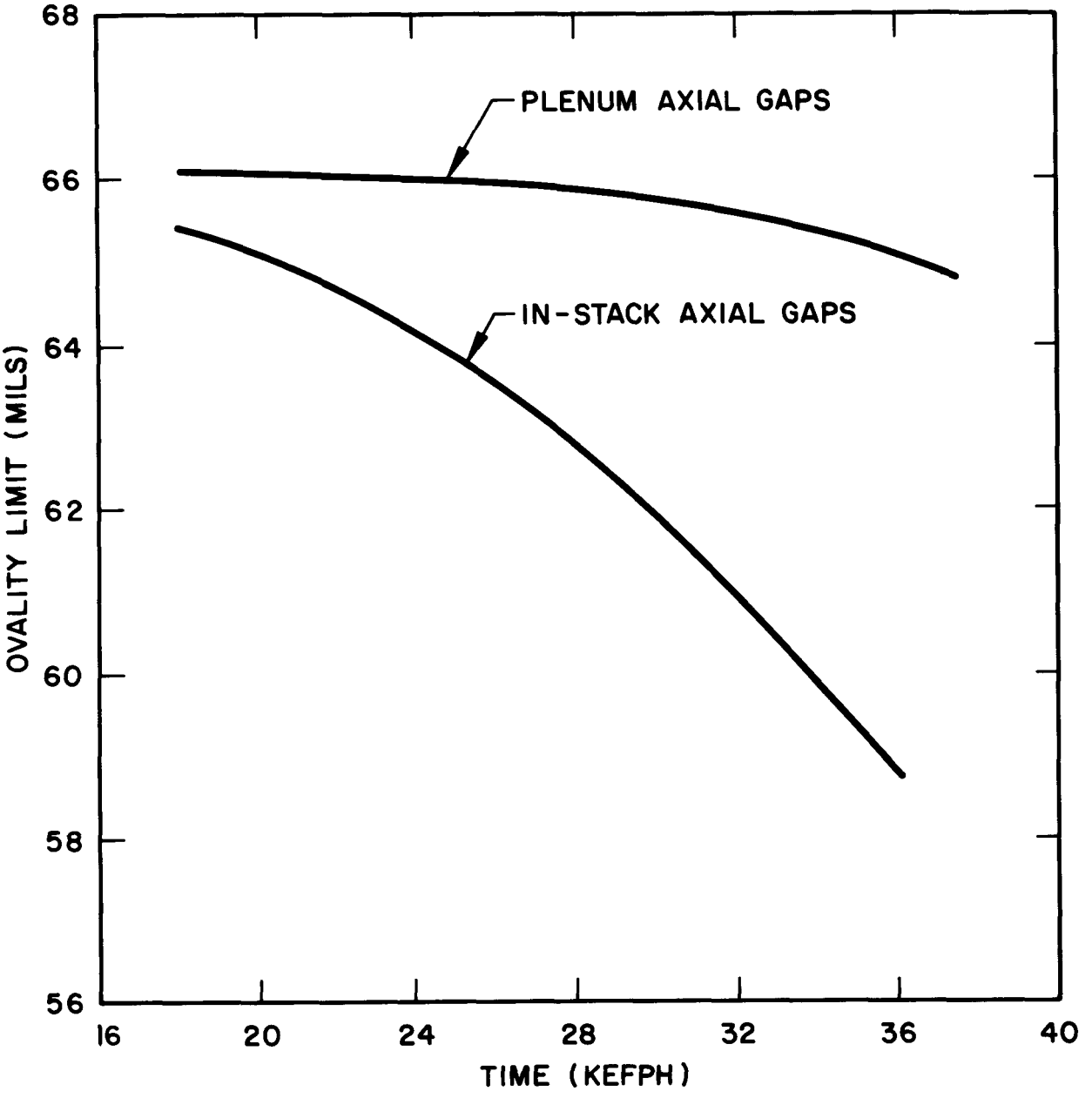

Figure 18. Standard and Power Flattening Blanket Collapse Limits

P_5 = collapse probability for standard blanket fuel rod plenum gaps

P_6 = collapse probability for power flattening blanket fuel rod plenum axial gaps

N_{STD} = number of standard blanket fuel rods (3234)

N_{PFB} = number of power flattening blanket fuel rods (3581).

Table 36 presents the predicted number of fuel rods with collapsed cladding for operation of LWBR to 30,000 EFPH.

Table 36 - Predicted Number of Fuel Rods with Collapsed Cladding

Time (EFPH)	Number of Collapsed Rods
18,000	0.02
24,000	0.08
30,000	0.25

These results indicated that gross collapse of fuel rods in LWBR was highly unlikely for operation to 30,000 EFPH.

5.14.2.3 - Grid-Induced Cladding Deformation (Dimpling)

The ACCEPT finite element computer program and a statistical fit of observed deformations for irradiation test rods were used to predict dimpling of LWBR fuel rod cladding due to grid loads. Grid-induced dimpling of the cladding was primarily a concern for seed fuel rods with freestanding cladding, where a radial gap remained between cladding and fuel pellets during lifetime. Grid-induced dimpling could also occur in the thoria regions of fuel rods with nonfreestanding cladding, where a radial gap between the cladding and fuel pellets could exist through most of core life. However, omission of the effect from spring follow calculations for rods with nonfreestanding cladding (blanket and reflector) was found to be conservative (i.e., it resulted in increased spring follow requirements).

The ACCEPT program was used to evaluate dimpling at the end (top and bottom) grid locations on seed fuel rods where accurate prediction of the effects of time, temperature, and cladding stress was needed to evaluate the impact of dimpling on accelerated wear of fuel rods with spring forces below the vibratory wear threshold. Analysis of cladding dimpling with ACCEPT involved modeling a 180-degree segment of the fuel rod cladding. A time-varying external pressure over the grid contact points was input to simulate irradiation-induced relaxation of support grid spring force. An external pressure equivalent to system pressure was also applied to the cladding segment. A time-varying internal contact surface was included in the model to account for shrinkage and swelling of fuel pellets at high-power regions of fuel rods. An internal contact surface was not included for low-power regions where pellet-cladding interaction would not occur.

The ACCEPT procedure for predicting grid-induced cladding dimpling was qualified by comparison of predictions with deformations observed on LWBR irradiation test rods. Measured dimpling was bounded by ACCEPT predictions when design properties for parameters such as cladding temperature were used. Best estimate predictions of cladding dimpling were slightly lower than best estimate values obtained from a best-fit curve of irradiation test data. The ACCEPT best estimate and design predictions for dimpling at the end grid locations on the most highly depleted seed rod in LWBR are presented in Table 37.

Table 37 - ACCEPT Predictions for Seed Grid-Induced Cladding Deformations at 30,000 EFPH

Location	Best Estimate (mils)	Design (mils)
Top Grid	0.4	1.5
Bottom Grid	0.3	1.1

Estimates of dimpling from the statistical fit of data from irradiation test rods were used for high-power regions of seed fuel rods. The best estimate and upper-bound curves used for LWBR analysis are presented in Figure 19.

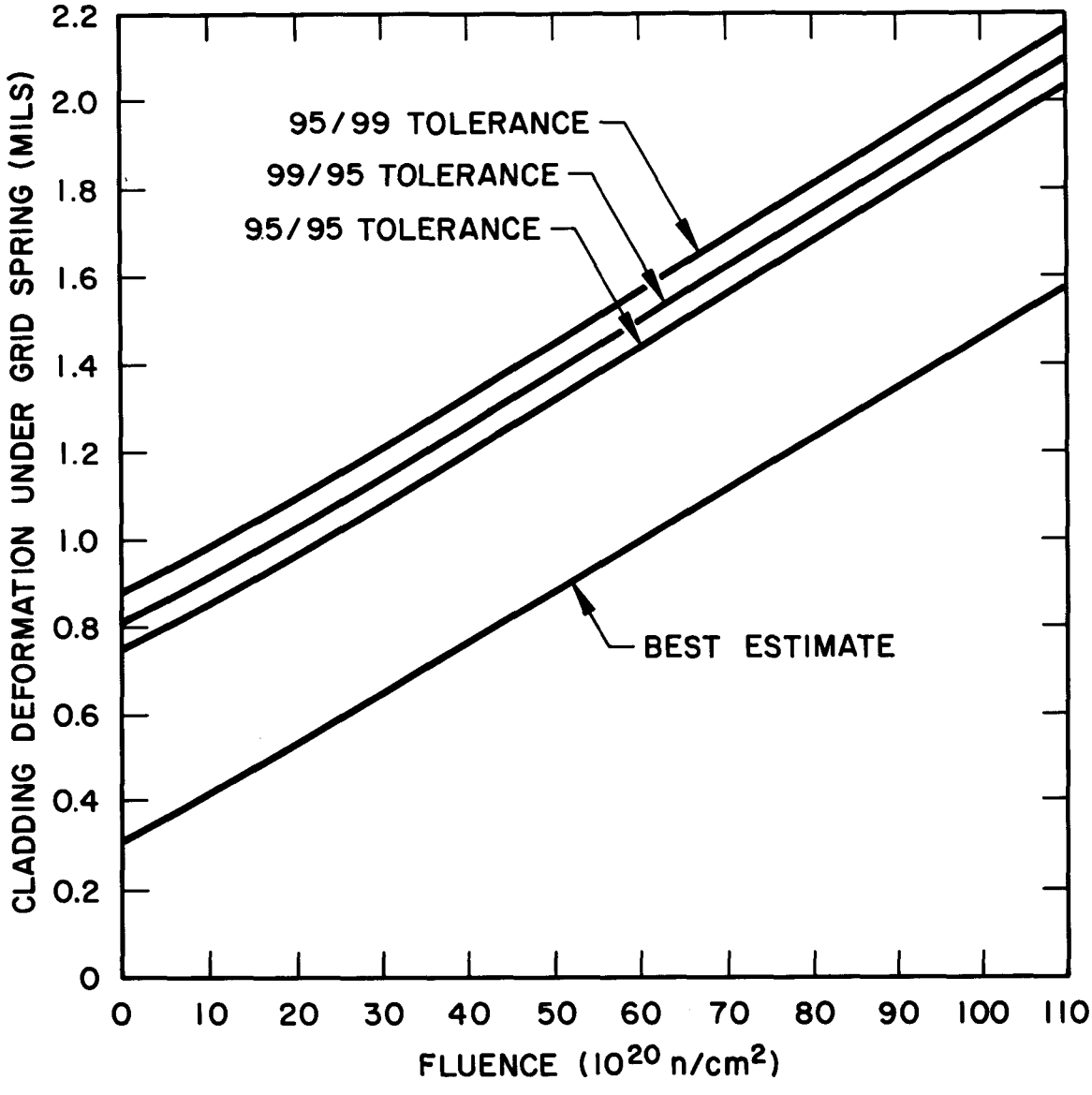

Figure 19. Curves for Grid-Induced Cladding Dimpling Based on Irradiation Test Data

Dimpling of fuel rod cladding under grid forces introduces localized cladding strains and results in loss of spring deflection. Rounding out a dimpled cladding due to pellet swelling introduces elastic tensile stress on the cladding inner surface.

Based on ACCEPT calculations, the maximum tensile plastic strain for a 1.9-mil dimple on a seed fuel rod was 0.2 percent in the thickness direction. This is well below the 2.0 percent strain limit used for LWBR fuel rods.

Based on ACCEPT predictions of local cladding deformation at the spring and dimple contact locations on a seed fuel rod, the loss in spring deflection (LSD) due to grid-induced dimpling was given by:

$$LSD = 1.15 \text{ (Dimpling)},$$

where the dimpling is calculated by ACCEPT or the Figure 19 curve. The 1.15 factor accounts for the fact that the amount of dimpling is not the same at all rod-grid contact points.

Based on elastic calculations, the stress increments associated with rounding out a 1.9-mil dimple were 19,133 psi tangential and 4181 psi axial.

5.14.2.4 - Ridging

Ridges on fuel rod cladding are a result of radial thermal expansion of fuel pellets combined with creep shrinkage of the cladding. Ridges usually form on fuel rods containing square-cornered cylindrical pellets due to pellet deformation into an hourglass shape under a large radial temperature gradient. Because they contained untapered pellets, ridging was a design concern for LWBR seed and reflector fuel rods. Ridging was not a design concern for LWBR blanket fuel rods because the pellets had 1- to 5-mil deep end tapers.

The degree of ridging in LWBR fuel rods was determined from an empirical relationship derived from analysis with DUZ-1 (Reference 66), a Bettis computer program to calculate pellet distortion, and from test data from the LWBR irradiation test program. Ridge heights were calculated using the relationship:

$$h_D = D_f \; B \; a \; (\Delta T),$$

where:

h_D = differential end expansion of a pellet (in.)

D_f = diameter of the fuel pellets (in.)

B = allowance for pellet end radial cracking [1.0 for small initial radial gap (<0.005 inch) and 2.0 for large initial radial gap (>0.010 inch)]

a = effective thermal coefficient of pellet end displacement

= 1.1×10^{-6} in/in/F

ΔT = difference in temperature at the pellet center line and surface (F).

The effective thermal coefficient of pellet end displacement (a) represents the difference between the pellet expansivity at the ends and at the midplane. The value of a is the slope of a linear plot of diametral ridge height/ pellet diameter versus the difference in temperature between the pellet center line and surface. The linear relationship was the result of calculations of free pellet distortion of various temperature distributions across the pellet.

Table 38 presents maximum expected ridge heights for LWBR seed and reflector fuel rods.

Table 38 - LWBR Fuel Rod Ridging

Rod Type	Chamfer Depth (in.)	Chamfer Length (in.)	Minimum Radial Gap (in.)	Maximum Expected Ridge (in.)	Thinning Strain Increment (%)
Seed	0.030	0.015	0.0043	0.0010	0.54
Reflector	0.000	0.000	0.0025	0.0011	0.58

Cladding thinning strain increments resulting from ridging were added to cladding thinning strains calculated in CYGRO fuel rod analysis. Appendix A2 shows the equations used to determine the strain increments due to ridging. Total thinning strain for LWBR fuel rods was limited to 2 percent.

5.14.2.5 - Grooving

Grooving was a concern for LWBR blanket fuel rods which had tapers on the pellets to prevent excessive ridging. In the absence of pellet hourglassing, cladding creep under system pressure could result in local shrinkage of the cladding into tapered regions. Data from the LWBR irradiation test program indicated that groove depths for blanket fuel rods at LWBR operating conditions could be calculated using the relationship:

$$\delta = \delta_{max} \left[1 - e^{-(F - A)/F_o}\right],$$

where:

δ = diametral groove depth

δ_{max} = maximum groove depth

A = amount of fast neutron exposure required to attain fuel-cladding gap closure

F = fluence

F_o = fluence constant which determines the rate at which groove depth progresses from zero.

Irradiation test data also indicated that the maximum groove depth (δ_{max}) was given by:

$$\delta_{max} = d_T - 0.0034 \text{ inch},$$

where:

d_T = effective (average diametral depth of two adjacent tapers) diametral taper depth.

For LWBR core performance calculations, the 0.0034-inch allowance was reduced to 0.002 inch to allow for pellet ovality and measurement uncertainity. Therefore, the maximum groove depth was taken to be:

$$\delta_{max} = d_T - 0.002 \text{ inch}.$$

For LWBR fuel rods, the neutron exposure was sufficient to cause full grooving of the cladding. The resulting fuel rod groove depths are given in Table 39.

Table 39 - LWBR Blanket Fuel Rod Groove Depths

Rod Type	Taper Depth (in.)	Groove Depth (in.)	Cladding Thinning Strain (%)
Standard	0.008	0.006	0.71
Power-Flattening	0.0076	0.0056	0.44

Cladding grooving resulted in localized cladding thinning due to axial stretching of cladding into the groove. It could result in a loss of grid spring deflection (spring follow) and rod-to-rod and rod-to-support structure clearances.

There were no specific limits for grooving of LWBR fuel rods. Strains due to grooving were added to strains from other sources (e.g., rod growth) to determine the total cladding strain for comparison with the 2 percent thinning strain limit. Losses in spring deflection, rod-to-rod structure clearance, and rod-to-support structure clearance due to grooving were included in the analysis of these phenomena.

The strain increments due to grooving were calculated using the relationships:

$$\delta\varepsilon_\theta = -(g + h)/r_f$$

and

$$\delta\varepsilon_z = \frac{2\,t\,g}{b_g^{\,2}} + \frac{\left[b_g^{\,2} + h^2\right]^{1/2} - b_g}{b_g},$$

where:

g = groove depth (relative to top of adjacent ridge)
b_g = taper length
t = cladding thickness
r_f = pellet radius
h = ridge height.

These strain increments were added to the strains at the pellet axial midplane to determine the total strain in the cladding at the groove.

5.15 - PLENUM DESIGN

A plenum volume with plenum spring was provided above the fuel stack in each rod to accommodate axial expansion and irradiation swelling of the fuel stack and to relieve internal gas pressure caused by fission gas buildup. A plenum spring was provided in all fuel rods to maintain a contiguous fuel stack and to minimize pellet motion under shock loads. Plenum design included the specification of plenum volume, spring characteristics, and plenum support sleeve dimensions.

Plenum springs were fabricated from Inconel X-750 wire. A support sleeve was inserted in the plenum region of each blanket and reflector rod to prevent cladding collapse onto the spring during operation. Seed rods required no support sleeve due to the freestanding cladding design. Support sleeves were made from seamless tubing of 348 stainless steel, and were attached to the fuel rod endclosure with a pin made from 304 stainless steel bar stock.

5.15.1 - Plenum Volume

Plenum volume in each rod type was sized to accommodate the spring and to maintain internal gas pressure below the primary system pressure, based on the predicted amount of fission gas release from the fuel. Internal pressure affects cladding strain during normal operations and is significant in the determination of coolant channel adequacy during a loss-of-coolant accident as described in Section 5.8.

Plenum lengths and void volumes in the four rod types are presented in Table 40.

5.15.2 - Support Sleeve

Support sleeves were designed to fit the cladding inside diameter for blanket and reflector rods, with a minimum diametral clearance of 0.0025 and 0.0040 inch, respectively. Sleeve length was such that an axial gap existed between the bottom of the sleeve and the top of the fuel stack. The plenum

Table 40 - Plenum Void and Sleeve Dimensions
(As-Installed at Room Temperature)

	Seed	Standard Blanket	Power Flattening Blanket	Reflector
Plenum Length (in.)	10.000 ±0.100	9.900 ±0.055	9.900 ±0.055	3.955 ±0.040
Maximum Void Volume (in^3)	0.375	1.065	0.920	0.884
Minimum Void Volume (in^3)	0.213	0.762	0.649	0.727
Sleeve Length (in.)	No Sleeve	9.510 ±0.005	9.475 ±0.005	4.030 ±0.005
Axial Gap between Sleeve and Pellet Stack	--	$0.495^{+0.030}_{-0.040}$	0.525 ±0.035	$0.230^{+0.070}_{-0.040}$

axial gap was sufficient to accommodate differential expansion and growth of the fuel and cladding, yet short enough to support the cladding against complete collapse. As described in Section 5.14, cladding ovality of 0.006 inch was expected on a best estimate basis, and 0.036 inch on a worst-case basis.

If an unexpected amount of fuel axial expansion were to close the plenum gap and exert forces on the bottom end of the sleeve, the forces would be transmitted to the sleeve pin and the top endclosure without detrimental effects on the cladding. An irradiation test of a fuel rod with an undersized plenum gap supported this conclusion.

The sleeve lengths and resulting unsupported cladding lengths for the four as-fabricated rod types are given in Table 40.

5.15.3 - Plenum Spring

Design criteria for the plenum spring are: (1) the capability of maintaining a positive force on the fuel stack throughout lifetime under all operating and shock conditions, (2) a shear stress of 70,000 psi or less, and (3) a fatigue usage factor of 0.8 or less.

LWBR spring specifications are listed in Table 41 for the four types of fuel rods. Characteristics of fabricated springs are given in Table 42 as derived from results of tests on sample populations of each type. Comparison with the allowable design range indicates that approximately 90 percent of the springs will have characteristics within the design range, with a 95 percent confidence level.

Spring characteristics and the fuel and cladding differential thermal expansion were used to calculate spring forces at beginning of life. Lifetime changes in these parameters plus worst-case stress relaxation characteristics were used to determine if the spring forces would be capable of maintaining a positive force on the pellet stack and of sustaining design internal shock loads throughout lifetime. Spring deflection was expected to change during lifetime due to fuel stack shrinkage and rod elongation. A spring relaxation of 20 percent was used in the calculations, based on in-pile tests of Inconel

Table 41 - LWBR Fuel Rod Plenum Spring Specifications

Spring Data	Seed Rods	Standard Blanket Rods	Power Flattening Blanket Rods	Reflector Rods
Total Coils	190	125	135	33
Active Coils	188	123	133	31
Coil Spacing (in.)	0.024	0.036	0.032	0.048
Wire Diameter (in.)	0.043 ±0.001	0.072 ±0.001	0.066 ±0.001	0.109 ±0.001
Mean Spring Diameter (in.)	0.207	0.361	0.332	0.527
Spring Load Rate (lb/in)	3.06 ±0.15	6.96 ±0.35	5.85 ±0.29	46.8 ±2.3
Nominal Free Length (in.)	12.62	13.41	13.40	5.10
Installed Length (in.)*	10.00 ±0.01	10.00 ±0.01	10.00 ±0.01	3.955 ±0.01
Installed Load (lb)*	8.03 ±0.40	23.8 ±1.2	19.9 ±1.0	53.6 ±2.7

*At room temperature.

Table 42 - Typical Characteristics of As-Built Springs

Spring Type	Category Tested	Number of Samples Tested	Mean	95/90 Statistical Tolerance Interval	Allowable Design Range
Seed	Installed Load (lb)	30	8.17	7.96 to 8.38	7.63 to 8.43
	Spring Rate (lb/in)	30	3.03	2.92 to 3.14	2.91 to 3.21
	Wire Diameter (in.)	30	0.0425	0.0414 to 0.0436	0.042 to 0.044
Standard Blanket	Installed Load (lb)	15	24.3	23.68 to 24.92	22.6 to 25.0
	Spring Rate (lb/in)	15	6.83	6.61 to 7.05	6.61 to 7.31
	Wire Diameter (in.)	15	0.0713	0.0702 to 0.0724	0.071 to 0.073
Power Flattening Blanket	Installed Load (lb)	15	20.2	19.58 to 20.82	18.9 to 20.9
	Spring Rate (lb/in)	15	5.77	5.55 to 5.99	5.56 to 6.14
	Wire Diameter (in.)	15	0.0656	0.0643 to 0.0669	0.065 to 0.067
Reflector	Installed Load (lb)	38	53.5	51.93 to 55.07	50.9 to 56.3
	Spring Rate (lb/in)	38	47.58	46.34 to 48.82	44.5 to 49.1
	Wire Diameter (in.)	38	0.109	*	0.108 to 0.110

*Standard deviation not reported.

X-750 material and the fluence levels expected at the top of the fuel stack. Lifetime changes in spring loads are listed in Table 43 for springs in three rod types. These calculated spring loads show that positive spring forces were predicted through the extended lifetime to 30,000 EFPH. This conclusion also applies to springs in power flattening blanket rods because the loads are about 83 percent of those in standard blanket springs (Table 42).

After the springs were purchased and tested, the thoria fuel stack in blanket rods (both standard and power flattening) was increased by 0.1 inch to improve breeding by adding fertile material. This reduced the plenum length and the installed spring length accordingly. The resulting installed loads in blanket rods remained within tolerance, at 3 percent higher than the loads shown in Tables 41 and 43, and higher than the forces used in the spring tests of Table 42. The higher spring loads in blanket rods were considered beneficial to maintaining a positive load on the fuel stack and the shorter plenum length provided additional cladding support at the sleeve-fuel gap.

Capability of the plenum spring to maintain a positive force on the fuel stack during a shock load was indicated by the comparisons in Table 44. Spring forces are expressed in g-units, which is the force normalized to the mass of each fuel stack. Minimum loads were used for this comparison. As indicated, calculated spring forces at end of life (EOL) exceeded the shock load. This was a worst-case shock load resulting from check valve slam.

Also listed in Table 44 are the calculated transverse shear stresses on the springs resulting from static compressive loads. Shear stresses were within the 70,000-psi design limit. The fatigue usage factor for all types of springs was zero due to alternating stress intensities below the endurance limit of the fatigue design curve. Thus, spring design adequacy was shown for the four rod types.

Table 43 - Calculated Lifetime Spring Load Ranges

	Seed Spring Load (lb)	Standard Blanket Spring Load (lb)	Reflector Spring Load (lb)
	At Room Temperature		
BOL	7.6 to 8.4	22.6 to 25.0	50.9 to 56.3
18,000 EFPH	3.5 to 3.8	13.6 to 15.1	16.0 to 17.7
30,000 EFPH	2.5 to 2.8	10.8 to 12.0	6.9 to 7.7
	At Operating Temperature		
BOL	9.0 to 10.2	26.2 to 28.0	63.1 to 64.3
18,000 EFPH	4.3 to 5.5	16.3 to 18.0	24.5 to 25.7
30,000 EFPH	3.3 to 4.5	13.2 to 14.9	14.5 to 15.6

Table 44 - Calculated Plenum Spring Conditions Over Lifetime

	Seed Rods	Standard Blanket Rods	Power Flattening Blanket Rods	Reflector Rods
Spring Force (g's)				
Design at BOL (hot)	5.0	3.1	3.0	3.0
Design at EOL (hot)	1.5	1.7	1.8	1.3
Best Estimate at EOL (hot)	2.8	2.3	2.4	1.4
Spring Force Required for Shock Load (g's)	1.4	1.0	1.3	1.3
Spring Stress, Transverse Shear (psi)*	69,100	70,000	70,000	68,500
Fatigue Use Factor	0	0	0	0

*Transverse shear stress limit is 70,000 psi for temperatures up to 800F, including a margin from the limit of 99,000 psi for Inconel Alloy X-750 springs.

SECTION 6 - FABRICATION PROBLEMS AND LESSONS LEARNED

6.1 - FABRICATION PROBLEMS AFFECTING FUEL ROD DESIGN

During fabrication of LWBR fuel rods and components, certain items caused problems which led to design modifications. The resulting fuel rod design modifications included the items in the following paragraphs.

6.1.1 - Pellet Chamfers

Chamfers were added to the pellet ends of all seed pellets and all blanket thoria pellets. Seed binary pellet chamfers were ground at a nominal angle of 45 degrees and a nominal linear dimension of 0.015 inch. All seed thoria and blanket thoria pellets were ground with 0.006-inch nominal chamfers. Reflector pellets were not chamfered because of their low-power duty.

Chamfered ends tended to reduce friction between pellet and cladding and to minimize formation of chips during rod loading. In addition to solving rod load problems, pellet chamfers permitted freer movement of pellets within the cladding, thus reducing pellet-cladding interaction.

6.1.2 - Pellet Lengths

Pellet lengths were decreased from the original design lengths due to problems with structural stability in fuel pellet manufacture. Shorter pellet lengths improved pellet acceptance rates during fabrication and pellet integrity during power operations. The longer pellets were shown in irradiation tests to crack more often due to the greater temperature gradients in the pellets.

6.1.3 - Plenum Support Sleeve Relief Holes

Four 0.070-inch holes were drilled near the upper ends of the support sleeves of blanket rods to relieve gas entrapped during insertion of the plenum components and endclosure to close off the top end of the rod.

6.2 - FABRICATION PROBLEMS AFFECTING TECHNICAL REQUIREMENTS

Technical requirements of fuel rod fabrication were established early in LWBR fuel rod design efforts on the basis of irradiation tests and out-of-pile

tests on reference and nonreference rods and components. Subsequent tests permitted modification of technical requirements in specific areas, and preproduction fabrication experience exposed the need for such modifications. The resulting changes in technical requirements are discussed in the following paragraphs.

6.2.1 - Tubing Internal Diameter Surface Borescope

Small elongated surface depressions up to 0.200-inch long and 0.005-inch deep were observed on the tubing inside diameter surface after destructive evaluation of preproduction fuel rods. Investigation of the cause of these defects identified that they occurred at the vendor's plant during tube fabrication. The defects were probably caused by chips on the tube-reducing mandrel, which were imbedded on the surface and subsequently removed during pickling. Visual inspection standards were established based on the destructive evaluation of several tubes having these defects. An automated borescope inspection to detect the presence of such internal surface defects was developed in the fuel rod fabrication process prior to first blanket rod end welding to cull out any tubes with this type defect. Borescope inspection of tube interior surfaces rejected approximately 0.5 percent of blanket tubes for pitting or depressions on the inside diameter surface.

The borescope was also used to inspect tubing for foreign material on inside surfaces. Approximately 256 reflector tube assemblies, processed prior to initiation of borescope inspection, were inspected by passing the borescope into the open end of the assembly. Approximately 160 of these assemblies contained detectable foreign material. Forty of the 160 assemblies were reclaimed by removing the endclosure and cleaning out the tubes.

As a result of this borescope detection of foreign material in tubing, the tube cleaning procedure was changed to require an alcohol mechanical swabbing to be repeated until all traces of black material were removed. Subsequent borescope inspections showed this to be effective.

6.2.2 - Pellet Edge Cracks

The presence of initial cracks in a pellet caused technical concern because of: (1) the potential for pellet chipping during loading and operation, (2) the effect of cracks on structural integrity of the pellet, and (3) the potential for inducing local ridges or bumps on blanket cladding such as observed on some irradiation test rods. Push tests and rod loading tests of pellets indicated that this cracked condition of fabricated blanket binary and thoria pellets did not result in an increase in pellet chipping during loading, push testing, or autoclave corrosion testing.

Therefore, pellet edge cracks were accepted within certain limits of size and frequency. These limits continued to assure that fabricated pellets were structurally sound.

6.2.3 - Pellet Structure

Modifications to pellet structure characteristics of grain size and granular segregation resulted from analysis of fuel densification during power operations. The fine grain size limit was relaxed to ASTM 10.5 to 13, depending on the fuel type and location within the pellet, based on limits for allowable densification and fission gas release. Additional specifications related to averages and limitations on the volume fraction of fine-grained material.

Granular segregation is a type of porosity distribution in fuel pellets. Excessive granular segregation was restricted by sample inspection and comparison to microstructure standards. These high-porosity regions represented undesirable zones of mechanical weakness and decreased thermal conductivity.

Inspection standards for grain size and granular segregation were based on analysis and irradiation test data and their effects on pellet structural integrity and in-reactor densification.

6.2.4 - In-Motion Radiography

In-motion radiography was used to detect pellet chips and voids in the fabricated fuel rods as discussed in Section 5.13 and to evaluate overall pellet integrity. Only 12 percent of the reflector rods were accepted within the original inspection standards for size, orientation, location, and frequency of chips and voids. This acceptance rate was sufficient to supply rods for high-duty locations in reflector modules. A relaxation of inspection standards resulted in acceptance of the remaining 88 percent of reflector rods with the stipulation that they be assembled into selected low-power regions of the modules.

As a result of this experience with reflector fuel integrity, and following some tests on various loading procedures (Reference 67), pellet loading was changed from vertical to horizontal and from mechanical to manual insertion in seed and blanket rods.

Seed rods were inspected by in-motion radiography at six orientations 30 degrees apart. No chips were permitted for acceptance, except for one chip located in the lower thoria region of a rod. Relaxation of chip and void sizes, acceptance of chips inside the plenum spring and of pellet dust, and establishment of spring coil distribution acceptance conditions resulted in conditional acceptance of some seed rods for assembly into lower power locations.

Standard blanket rods were inspected at nine orientations 20 degrees apart. Inspection standards resulted in an 85 percent acceptance rate. The major cause of rejection was pellet chips and voids. The size, number, and locations of chips and voids determined the allowable location of a rod in blanket modules.

In-motion radiographic inspection of power flattening blanket rods was similar to that of the standard blanket rods. Nine views were inspected, and the major causes of rejection were pellet chips and voids; the number of pellets lacking tapers was also significant. However, an 88 percent acceptance rate was achieved.

Untapered pellets, or pellets with taper depth less than the 0.001 inch minimum, were found in some fabricated standard blanket and power flattening blanket rods. Tapers were measured from the radiographs using a microdensitometer. Measurements were confirmed by unloading three rods and physically measuring 13 pellets reported as untapered from radiographic inspection. Of the blanket rods containing detected untapered pellets, 52 standard blanket and 161 power flattening blanket rods were conditionally accepted for selective placement at lower power locations in the blanket modules. These represented 1 and 3 percent of the number of rods loaded, respectively.

6.2.5 - Low-Density Reflector Fuel Pellets

Approximately 26 blends of reflector pellets had densities less than 96 percent average density. These blends were processed from essentially three lots of thoria powder. Lots processed subsequent to the three lots showed no similar conditions, and the cause of the lowered densities could not be determined. Although these blends met the then-specified density requirements, it was deemed technically undesirable to load reflector rods with pellets having densities less than 96 percent average density for unrestricted location in the assembly.

In order to find a way to use the already fabricated pellets, the following scheme was developed. Rods loaded with reflector pellets having an average density less than 95.5 percent were rejected. Rods loaded with reflector pellets having an average density between 95.5 and 96.0 percent were assembled in selected regions of the core where acceptable performance could be shown. The balance of the blends of pellets having an average density between 95.5 and 96.0 percent were combined with blends having densities greater than 96 percent to ensure an average blend density of 96 percent or greater.

6.2.6 - Coring in Reflector Pellets

Pellet coring refers to large central voids in the fabricated pellet, with a high pore frequency, and is usually associated with fine central grain size. The condition was first noted in standard blanket thoria pellets and

was shown to be caused by incomplete removal of the binder prior to pellet sintering. Coring occurred only in thoria pellets due to lower pretreatment temperature (800 versus 1700F for binary pellets).

Coring was recognized after reflector fuel rods were assembled in modules, but before other types of rods were fabricated. An increase in thoria pellet sintering temperature and full inspection of fuel pellets for other than reflector rods eliminated cored pellets in seed and blanket rods. The search for suspected cored reflector pellets depended on inspection of retainer samples and review of fuel blend densities.

Radiographic inspection of retainer samples showed three reflector fuel blends with cored pellets and four blends with indications of low-density centers, termed shadowed pellets. Evaluation of density data resulted in five fuel rods being removed from the modules, then radiographed.

On the basis of those studies, three of the five inspected rods were removed from high-power locations and replaced with rods containing no cored pellets. All other rods containing suspect fuel blends were in low-power locations where cored or shadowed conditions would not be detrimental to core performance.

6.2.7 - Fuel Rod Straightness

The original fuel rod straightness criteria resulted in an acceptance rate of 90 percent for reflector fuel rods. Modification of the criteria on a grid level basis improved the acceptance rate to 91.5 percent, but the major improvement was a conditional acceptance for selective assembly into modules. Approximately 6.8 percent additional reflector rods were accepted on this basis.

Modified requirements on rod straightness also resulted in conditional acceptance of 1 percent of seed rods, 3 percent of standard blanket rods, and 1.5 percent of power flattening blanket rods. All such rods accepted conditionally were selectively placed in low-duty locations in their respective modules.

6.3 - LESSONS LEARNED

The LWBR fuel system was the first of its kind to use a ^{233}U and thoria-based fuel system to demonstrate breeding. As such, many lessons were learned which may be useful in future projects. Some of the more significant lessons learned are listed below:

1. High-density fuel pellets alleviate many fuel rod performance concerns. Among them are the opening of axial gaps in the fuel stack and subsequent cladding deformation, pellet cracking or coring, and internal temperature instability caused by interactions between pellet diameter and fuel-cladding gap conductance.
2. High-quality fuel pellets can be manufactured to 0.0005-inch tolerance on diameter, and can include geometric requirements such as end dishes and edge chamfers and tapers.
3. Resintering when necessary is worth the extra manufacturing time to provide a structurally stable fuel pellet.
4. Pellet length to diameter ratio should be less than 2.5 to provide satisfactory uniform compaction.
5. Horizontal loading of pellets into tubing is preferred to vertical loading in the interest of pellet integrity.
6. Use of a friction-grip endclosure eliminates tack welding and provides a more uniform and defect-free weld joint.

Other procedures that aided in fuel rod fabrication are described in References 13 and 67.

(Intentionally Blank)

SECTION 7 - SUMMARY AND CONCLUSIONS

Fuel rods for the LWBR core were designed to meet the objectives of ensuring fuel breeding and maintaining failure-free fuel rod operation. To achieve desired breeding levels, poison control rods were replaced with movable fuel modules and spacial fuel zoning, the mass of nonfuel components such as Zircaloy cladding and support grids was minimized, and rod-to-rod pitch was as tight as practical while maintaining a coolable geometry. These challenges presented engineering and fabrication problems that required solutions unique to the LWBR fuel rod design.

An extensive analytical program for fuel rod design was supported by irradiation tests of reference and nonreference fuel rods and by out-of-pile tests of fuel rod components and simulated fuel rods, both singularly and in assemblies. In the development stage, use was made of experimental and power reactor data from the evolving fuel systems of the reactor industry, both in this country, as represented by the Electric Power Research Institute (EPRI), and internationally, as represented by Canadian and European experience. Concerns such as fuel densification, cladding deformation, pellet-cladding interaction, rod elongation and bow, accelerated corrosion of Zircaloy, and enhanced fission gas release entered into the performance assessments of the fuel rod design.

Fuel rod fabrication was gaged to meet the stringent technical requirements derived from the design concerns. From an innovative forging process used in tubing reduction to an improved rod endclosure design that simplified welding and increased fatigue life, each step of fuel rod fabrication and inspection was directed toward complete fuel rod integrity.

The LWBR fuel system was the first to use ^{233}U and thoria-based fuel to demonstrate breeding. It was necessary to develop irradiated fuel properties and to determine susceptibility of the assembled fuel rod to the problems experienced by UO_2 fuel systems in the industry. Unique performance requirements were imposed by the use of movable fuel assemblies for reactivity

control and the tight rod-to-rod clearances and rod component dimension tolerances required to enable fuel breeding. This report describes the specific fuel rod design considerations and the methods used to assess those concerns for LWBR fuel rods.

Close follow of reactor operations using an extensive data acquisition system enabled the continuous monitoring and reevaluation of fuel rod performance throughout lifetime. As a result, the design lifetime of 18,000 EFPH was extended with confidence to 29,047 EFPH actual lifetime, with reductions in maximum power, system pressure, and coolant temperature.

End-of-life examinations of fuel rods indicate no breach of cladding, preservation of fuel pellet integrity, and acceptable fuel rod performance as expected. Results of post-irradiation examination of selected fuel rods are reported in References 17 and 68.

SECTION 8 - ACKNOWLEDGMENTS

Analyses and fuel element performance assessments were performed under the supervision of R. A. Frederickson, I. Goldberg, P. L. Pfennigwerth, and M. J. Schneider. The performance of LWBR fuel elements was in large part due to analyses and design supervised by I. Goldberg. The following individuals contributed to the technical assessments listed below:

E. B. Barger	-	Cladding wear, out-of-pile tests
B. R. Beaudoin	-	Programming of physics data and fuel temperature model
W. R. Campbell	-	LEP, PCI, SCC, fuel depletion, up-power transient analysis
T. L. Chao	-	Rod bow
R. M. Clark	-	Module growth and module bow
J. C. Clayton	-	Cladding corrosion and hydrogen pickup, defected fuel rod operation, waterlogging
P. J. Crescimanno	-	SCC, cladding properties
E. Duncombe	-	LEP, CYGRO
L. B. Freeman	-	Reactor physics
C. S. Galtz	-	Cladding wear, grid spring follow, rod-to-structure proximity
J. F. Giovengo	-	CYGRO qualification, LOCA, cladding stresses, fission gas release, rod growth, axial gaps
D. A. Gorscak	-	Cladding deformation over axial gaps
H. C. Hecker, Jr.	-	Reactor physics
B. Z. Hyatt	-	AM-350 stainless steel corrosion, hydrogen pickup, and grid spring follow
K. L. Keller	-	Cladding wear, grid spring follow, SCC of Alloy X-750
E. A. McCabe	-	Plenum hardware, waterlogging
P. L. Pfennigwerth	-	Cladding corrosion and hydrogen pickup, cladding deformation over axial gaps, fuel densification
K. D. Richardson	-	Module length and module bow
I. A. Selsley	-	Cladding deformation over axial gaps
B. C. Smith	-	AM-350 corrosion and hydrogen pickup
R. M. Stackhouse	-	AM-350 hydrogen pickup
J. W. Stout	-	Thermal/hydraulic performance
B. A. Todd	-	PCI, SCC, cladding wear, overpower transients
H. J. Willard, Jr.	-	Zircaloy growth
C. E. Zucker	-	Depletion, fluence, rod bow

Reviews were provided by W. E. Franzen, W. J. Babyak, C. A. Pruss, I. Goldberg, P. L. Pfennigwerth, and R. A. Frederickson. Final editing was provided by D. M. Bailey.

(Intentionally Blank)

SECTION 9 - REFERENCES

1. D. R. Connors, S. Milani, J. A. Fest, and R. Atherton, "Design of the Shippingport Light Water Breeder Reactor," WAPD-TM-1208, January 1979.

2. The Shippingport Pressurized Water Reactor, Addison-Wesley Publishing Co., Inc., Reading, Mass., 1958.

3. B. C. Smith and W. R. Campbell, "Light Water Breeder Reactor Fuel Element Performance Characteristics for Extending Core Lifetime," WAPD-TM-1603, October 1987.

4. J. Belle and R. M. Berman, editors, "Thorium Dioxide: Properties and Nuclear Applications," DOE/NE-0060, Government Printing Office, Washington, D.C., 1984.

5. H. R. Warner, "Release of Fission Gases from Oxide Fuels," WAPD-TM-805, July 1969.

6. I. Goldberg, et al, "Fission Gas Release from ThO_2 and ThO_2-UO_2 Fuels (LWBR Development Program)," WAPD-TM-1350, August 1978.

7. J. M. Markowitz and J. C. Clayton, "Corrosion of Oxide Nuclear Fuels in High Temperature Water," WAPD-TM-909, February 1970.

8. J. C. Clayton, "In-Pile and Out-of-Pile Corrosion Behavior of Thoria-Urania Pellets," WAPD-TM-1548, January 1987.

9. J. C. Clayton, "Cladding Corrosion and Hydriding in Irradiated Defected Zircaloy Fuel Rods," WAPD-TM-1393, August 1985.

10. J. C. Clayton, "Internal Hydriding in Irradiated Defected Zircaloy Fuel Rods - A Review," WAPD-TM-1604, September 1987.

11. K. D. Richardson, "Summary of the Fuel Rod Support System (Grids) Design for LWBR," WAPD-TM-1331, February 1979.

12. C. R. Woods, editor, "Properties of Zircaloy-4 Tubing," WAPD-TM-585, December 1966.

13. John H. Eyler, "Development and Control of the Process for the Manufacture of Zircaloy-4 Tubing for LWBR Fuel Rods," WAPD-TM-1289, January 1981.

14. J. B. Newman, J. F. Giovengo, L. P. Comden, "The CYGRO-4 Fuel Rod Analysis Computer Program," WAPD-TM-1300, July 1977.

15. G. P. Marino and R. L. Fischer, "Corrosion of Zircaloy-4 Tubing in 680°F Water," WAPD-TM-1322, December 1978.

16. J. C. Clayton, "Out-of-Pile Accelerated Hydriding of Zircaloy Fasteners," WAPD-TM-1426, October 1979.

17. K. D. Richardson, "End-of-Life Destructive Examination of LWBR Fuel Rods," WAPD-TM-1606, October 1987.

18. J. W. Stout, "Fuel-Rod/Support-Grid Scratching and Friction," WAPD-TM-1164, October 1979.

19. I. Goldberg, L. L. Lynn, and D. D. Sphar, "FIGRO - A FORTRAN-IV Digital Computer Program for the Analysis of Fuel Swelling and Calculation of Temperature in Bulk-Oxide Cylindrical Fuel Elements," WAPD-TM-618, December 1966.

20. L. A. Waldman, L. L. Lynn, and I. Goldberg, "FIGRO (Addendum) - A CDC-6600 Computer Program for the Analysis of Fuel Swelling and Calculation of Temperature in Bulk-Oxide Cylindrical Fuel Elements," WAPD-TM-618, Addendum I, October 1967.

21. I. Goldberg and L. L. Lynn, "FIGRO (Addendum II) - A CDC-6600 Computer Program for the Analysis of Fuel Swelling and Calculation of Temperature in Bulk-Oxide Cylindrical Fuel Elements," WAPD-TM-618, Addendum II, April 1970.

22. I. Goldberg, "A Procedure for Calculation of Steady-State Temperature in Zircaloy-Clad, Bulk-Oxide Fuel Elements Using the FIGRO Computer Program," WAPD-TM-757, November 1969.

23. F. A. Nichols, "Behavior of Gaseous Fission Products in Oxide Fuel Elements," WAPD-TM-570, October 1966.

24. D. N. Hutula, B. E. Wiancko, "ACCEPT: A Three-Dimensional Finite Element Program for Large Deformation Elastic-Plastic-Creep Analysis of Pressurized Tubes," WAPD-TM-1383, March 1980.

25. EPRI Journal pp 63-64, March 1987.

26. W. J. Penn, R. K. Lo, and J. C. Wood, "CANDU Fuel-Power Ramp Performance Criteria," Nuclear Technology 34, pp. 249-268, July 1977.

27. N. W. Polan and R. P. Tucker, "The Susceptibility of Unirradiated Recrystallized Zircaloy-4 Tubing to Stress Corrosion Cracking," WAPD-TM-1313, December 1977.

28. R. P. Tucker, P. H. Kreyns, and J. J. Kearns, "The Effects of Internal Surface Flaws, Iodine Concentration and Temperature on Stress Corrosion Cracking Behavior of Zircaloy-4 Tubing," WAPD-TM-1248, February 1976.

29. J. G. Weinberg, "Iodine Stress Corrosion Cracking of Zircaloy-4 Tubing," WAPD-TM-1048, February, 1974.

30. H. S. Rosenbaum, "The Interaction of Iodine with Zircaloy-2," Electrochem. Tech. 4, pp. 153-156, Mar-Apr 1966.

31. J. C. Clayton, "Fission-Product Iodine in Thoria/Urania Oxides," WAPD-TM-1148, February 1979.

32. D. M. Ivak and L. A. Waldman, "Iodine and Cesium in Oxide Fuel Pellets and Zircaloy-4 Cladding of Irradiated Fuel Rods," WAPD-TM-1394, March 1979.

33. P. J. Crescimanno, W. R. Campbell, and I. Goldberg, "A Fracture Mechanics Model for Iodine Stress Corrosion Crack Propagation in Zircaloy Tubing," ASTM STP 821, pp. 150-169, American Society for Testing and Materials, Philadelphia, PA, 1984.

34. S. Djurle, "The Studsvik Over-Ramp Project," EPRI NP-3007, Electric Power Research Institute, April 1983.

35. D. Cubicciotti, R. L. Jones, and B. C. Syrett, "Stress Corrosion Cracking of Zircaloys," EPRI NP-1329, March 1980.

36. J. F. Yerman, "Effect of Fuel Chips on Cladding Stress in Zircaloy Clad Oxide Fuel Rods," WAPD-TM-1324, November 1978.

37. S. Borresen, et al, "Nuclear Fuel Performance Evaluation," EPRI NP-409, June 1977.

38. W. J. O'Donnell, "Fracture of Cylindrical Fuel Rod Cladding Due to Plastic Instability," WAPD-TM-651, April 1967.

39. P. J. Crescimanno, "High Strain Rate Tensile Tests of Zircaloy at 550°F," WAPD-TM-1263, February 1976.

40. G. F. Rieger and D. Lee, "Strength and Ductility of Neutron Irradiated and Textured Zircaloy-2," Zirconium in Nuclear Applications, ASTM STP 551, American Society for Testing and Materials, Philadelphia, PA, pp. 355-369, August 1974.

41. E. Duncombe, "The Relationship Between Failure Strains in Burst Tests on Zircaloy Tubing and Wall Thickness Eccentricity," WAPD-TM-1104, January 1973.

42. J. C. Clayton, "Sources of Internal Hydriding in Unirradiated Thoria-Fueled Zircaloy Rods," WAPD-TM-1272, February 1979.

43. J. C. Clayton, "Corrosion and Hydriding of Irradiated Zircaloy Fuel Rod Cladding," WAPD-TM-1440, September 1982.

44. J. C. Clayton and R. L. Fischer, "Corrosion and Hydriding of Zircaloy Fuel Rod Cladding in 633K Water and Reactor Environments," pp. 3.1-3.16, Proc. ANS Topical Meeting on Light Water Reactor Fuel Performance, Orlando, Florida, April 1985.

45. E. Hillner, "Corrosion and Hydriding Performance Evaluation of Three Zircaloy-2 Clad Fuel Assemblies After Continuous Exposure in PWR Cores 1 and 2 at Shippingport, PA," WAPD-TM-1412, January 1980.

46. E. Hillner, "Long-Term In-Reactor Corrosion and Hydriding of Zircaloy-2 Tubing," in "Zirconium in the Nuclear Industry: Fifth Conference," ASTM-STP 754, pp. 450-478, 1982.

47. J. Boulton, "Current Knowledge of Zirconium Alloys for Reactor Usage," AECL-3365, June 1969.

48. F. Garzarolli, R. Von Jan, and H. Stehle, "The Main Causes of Fuel Element Failure in Water-Cooled Power Reactors," Atomic Energy Review 17, pp. 31-128, 1979.

49. J. J. Urbaniak, "ROBOT - A Computer Program to Solve the Bowing Problem in Rod-Type Fuel Elements (LWBR Development Program)," WAPD-TM-847, July 1969.

50. I. Goldberg, L. A. Waldman, J. F. Giovengo, W. R. Campbell, "Fission Gas Release and Grain Growth in ThO_2-UO_2 Fuel Irradiated at High Temperature," WAPD-TM-1350 Addendum, July 1979.

51. J. F. Giovengo, I. Goldberg, C. D. Sphar, "Fission Gas Release from High Burnup ThO_2 and ThO_2-UO_2 Fuels Irradiated at Low Temperature," WAPD-TM-1350, Addendum 2, May 1982.

52. I. Goldberg, J. F. Giovengo, T. L. Chao, "Evaluation of Coolable Geometry Adequacy of the LWBR Core During a Loss-of-Coolant Accident (LOCA)," WAPD-TM-1397, June 1985.

53. W. J. O'Donnell and B. F. Langer, "Fatigue Design Basis for Zircaloy Components," Nuclear Science and Engineering 20, pp. 1-12, 1964.

54. C. S. Galtz, "The Friction Grip Endclosure - A Means for Increasing the Fatigue Life of Fuel Rod End Welds," WAPD-TM-1348, March 1983.

55. J. C. Clayton, "Out-of-Pile Nickel Alloy-Induced Accelerated Hydriding of Zircaloy Fasteners," in "Zirconium in the Nuclear Industry: Sixth Conference," ASTM-STP 824, pp. 572-591, 1984.

56. D. H. Locke, "The Behavior of Defective Reactor Fuel," Nucl. Eng. Des. 21, pp. 318-330, 1972.

57. H. Plitz, "Failed Fuel Pin Performance in Fast Metal-Cooled Reactors," Nucl. Tech. 37, pp. 48-58, 1978.

58. D. H. Locke, "Mechanisms of Deterioration of Defected LWR Fuel," IWGFPT-6, 101-103 (1980); IAEA Specialists Meeting on Behavior of Defected Zirconium Alloy Clad Ceramic Fuel in Water Cooled Reactors, Chalk River, Ontario, Canada, September 17-20, 1979.

59. H. J. Cramer, R. H. Rigg, and J. W. Stout, "Fuel Rod-Grid Interaction Wear: In-Reactor Tests," WAPD-TM-1347, November 1979.

60. C. S. Galtz, R. M. Stackhouse, and W. R. Campbell, "Flow-Induced Vibrational Wear Behavior of Zircaloy Clad Simulated Fuel Rods in a Grid Support System," WAPD-TM-1250, March 1987.

61. B. R. Beaudoin, "Loading Assurance Methods Used in the Manufacture of the Light Water Breeder Reactor (LWBR)," WAPD-TM-1315, September 1987.

62. B. R. Beaudoin, "Monte Carlo Simulation Using the METER System with Applications Related to LWBR (LWBR Development Program)," WAPD-TM-1288, February 1977.

63. I. A. Selsley, "Ex-Reactor Deformation of Externally Pressurized Short Lengths of Fuel Rod Cladding (LWBR Development Program)," WAPD-TM-1404, May 1979.

64. I. A. Selsley, "Thermal Tests to Investigate Stability of Externally Pressurized Zircaloy-4 Tubing Over Axial Gaps (LWBR Development Program)," WAPD-TM-1509, July 1982.

65. D. A. Gorscak and P. L. Pfennigwerth, "Analysis of Cladding Deformation Over Plenum Axial Gaps in Zircaloy Clad Fuel Rods," WAPD-TM-1339, December 1982.

66. D. S. Griffin, R. B. Kellogg, W. D. Peterson, and A. E. Sumner, Jr., "DUZ-1: A Program for Solving Axisymmetric and Plane Elasticity Problems on the Philco-2000," WAPD-TM-555, November 1965.

67. V. V. DeGeorge and I. Goldberg, editors, "The Fabrication and Loading of Fuel Rods for the Light Water Breeder Reactor," WAPD-TM-1278, March 1986.

68. D. A. Gorscak, "End-of-Life Nondestructive Examination of LWBR Fuel Rods," WAPD-TM-1605, October 1987.

APPENDIX A1 - DERIVATIONS OF EQUATIONS FOR CLADDING WEAR DEPTH

Separate formulas are used for vibrational wear depending on long-term motion of the fuel rod relative to the grid contact location. For fuel rods which have an insignificant irradiation growth relative to grid support levels, the stationary wear spot formula applies (from Section A1.1 below). For rods which have significant growth, the moving wear spot formula (Section A1.2) applies. For both stationary and moving wear spot, the procedures for overlay wear (Section A1.3) and for the effect of grid dimple width (Section A1.4) are applicable.

A1.1 - VIBRATIONAL WEAR AT A STATIONARY WEAR SPOT

Consider the formation by vibrational wear of a wear spot in the cladding at a location which is stationary with respect to the grid dimples:

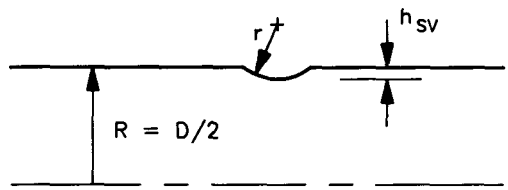

Axial Section Through Wear Spot

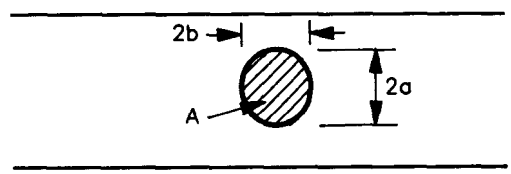

Plan View of Wear Spot $[h_{sv} \leq (h_{sv})_{cyl}]$.

For wear spots of a depth equal to or less than $(h_{sv})_{cyl}$, where $(h_{sv})_{cyl}$ is the depth at which the width of the wear spot (2a) becomes equal

to the width of the cylindrical section of the grid dimples, the shape of the wear spot will be approximately elliptical as shown in the above plan view sketch. The amount of material (dV) removed from the wear spot due to a differential increase (dh_{sv}) in the depth of the spot is:

$$dV \approx A dh_{sv} , \tag{A1-1}$$

where:

A = the area of the ellipse.

Since the wear depth is generally much smaller than the rod radius (R) or the dimple radius (r), the semi-axes of the ellipse can be approximated by:

$$a = \sqrt{D\ h_{sv}} \quad \text{and}$$

$$b = \sqrt{2r\ h_{sv}} , \tag{A1-2}$$

in which case the area of the ellipse is given by:

$$A = \pi\ ab$$

$$= \pi \sqrt{2rD}\ h_{sv} . \tag{A1-3}$$

Substituting Equation (A1-3) into Equation (A1-1) and integrating over the limits of 0 to h_{sv} give the volume of metal removed from a wear spot of depth (h_{sv}) as:

$$V = \pi \sqrt{rD/2}\ h_{sv}^2 . \tag{A1-4}$$

Noting that the wear volume generated during a period of operation [t (hours)] is equal to $\dot{V}t$, where $\dot{V}$ is the volumetric wear rate (mil^3/hr), Equation (A1-4) gives the wear depth developed after t hours of operation as:

$$h_{sv} = (\dot{V}t/\beta)^{1/2} , \tag{A1-5}$$

where:

$\beta = \pi \sqrt{rD/2}$.

Equation (A1-5) indicates that, for operation at a stationary wear spot with a fixed vibrational wear rate, the wear depth increases directly with the square root of the operating time. Equation (A1-5) also indicates that the wear depth at a stationary wear spot is a function of the dimple radius, varying inversely with the fourth root of the dimple radius. Hence, for a given amount of wear volume generated at a stationary wear spot, the wear depth developed at an LWBR seed rod spring is approximately 12 percent greater than that developed at a reaction dimple. (Seed grid spring and reaction dimple radii are nominally 64 and 100 mils, respectively.)

For cases in which the vibrational wear rate varies with time (as the result, for example, of a reduction in grid spring load to a value below the breakaway load, or a reduction in flow rate), the wear volume generated at a given wear spot is:

$$V = \sum \dot{V}_j \, \Delta t_j \, , \qquad \text{(A1-6)}$$

where:

$\dot{V}_j$ = the wear rate existing during the time interval Δt_j.

Therefore, substitution of Equation (A1-6) into Equation (A1-4) gives, for a variable wear rate history,

$$h_{sv} = \left(\frac{\sum \dot{V}_j \, \Delta t_j}{\beta}\right)^{1/2} \quad \text{for } h_{sv} \leq (h_{sv})_{cyl} , \qquad \text{(A1-7)}$$

where:

$(h_{sv})_{cyl}$ = the wear depth at which the width of the wear spot is equal to the width of the grid spring or dimple. For deeper wear, the procedure described in Section A1.4 can be used.

A1.2 - VIBRATIONAL WEAR AT A MOVING WEAR SPOT

If, due to fuel rod elongation effects, the cladding surface moves axially with respect to the grid dimple, the wear spot developed as a result of

vibrational wear will be in the form of an axial groove, as depicted in the following sketch:

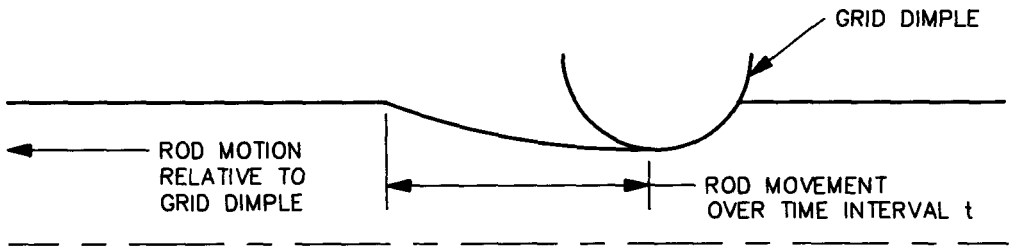

Axial Wear Groove Formed in Moving Fuel Rod Cladding

As indicated in this sketch, the groove depth tends to increase with time. However, after a sufficiently long period of time, the groove depth approaches an equilibrium value which is a function of the vibrational wear rate and the rate of motion of the fuel rod with respect to the grid dimples.

During the transient phase of the formation of the wear groove (i.e., before the equilibrium depth has been reached), the total amount of wear product (dV) removed during a differential time interval (dt) can be considered to consist of two components, dV_x and dV_h, as shown in the following sketch, which is drawn from the viewpoint of an observer stationed on the cladding:

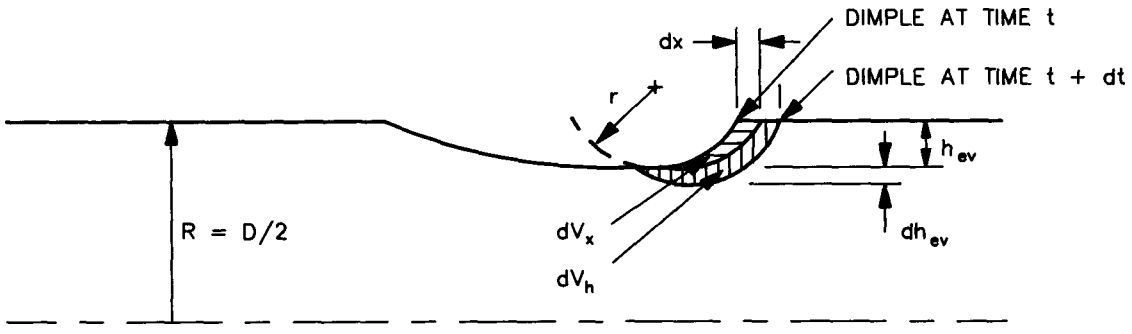

The Volumetric Components of Wear (dV_x and dV_h)

The volumetric component of wear (V_x) is that occurring over the axial increment of motion (dx) executed in the time interval (dt). The volumetric component of wear (dV_h) is that occurring in the depth direction over an increment (dh_{ev}) executed in the same time interval. These component volumes are given by:

$$dV_x = A_x dx$$

$$dV_h = A_h dh_{ev} \quad , \tag{A1-8}$$

where:

A_x, A_h = the projected areas of the wear contact area between the cladding and the dimple in the x and h directions, respectively.

The total volume of the wear product is the sum of the two volumetric wear components, so that, by Equation (A1-8), the total wear rate is given by:

$$\dot{V} = A_x \frac{dx}{dt} + A_h \frac{dh_{ev}}{dt} \quad . \tag{A1-9}$$

The quantity dx/dt is the velocity (u) of the cladding in the axial direction (i.e., the rate at which the rod is elongating relative to the grid). The quantity dh_{ev}/dt is the rate at which the depth of the wear groove is increasing. Letting dx/dt = u, Equation (A1-9) gives the rate of increase in wear depth:

$$\frac{dh_{ev}}{dt} = \frac{\dot{V} - A_x u}{A_h} \quad . \tag{A1-10}$$

For wear spots of a depth equal to or less than $(h_{ev})_{cyl}$, where $(h_{ev})_{cyl}$ is the depth of the wear groove at which the width of the groove becomes equal to the width of the cylindrical section of the dimple, the

projected area of the wear contact surface as viewed in the y-direction will approximate a semi-ellipse. The semi-axes of the ellipse can be approximated by:

$$a = \sqrt{Dh_{ev}} \text{ (in the axial direction)}$$

$$b = \sqrt{2rh_{ev}} \text{ (in the circumferential direction).}$$

The projected area (A_h) is therefore given by:

$$A_h = 1/2\ \pi\ ab$$

$$= \pi \sqrt{rD/2}\ \ h_{ev}\ . \qquad \text{(A1-11)}$$

The projected area (A_x) of the wear contact area in the x-direction is shown in the following sketch:

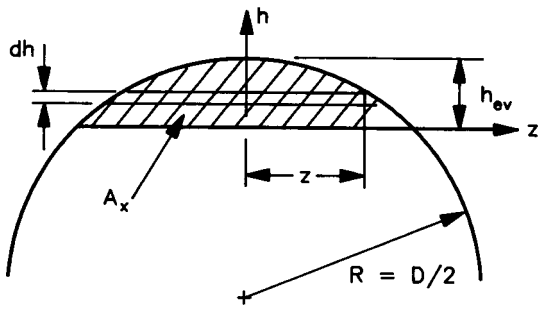

The projected area (A_x) is given by:

$$A_x = 2 \int_0^{h_{ev}} z\ dh\ , \qquad \text{(A1-12)}$$

where:

$$z = \sqrt{Dh - h^2}$$

or

$$z = \sqrt{Dh} \text{ for } h << D.$$

Substituting this expression for z into Equation (A1-12) and integrating over the indicated limits gives:

$$A_x = \frac{4}{3}\sqrt{D}\ h_{ev}^{3/2} . \qquad \text{(A1-13)}$$

Substituting Equations (A1-11) and (A1-13) into Equation (A1-10) gives:

$$\frac{dh_{ev}}{dt} = \frac{\dot{V} - \frac{4}{3}\sqrt{D}\ u\ h_{ev}^{3/2}}{\pi\sqrt{rD/2\ h_{ev}}} . \qquad \text{(A1-14)}$$

Equation (A1-14) is a first-order nonlinear differential equation which can be solved numerically for the depth (h_{ev}) of the wear groove as a function of time. If the wear rate (V) and the rod velocity (u) are fixed, the steady state (i.e., maximum) depth of the wear groove is found by letting the rate dh_{ev}/dt at which the depth increases equal zero, giving:

$$(h_{ev})_{ss} = \left(\frac{9}{32R}\right)^{1/3} \left(\frac{\dot{V}}{u}\right)^{2/3}, \quad (h_{ev})_{ss} << (h_{ev})_{cyl} . \qquad \text{(A1-15)}$$

The time required for the wear groove depth to approach the steady state value as given by Equation (A-15) increases with the distance of the grid from the free end of the rod. This is due to the fact that the rod elongation velocity decreases with the distance from the free end. In the limit, at the

grid level next to the fixed end (where the elongation velocity is essentially zero) the wear depth never approaches a steady state value and increases indefinitely with time as in the case of a stationary wear spot.

For the purpose of the wear design procedure, conservative estimates of the depth of a moving wear spot can be obtained on the basis of the steady state depth or the depth of a stationary wear spot, whichever is smaller. This simplification avoids the need for explicitly solving the differential equation of wear groove formation [Equation (A1-14)] at each time step. The actual depth of a moving wear spot at any given time is always smaller than the depth of a stationary spot. An apparent reversal of this situation during the early stages of the wear groove transient is due to the approximation of the projected area (A_h) of the wear contact surface by a semi-ellipse. This approximation of the projected area, which is made to avoid mathematical complexities in the transient solution, results in an underprediction of the actual projected area which, as can be seen by inspection of Equation (A1-10), leads to an overestimation of the rate of wear depth increase (h_{ev}/dt). It is to be noted, however, that the steady state solution of the moving wear spot depth is independent of the projected area (A_h) so that the steady state depth value is unaffected by the simplifying approximation made with regard to the geometry of this projected area. The steady state depth of a moving wear spot having a width less than the dimple width is actually a function only of the wear rate, the rod elongation velocity, and the rod diameter, and is independent of the grid dimple radius.

A1.3 - OVERLAY WEAR

The procedure described in this section was developed for explicitly calculating the depth increase due to overlay wear. This procedure also permits calculation of the overlay wear developed with differing distributions of vibrational wear between the various grid dimples and with reduced flow velocity.

The general case of the development of overlay wear at a moving wear spot due to a plant shutdown and a reduction in core power is illustrated in Figure

A1-1. The plant is assumed to be shut down for maintenance prior to a reduction in core power at time t_1. The depth (h) is the steady state wear depth developed during operation just prior to the shutdown. During the shutdown period from time t_1 to t_2, an overlay wear depth increment (Δh_s) is superimposed on the wear groove. The plant is started up at a reduced power level at time t_2, with the dimple dwelling in the previously worn section of the wear groove until time t_3 when the rod has elongated sufficiently for the grid dimple to move onto an unworn surface of the cladding. During this dwell period, an additional overlay depth increment (Δh_p) is superimposed on the previously worn section, resulting in a total wear depth of:

$$h_{max} = h_1 + \Delta h_s + \Delta h_p \ .$$

When the grid dimple approaches the previously unworn section of the cladding at the end of the wear groove, a new wear groove of steady state depth (h_2) begins to develop with continuing rod elongation. This new wear groove is assumed to attain its steady state value very shortly after time t_3 (the end of the power-reduction overlay period). Moving wear spot depth solutions for LWBR blanket fuel rods indicate that the steady state depth (h_2) of the new wear groove formed at reduced power is less than the peak depth attained in the previously worn groove at the end of the overlay period. The EFPH interval represented by the overlay period is equal to the operating time interval ($t_3 - t_2$) multiplied by the fractional core power at the reduced power level (P_2).

The overlay wear depth increment (Δh) for moving wear spots in LWBR blanket fuel rods is evaluated by use of Figures A1-2 and A1-3 in which Δh is given as a function of the overlay wear volume (ΔV) for wear spots at grid spring and reaction dimples, respectively. The overlay wear volume is given by:

$$\Delta V = \Delta V_s + \Delta V_p \ , \qquad \text{(A1-16)}$$

where:

ΔV_s = overlay wear volume developed during plant shutdown

ΔV_p = overlay wear volume developed during dwell period following a reduction in core power.

The overlay depth increment (Δh) determined on the basis of the wear volume evaluated by this equation is the total increase in depth due to both a plant shutdown and a reduction in core power (i.e., $\Delta h = \Delta h_s + \Delta h_p$).

The components of overlay wear volume are given by

$$\Delta V_s = f_s \dot{V}_o \Delta t_s \text{ and} \qquad \text{(A1-17)}$$

$$\Delta V_p = f_p \dot{V}_o \Delta t_p \ , \qquad \text{(A1-18)}$$

where:

f_s, f_p = wear rate factors applying to the shutdown period and to operation at reduced power, respectively

$\dot{V}_o$ = wear rate (mil^3/hr) with four pumps operating at fast speed

Δt_s, Δt_p = pump operating time during shutdown and dwell time during operation at reduced power, respectively (hours).

The factors f_s and f_p, which correct the wear rate for operation at a reduced flow velocity, are evaluated by:

$$f_i = \left(\frac{U_i}{U_o}\right)^n \ , \qquad \text{(A1-19)}$$

where:

U_i = rodded-region flow velocity during shutdown period or during operation at reduced power

U_o = rodded-region flow velocity with four pumps at fast speed

n = wear rate flow exponent (n = 1.7 was used for LWBR evaluations from Reference 60).

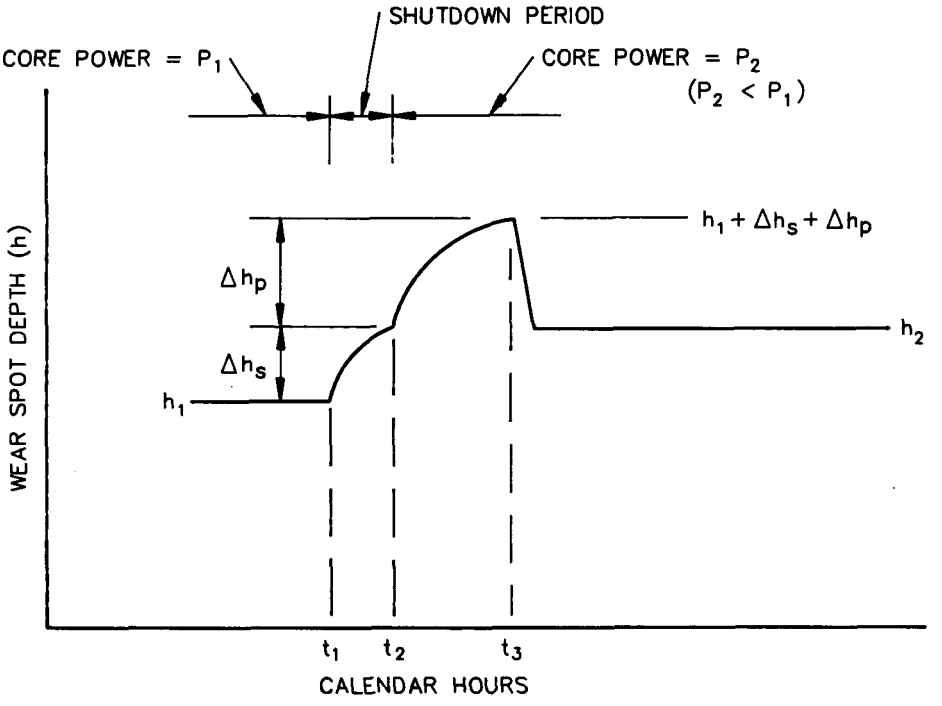

LEGEND:

h_1 = steady state depth at power level P_1

Δh_s = overlay depth due to pump operation during plant shutdown

Δh_p = overlay depth due to core power reduction

h_2 = steady state depth at reduced power level P_2

t_1 = time of plant shutdown

t_2 = time of plant startup

t_3 = time at which grid dimple completes retracing over previously worn section of wear spot.

Figure A1-1. Development of Overlay Wear Due to Plant Shutdown and Power Reduction (LWBR Blanket Fuel Rods)

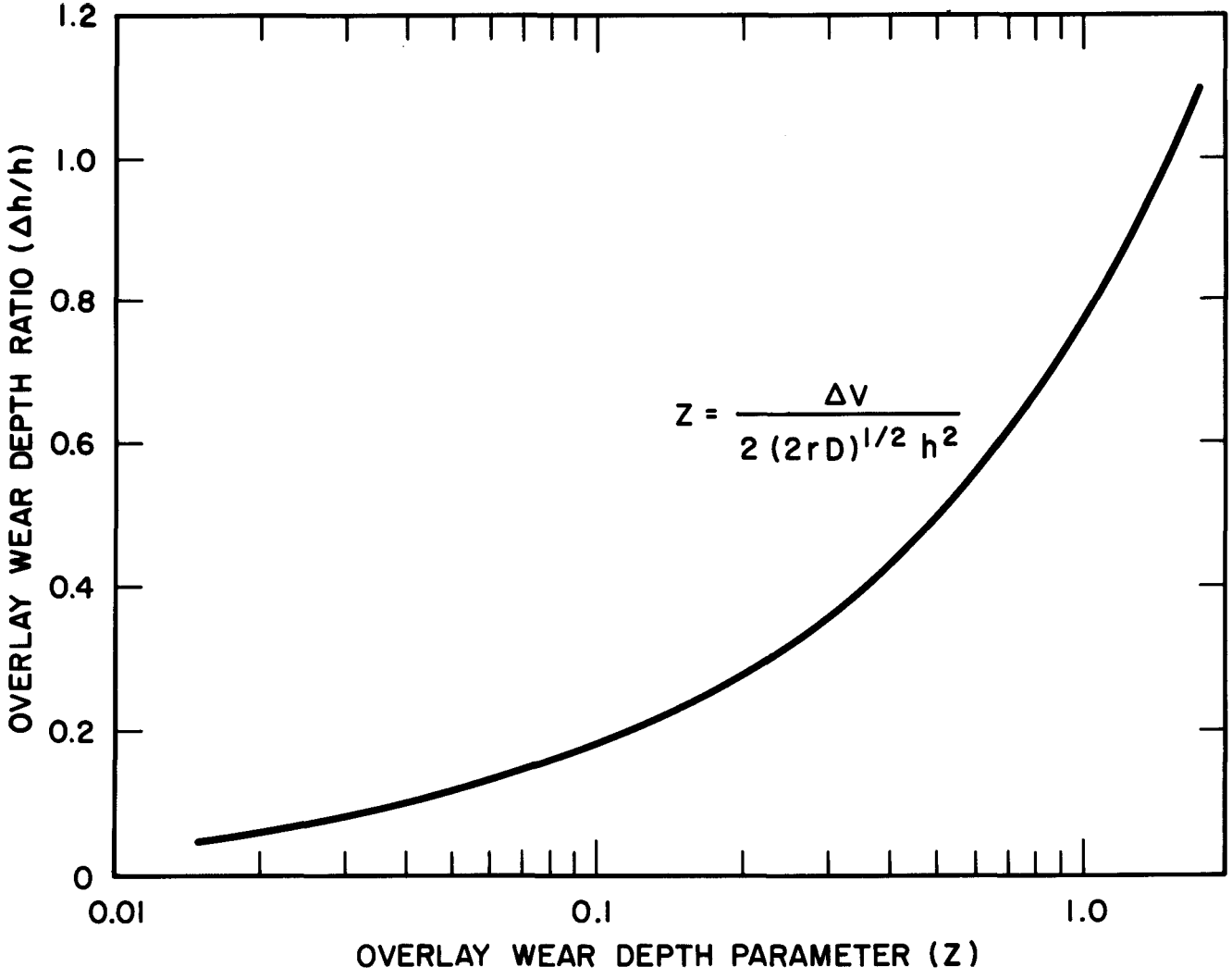

Figure A1-2. Overlay Wear at a Grid Spring

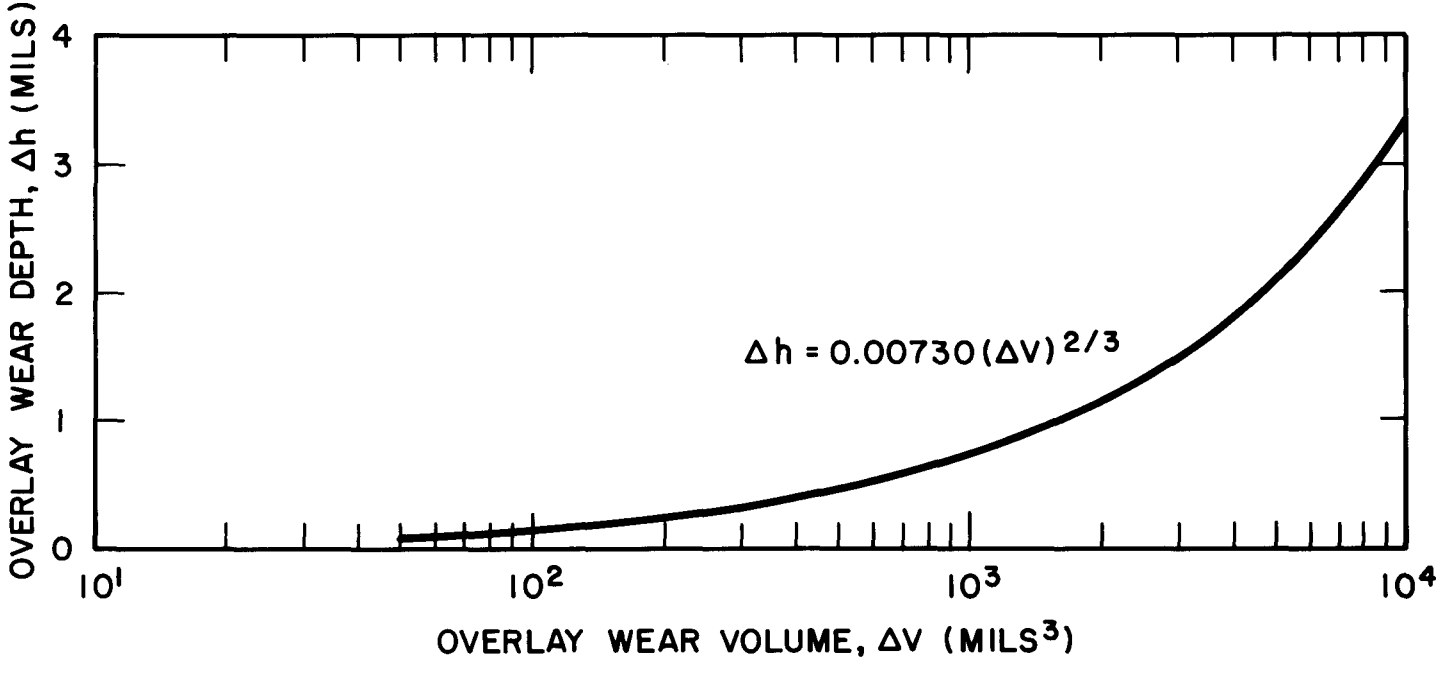

Figure A1-3. Overlay Wear at a Grid Dimple

The dwell time (Δt_p) during operation at reduced power is given by:

$$\Delta t_p = \frac{l_g \, s_o}{l_o \, u_g} \Delta p \text{ hours} , \qquad \text{(A1-20)}$$

where:

l_g = distance from end of fuel stack nearest the fixed end of the rod to the grid level in question

l_o = total length of fuel stack

s_o = total change in length of fuel rod resulting from a 100 percent change in core power

u_g = rod elongation velocity at grid level in question (mil/hr)

Δp = fractional reduction in core power.

The maximum wear depth developed at a moving wear spot in a blanket fuel rod following a shutdown period and a reduction in core power is then given by:

$$(h_{ev})_{max} = (h_{ev})_{ss} + \Delta h , \qquad \text{(A1-21)}$$

where:

$(h_{ev})_{ss}$ = steady state wear depth developed prior to a shutdown and a reduction in core power.

In the case of a grid spring wear site, the depth ratio ($\Delta h/h$) is plotted for an LWBR power-flattening blanket rod in Figure A1-2 as a function of an overlay wear parameter defined as:

$$Z = \frac{\Delta V}{2 \, (2 \, r \, D)^{1/2} \, h^2} , \qquad \text{(A1-22)}$$

where:

D = rod diameter (mils)

r = spring dimple radius (mils)

h = $(h_{ev})_{ss}$, as defined in Equation (A1-21).

Calculation of the overlay wear depth increment for a moving wear spot is based on the superposition of a stationary wear spot on the previously worn groove. For LWBR rods, this approach is considered to be realistic, as well as conservative, in view of the relatively small motions executed by a rod relative to the grid during the overlay dwell period (~10 mils maximum for a 10 percent reduction in core power).

The solution for overlay wear in a moving wear spot at a grid spring is based on an infinite dimple width and, therefore, is applicable to wear spots having a maximum depth of up to approximately 19 mils on LWBR blanket rods. The overlay solution at a reaction dimple is based on a finite dimple width equal to the total width of a blanket grid reaction dimple (85 mils) and is, strictly speaking, applicable to the evaluation of overlay wear superimposed on steady state depths equal to or greater than 8.4 mils (the depth at which the width of a wear spot in a power flattening blanket fuel rod becomes equal to the total width of a reaction dimple). At smaller wear depths, the overlay solution given in Figure A1-3 tends to underestimate the overlay increment. However, at wear depth levels generally of interest in fuel rod design assessments, the error introduced by the use of this overlay solution is relatively small. For example, the overlay depth at a reaction dimple is underpredicted by approximately 3 percent when superimposed on a steady state wear depth of 7 mils, and by approximately 6 percent when superimposed on a depth of 6 mils. Errors of this magnitude in the calculated overlay wear increment result in the cladding stresses being underpredicted by no more than about 0.5 percent. In view of the conservatism in the overlay analysis, as well as the additional complication which would be involved in calculating overlay wear at a finite reaction dimple as a function of wear depth, the overlay wear depths determined by Figure A1-3 can be applied with sufficient accuracy to steady state wear depths less than 8.4 mils in LWBR blanket rods.

An overlay wear allowance for reduction in core power is not applicable in the case of a stationary wear spot. However, allowance must be made for overlay wear developed at a stationary spot during a plant shutdown. This is

done by including a volume term (ΔV_s), as calculated by Equation (A1-17), in the total wear spot for each shutdown occurring up to the time of life in question.

A1.4 - FINITE DIMPLE WIDTH EFFECT

The effect of a "finite" dimple width on wear spot geometry is illustrated in Figure A1-4, showing wear spot cross sections at various wear depths. Because of the rolled (beveled) edges, the width of the cylindrical surface of reaction dimples is seen to be less than the total dimple width [Section (1)A of Figure A1-4]. The value of h_1 is the depth at which the spot width at a reaction dimple wear site becomes equal to the total width of the dimple as shown in Section (1)A of Figure A1-4. In the case of the springs, the edges are square, and the cylindrical surface therefore extends over the entire width of the spring. The corresponding depth (h_1) at a spring wear site is shown in Section (1)B of Figure A1-4. It can be seen that the departure from a cylindrical dimple geometry to a "finite-width" geometry results in a smaller wear spot cross-sectional area for a given wear depth, demonstrating that the finite dimple width effect tends to increase wear depth developed for a given volume of wear product.

The wear depth developed at spring and reaction dimple wear sites is a function of the calculated wear spot volume (V). The wear volume is calculated from Equation (A1-6) as:

$$V = \sum \dot{V}_j \, \Delta t_j, \qquad \text{(A1-6)}$$

where:

$\dot{V}_j$ = the vibrational wear rate (mil^3/hr) at a given contact wear site existing over the time interval Δt_j (hours).

The stationary wear spot depth solutions are obtained by evaluating the volume integral:

$$V = \int A_x \, dx \ , \qquad \text{(A1-23)}$$

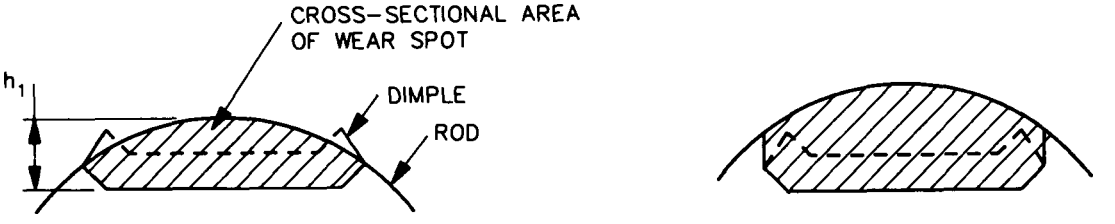

(1) Spot Width Equals Total Dimple Width (2) Spot Width Greater Than h_1

A. REACTION DIMPLE WEAR SITE

(1) Spot Width Equals Spring Width (2) Spot Depth Greater Than h_1

B. SPRING WEAR SITE

Figure A1-4. Effect of Finite Dimple Width
(Using LWBR Spring and Dimple Geometries)

where:

A_x = cross-sectional area of wear spot at an axial distance (x) along the rod. (These areas are similar in shape to those shown in Figure A1-4.)

For a given type rod and dimple contact, the volume integral [Equation (A1-23)] is solved by numerical integration for a series of wear depths and plotted against wear depth. Numerical integration (by Simpson's rule) was found to be more appropriate than a closed-form solution because of the mathematical complexities introduced by the irregular volumes formed when the wear depth exceeded the limiting value (h_1).

The moving wear spot depth is obtained from the steady state solution of the differential equation of wear depth in an elongating rod [Equation (A1-10)]. The steady state solution is:

$$A_x = \frac{\mathbb{V}}{u} , \qquad \text{(A1-24)}$$

where, in this case, A_x is the projected area of the wear spot in the axial direction at a section through the center of the spring or dimple (as shown in Figure A1-4). Using the geometrical relation which exists between the cross-sectional spot area and wear depth, values of A_x $(= \mathbb{V}/u)$ can be calculated and plotted for a series of wear depths.

For cases in which the wear depth is less than the limiting value (h_1) given in Figure A1-4, the plotted wear depth solutions are identical to those provided by a solution based on a crossed-cylinder contact geometry (i.e., with no finite dimple width effect). Hence, the curves can be used to determine vibrational wear depth (not including overlay wear) for depths less than limiting depth value h_1 (down to the limit of the plots at about 1 mil), as well as those greater than h_1.

In Sections A1.1 and A1.2, the limiting depth value (h_1) at which departure from crossed-cylinder contact geometry occurs was referred to as $(h_{sv})_{cyl}$ and $(h_{ev})_{cyl}$ for the stationary and moving wear spot models, respectively.

APPENDIX A2 - CLADDING STRAINS DUE TO RIDGING

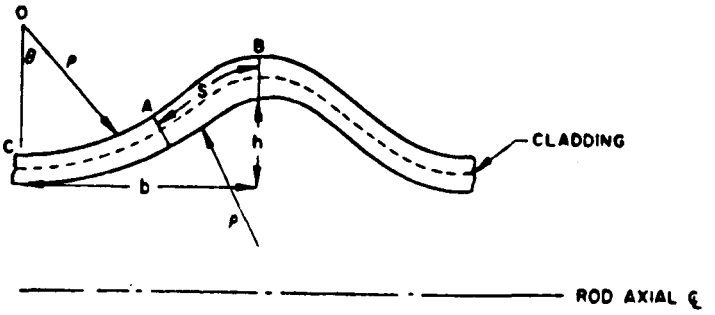

$$\varepsilon_\theta^* = \varepsilon_\theta^o + \delta\varepsilon_\theta \tag{A2-1}$$

$$\varepsilon_z^* = \varepsilon_z^o + \delta\varepsilon_z \tag{A2-2}$$

$$\varepsilon_r^* = \varepsilon_r^o + \delta\varepsilon_r \tag{A2-3}$$

where:

ε_θ^*, ε_z^*, and ε_r^* = total inelastic strain at the ridge

ε_θ^o, ε_z^o, and ε_r^o = inelastic strain at midplane of pellet.

Since inelastic strain does not contribute to volume change,

$$\varepsilon_\theta^* + \varepsilon_z^* + \varepsilon_r^* = 0, \text{ and } \varepsilon_\theta^o + \varepsilon_z^o + \varepsilon_r^o = 0 \tag{A2-4}$$

$$\delta\varepsilon_\theta = h_D/D_o \tag{A2-5}$$

where:

h_D = diametral ridge height

D_o = cladding outside diameter at the pellet midpoint, measured at the same time that h_D is measured.

$$\delta\varepsilon_z = \delta\varepsilon_z' + \delta\varepsilon_z'' , \qquad \text{(A2-6)}$$

where:

$\delta\varepsilon_z'$ = axial strain due to axial stretching at midthickness

$\delta\varepsilon_z''$ = bending strain on outer fibers.

$$\delta\varepsilon_z' = \frac{2S - b}{b} , \qquad \text{(A2-7)}$$

where:

S = half the length of circular arc from bottom to top of ridge

b = half the base width of the ridge,

and

$$\delta_z'' = \frac{t}{2\rho} \qquad \text{(A2-8)}$$

where:

ρ = radius of curvature defining the ridge shape

t = cladding thickness.

$$\rho = \frac{b^2}{4h} + \frac{h}{4} \qquad \text{(A2-9)}$$

for $b >> h$,

$$\rho \cong \frac{b^2}{4h} \qquad \text{(A2-10)}$$

therefore,

$$\delta\varepsilon_z'' \cong \frac{2th}{b^2} \quad . \tag{A2-11}$$

The calculation of $\delta\varepsilon_z'$ proceeds as follows. A minimum value of 2 S can be calculated by:

$$2\ S_{min} = \left(b^2 + h^2\right)^{1/2} \quad . \tag{A2-12}$$

Thus, substituting the value of 2 S_{min} from Equation (A2-12) into Equation (A2-7) yields:

$$\delta\varepsilon_z' = \frac{\left(b^2 + h^2\right)^{1/2} - b}{b} \tag{A2-13}$$

and, therefore,

$$\delta\varepsilon_z = \frac{2th}{b^2} + \frac{\left(b^2 + h^2\right)^{1/2} - b}{b} \quad . \tag{A2-14}$$

*U.S. GOVERNMENT PRINTING OFFICE: 1988-505-001/80169